T-3809

EFFECTS OF COATING PROPERTIES ON THE FORMABILITY OF COATED SHEET STEELS

by

RANGARAJAN VENKATARAMAN

T-3809

A thesis submitted to the faculty and the Board of Trustees of the Colorado School of Mines in partial fulfillment of the requirements for the degree of Doctor of Philosophy (Metallurgical Engineering).

Golden, Colorado
Date: 11/22/89

Signed: _____
Rangarajan Venkataraman

Approved: _____
David K. Matlock
Thesis Advisor

Golden, Colorado
Date: 11/22/89

_____
John J. Moore
Department Chairman
Metallurgical and Materials Engineering

ABSTRACT

This work examines flow and fracture in coatings and friction behavior of coated sheet steels as a function of coating crystallographic texture, microstructure and surface morphology of coatings. Electrogalvanized zinc and hot dipped zinc and zinc-alloy coatings were characterized by X-ray diffraction and scanning electron microscopy. Samples of each were tested in simple tension and with the bending under tension type friction test. Preferred orientation of zinc basal planes parallel to the coating surface promoted cracking in stretching operations, while plastic deformation was the dominant mode of strain accommodation in coatings without such basal plane texturing. In zinc-alloy coatings intermetallic phases contributed to cracking as the primary mode of strain accommodation. These observations were linked by the development of conceptual models of coating deformation as a function of coating crystallographic texture, microstructure, material strength, and imposed strain state.

A model for metallic friction proposed by Wanheim and Bay, which is based on deformation of surface asperities,

has been tested and proven applicable for coated sheet steels. The shear resistance due to friction was shown to depend on the true contact area at a given pressure and the adhesive strength of the asperity bonds. For pure zinc the strength of the asperity bonds is lower for coatings which possess basal planes parallel to the coating surface. For the higher strength alloy coatings, low normalized friction stresses resulted primarily from the lower true contact areas at a given pressure.

The results on coating deformation suggest that for pure zinc coatings a non-basal plane texture parallel to the surface is favorable for plastic flow and good substrate coverage. Frictional analyses on the other hand show that a basal plane texture parallel to the surface in pure zinc coatings is favorable for lower friction coefficients. Therefore, coating design will require a compromise between superior flow in the coatings and lower surface friction coefficients. A suggested design would consist of a dual layer pure zinc coating with basal plane texture in the surface layers and non-basal plane texture in the bulk of the coating.

TABLE OF CONTENTS

LIST OF FIGURES

LIST OF TABLES

ACKNOWLEDGEMENT

The author would like to express his sincere appreciation to his thesis committee: Professors David K. Matlock (thesis advisor), George Krauss, Chester Van Tyne, John T. Williams (chairman) and Norubu Wada.

The author is especially indebted to his advisor Professor Matlock for his continued support and guidance in this work. The author would like to thank Professor Van Tyne for his help with the theoretical study on friction. The author would like to thank Professor Krauss for his support and guidance throughout the program. The author acknowledges the help of Dr. Lawrence Franks at Inland Steel Research Laboratories, East Chicago, Indiana, in obtaining pole figure measurements.

The author owes a debt of gratitude to his wife Latha for her invaluable help in putting together this manuscript.

The author acknowledges and appreciates the financial support of the Advanced Steel Processing and Products Research Center at the Colorado School of Mines.

1.0 INTRODUCTION

Zinc based coatings are widely used for corrosion protection of steel sheet and strip products, and are currently under intensive development for enhanced corrosion resistance in automotive applications (1-3).

The zinc coating on steel affords two types of protection against corrosion. Steel articles coated with zinc remain rust free for a longer period of time because zinc, along with its passive layers of oxides or hydroxides, physically prevents the steel from coming in contact with aggressive media. This protection is termed the "barrier effect". Zinc inherently corrodes at a much slower rate compared to iron. Even though the half-cell potential of Zn is more anodic compared to Fe, the exchange current density for hydrogen evolution reaction is lower on zinc surfaces, resulting in slower corrosion rates for zinc. A second type of corrosion protection, is the sacrificial anodic protection zinc provides to steel. When both steel and zinc are exposed to an adverse environment, zinc corrodes preferentially since it is anodic to steel in many environments. According to the mixed potential theory (4), coupling zinc to iron will result in a greater anodic

dissolution of zinc and a reduced dissolution rate for steel.

Simultaneous requirements of barrier and galvanic protection coupled with the low toxicity limits in industry are met only by zinc. Aluminum for example provides a better barrier effect but offers very little galvanic protection. Magnesium offers excellent galvanic protection, but has no barrier effect. Cadmium offers superior barrier effect and good galvanic protection, but produces highly toxic compounds. Thus zinc is the choice of the automotive and structural industries for corrosion protection of steel. Research in the past few years has shown that compared to pure zinc, Zn-alloy coatings perform better in atmospheric corrosion tests (5-9). Therefore considerable work has been done in developing new zinc-alloy coatings. The prominent hot-dip zinc-alloy coatings include the galvannealed coating which is made up of Zn-Fe alloys and Galfan[R1] and Galvalume[R2] coatings which are Zn-Al alloy coatings of different compositions. As in the case of hot-dip coatings, there are electroplated Zn-alloy coatings. The metals co-deposited with zinc include iron, nickel, chromium, cobalt and molybdenum, either singly or in combination.

Table 1 gives a summary of the zinc coatings and the major industry sectors where they are used (1). Table 1 shows that a variety of zinc-based coatings are used in automotive, appliance and building industries. Automotive industry is the largest consumer of zinc coated sheet steels. Coatings listed in Table 1 differ significantly in their compositions. As a result, the binary phases formed in these coatings vary. Table 2 gives the crystallographic structure of phases formed in some of the commercially used Zn-alloy coatings. The crystallographic structures vary from HCP to complex cubic. The coatings are made up of either a single phase or two phases with differing crystal

---

[1]Galfan[R] is a registered trade name of the International Lead Zinc Research Organization for steel sheet coated with 5% Al-Zn alloy with small amounts of lanthanum and cerium mischmetal.

[2]Galvalume[R] sheet is a registered trademark of the Bethlehem Steel Corporation for steel sheet coated with 55% Al-Zn alloy.

Table 1 A listing of commercially used zinc-based coatings

Type	Coating	Major Industry Sectors
Zinc coatings on steel — Hot Dip Coatings	Zinc	Building/Appliance/Automotive
	Zn-5% Al	Building
	Zn-55% Al	Building/Appliance
	Galvanneal Zn-Fe	Automotive/Appliance
Zinc coatings on steel — Zn-rich paint systems	Zincrometal Type	Automotive
	Special development	Automotive
Zinc coatings on steel — Electro-deposition	Zinc	Automotive
	Co-deposited zinc alloy	Automotive
	Duplex layers	Automotive

Table 2 Microstructural and crystallographic characteristics of zinc and zinc-alloy coatings

Coating Type	Coating Composition	Micro-structure	Phases	Crystallographic structure
Electro-galvanized	100% Zn	-	η	HCP, Zn
Hot Dip galvanized	100% Zn	Possible intermet-metallics	η	HCP, Zn
EC* Zn-Fe	15% Fe	Two Phase	$\eta + \delta$	HCP, Zn + HCP, $FeZn_{10}$
Galvann-ealed	15% Fe	Two Phase	$\delta + \Gamma$	HCP, $FeZn_{10}$ + FCC, Fe_5Zn_{21}
EC Zn-Ni	11-13% Ni	Single Phase	Γ	Complex cubic Ni_5Zn_{21}
EC Zn-Ni	7-9% Ni	Two Phase	$\Gamma + \eta$	Complex cubic Ni_5Zn_{21} + HCP, Zn
Galfan (Zn-Al)	5% Al + 0.2% (La+Ce)	Eutectic	η, matrix + Al- rich particles.	HCP, Zn
Galvalume (Zn-Al)	55% Al + 1.6% Si	Al dendr. + Zn-rich interdendritic regions**	α Al + η Zn	FCC, Al + HCP, Zn

* EC - ElectroCoated

** Zn rich interdendritic regions have a high density of precipitates and pure Si particles

structures. Some coatings, such as Galfan, have an eutectic microstructure. Since flow behavior of a material is a function of its crystal structure, coatings listed in Tables 1 and 2 will exhibit significant variations in flow and fracture behavior.

While most of the development work in zinc coated sheet steels has concentrated on improving the corrosion resistance there are some significant problems that need to be solved in the area of forming coated sheet steels. The two significant problems are those of coating effects in friction and coating damage during forming. Besides these, the coating can also influence the mechanical behavior of the steel substrate. Hot dip coatings have been shown to adversely affect the formability and ductility of steels (10,11). The coating itself can flake, powder or gall independent of the substrate. Flaking consists of separation of relatively large portions of the coating from the substrate steel. Powdering is fine coating debris resulting from abrasion between the asperities on the tool surface and the material. Galling develops when flakes and powder particles build up on the die surfaces. These forming problems are described in detail in the literature section on formability of coated sheet steels.

Formability problems are a function of the flow and fracture behavior of the coating material. Therefore, characterization of the coating in terms of its microstructure and texture would be the first step in understanding the forming characteristics of the coated sheet steels. Furthermore, the deformation behavior of the coatings can be studied by following texture and morphological changes in the coating as a function of strain in uniaxial or biaxial tension. Such studies of microstructure, texture and stress state effects on flow and fracture of zinc coated sheet steel would complement corrosion research in developing coatings with good formability characteristics and excellent atmospheric corrosion resistance.

2.0 LITERATURE STUDY

2.1 Galvanizing Process and Coating Characteristics

The process of coating steel with zinc is called galvanization. There are two primary methods by which sheet steels are galvanized. One is a hot dip galvanizing process where the steel after proper surface pretreatments is dipped into a molten zinc bath. The time of dipping and the temperature of the bath are carefully controlled. The second method is electrodeposition of zinc on steel. The electrodeposited zinc has a much smoother finish and better formability compared to hot dip zinc coatings (10).

2.2 Hot Dip Galvanizing

2.2.1 Continuous Galvanizing

In a hot dip galvanizing process, continuously galvanized sheets are produced by passing the steel substrate through a bath of molten zinc at a temperature of about 450^{o}C. Suitable fluxes are either carried on the surface of the bath or applied to the steel surface, in

order to obtain continuous, adherent zinc coatings. For operations where a heat treating step is involved ahead of the galvanizing pot (either for annealing the steel or cleaning the steel surface), the heated steel is kept under a reducing atmosphere until it passes below the surface of the molten zinc bath (12).

The quality of hot dip coatings depends on proper surface pretreatment of the steel substrates, steel thickness, dipping conditions (time and temperature of bath), additives to the zinc bath and post-dipping processing factors such as the cooling rate etc. (13). Surface pretreatment of the steel includes degreasing, pickling in an acid solution, rinsing and fluxing. Fluxing facilitates the reaction between steel and molten zinc (13).

During hot dip galvanizing Fe-Zn alloy layers are formed in the coating. The types of alloy formed and the extent of alloy formation depends on the zinc bath temperature and immersion times involved in the galvanizing process since the reaction between Fe and Zn is primarily diffusion controlled. The Zn rich end of Fe-Zn binary phase diagram is given in Figure 1, where several of the

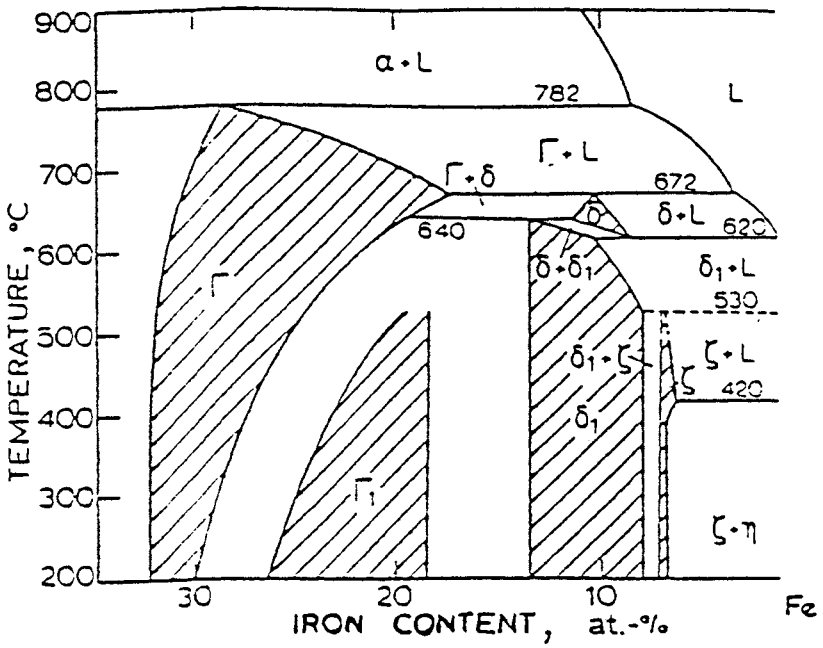

Figure 1. Zinc-rich end of Fe-Zn binary phase diagram (14)

intermetallic phases that can form in a Zn-Fe alloy coating are shown. The crystallographic structures of most of these phases are listed in Table 2. Phase ζ is $FeZn_{13}$, with a monoclinic structure.

The metallurgy of hot dipped galvanized coatings has been extensively reviewed by Short and Mackiowak (14). They considered the kinetics and thermodynamics of the reaction between Fe and Zn at different temperatures (14,15), along with the effects of surface preparation, stresses, shape of the article and alloying additions. Also in their work, the different alloys formed in the coating were characterized and some of their physical properties determined. In hot dip galvanized steel, the Fe-Zn alloy layer provides the bond between the zinc outer layer and the steel base. It is important to have the alloy layer completely cover the steel base. However excessive alloy formation will cause poor coating properties (12).

The addition of 0.15 wt.% Al to hot dip continuous galvanizing baths is mainly for the purpose of minimizing the Zn-Fe alloy layer thickness. This improves coating adherence and prevents flaking during forming operations.

The Al reacts with steel to form a thin layer of Fe-Al compounds (primarily a thin layer of Fe_2Al_5) which inhibits further reaction between the steel substrate and the zinc bath (16), provided the immersion times are not too long. With longer immersion times, Zn reacts with the Fe_2Al_5 layer and isolated particles of a Fe-Al-Zn ternary phase appear in this layer (16). With time the protective Fe_2Al_5 film is consumed and the Zn reacts with steel forming Fe-Zn intermetallic phases in the coating. This mechanism is more pronounced in Zn baths containing Fe additions (16).

Spangles are a prominent feature in hot dip galvanized coatings. A spangle on galvanized iron consists of alternating sectors of shiny and frosty regions (17,18). These sectors are roughly triangular in shape. Each shiny-frosty pair originates from a single nucleus and is a single grain. A spangle consists of many such grains growing from several nuclei which are related to each other in orientation. The frosty region represents a subgrain of the initial shiny single crystal, where the basal planes are aligned approximately parallel to the steel surface. The frosty regions and the typical spangle structure originate as a result of alloying additions, for example

lead and tin, in the zinc bath. With increasing amounts of alloy additions, the entire spangle may be frosty (17). Each shiny-frosty pair is separated by a straight line boundary which is a direction of maximum growth rate in epitaxial growth of the zinc crystal (<10$\bar{1}$0> directions on basal plane). Spangle nuclei form on the sheet steel surface and the spangle structure is essentially dendritic, with the primary dendrites oriented along all six favorable directions on the basal plane, giving a hexagonal shape to the growing spangle (18). Spangles have their main growth direction in the plane of the surface and those that grow prominently, especially under fast cooling rates, are those with basal planes parallel to the steel base (18).

The size of the spangle influences the fracture behavior of the coatings. A small spangle size is preferred in many applications. Lead, tin and cadmium additions are made to the zinc bath to control the spangle size (10). A low Pb content in the bath promotes minimum spangle or spangle free appearance. Antimony additions increase the spangle density and improve the quality, lustre and uniformity of the coating (13).

The presence of water vapor in the atmosphere during

solidification has been reported to produce coatings of uniform thickness (19). When small amounts of Al are added to a zinc bath to inhibit alloy growth, an Al_2O_3 film forms on the surface of the coating in the presence of some moisture. This oxide film physically restricts the spangle growth to two dimensions, thus reducing the roughness in the coatings (19).

2.2.2 Batch Hot Dip Galvanizing

Hot dip galvanizing after fabrication, where steel articles are dipped in molten zinc is called Batch Galvanizing. Here the coating consists of several intermetallic layers and an outer zinc layer, with a gradient in zinc composition from the free surface to the steel coating interface (20). Recent work in the area of batch galvanizing is concentrated on solving the problem of galvanizing structural steels containing Si, which are very reactive and form thick, brittle and often non-adherent coatings. Some of the attempted solutions are use of zinc-nickel bath, a bath with lead, aluminum, magnesium and tin additions, and high temperature galvanizing (a bath temperature of 550^{o}C) (20).

2.3 Electrogalvanizing

In the electrogalvanizing (EG) process steel strips pass through electrolytic cells in which current flows from the anode to the cathode (strip) through a zinc solution, bonding the zinc to the steel. The anodes can either be soluble zinc anodes or insoluble anodes of lead or lead alloys or platinized titanium, in which case the solutions have to be replenished in zinc (10). The electrogalvanizing process is conducted at room temperature and therefore the steel substrate properties are not affected, unlike the hot dip process. For example, in hot dip process excess carbon can remain in solution due to the associated heating and rapid cooling of the steel strips, resulting in steels with reduced formability (10). This has to be rectified with a post annealing heat treatment.

Electrolytic deposition of zinc coatings does not produce intermetallic layers in the coating, since the process is conducted at room temperature where no significant diffusion reaction takes place. A bond is formed between the Fe and Zn by sharing of electrons at the interface (10).

Electrolytic plating conditions such as pH of the electrolytes, addition of specific impurities to the plating bath, different types of electrodes, varying current densities etc., can result in significant variations in coating morphology and texture, as will be discussed later along with results from the present study. The influence of steel substrate texture in the hetero-epitaxial growth of zinc crystals will also be discussed in the section on results (Section 5.1.1).

2.4 Alloy Coatings and their Recent Developments

Some of the recent developments in continuous hot dipped galvanized coatings are the zinc alloy coatings, which include galvannealed coatings and the zinc-aluminium alloy coatings such as Galfan and Galvalume (20). These developments are a result of findings that show an enhanced atmospheric corrosion resistance in alloyed zinc coatings compared to pure zinc coatings (4-9). However, the galvanic protection is reduced upon alloying.

Galvannealed coatings are made entirely of Zn-Fe intermetallic alloys. They have a composition of 90% Zn and 10% Fe, by weight. They are produced by a post heat

treatment after hot dip processing to promote alloy growth, or by wiping the free zinc off from the surface of a hot dipped panel when it exits the coating pot. Galvannealed coating has good paint adherence and coated sheet steels with galvannealed coating have better weldability than those with pure zinc coating (10).

There are a variety of zinc-aluminium alloy coatings with the Al content varying from 1 to 55 wt.% and with a third alloying element. Some examples are, Crack free (1-2% Al), Super-zinc (5% Al-Mg), Galfan (5% Al - mischmetal), Lavagal (35% Al-Na-Mg) and Galvalume (55% Al - 1.5% Si) (20). Among these, Galvalume and Galfan are produced commercially in North America, as well as other places.

Galvalume is a hot dipped coating used for steel to improve atmospheric corrosion performance. The commercial coating consists of 55% Al, 43.4% Zn and 1.6% Si (21). Si prevents a strong and rapid exothermic reaction between the Al-Zn bath and the steel. A diffusion layer is formed between the steel and the bath, called the 'alloy layer', which consists of Fe-Al and Fe-Al-Si compounds (21). The overlay, above the alloy layer consists of α-Al dendrites,

Zn rich interdendritic regions and pure Si particles which form as a result of supersaturation of the Al-Zn bath upon cooling. The Al dendrites contain approximately 18% Zn and 0-1.8% Si in solid solution (21). The composition of the α-Al dendrites compares well with the composition expected from the Al-Zn binary phase diagram. The maximum solubility of Si in Al is approximately 1.6%. The zinc rich interdendritic regions have a high density of precipitates, besides Si particles (21). Zinc-rich regions in the overlay provide galvanic protection to any exposed areas of steel, while the aluminum-rich regions provide extended corrosion resistance (20).

Galfan is a Zn-5% Al-mischmetal alloy coating for steel. Galfan has good formability combined with a corrosion resistance exceeding that of hot dip or electrogalvanized coatings (9), and is compatible with the paint systems used in the automotive industry. Galfan also exhibits good resistance to flaking and microcracking during forming operations (9). The microstructure of Galfan consists of a eutectic structure of alternating lamellae of zinc-rich and aluminum-rich phases. The fineness of the structure increases with the cooling rate. The microstructure is completely eutectic at very high

cooling rates. If the cooling rate is slow, primary zinc or aluminum-rich phases are also formed (9). The 0.05% misch metal (La + Ce) causes complete wetting of the steel surface by the Al-Zn alloy thereby suppressing any intermetallic phase formation. The absence of any intermetallic phases in the coating is one reason for the good formability of Galfan-coated steel (20). The fine eutectic structure also helps by providing resistance to crack propagation.

As in the case of hot dip coatings, there are several electrodeposited Zn-alloy coatings being developed for improved corrosion performance. The metals co-deposited with zinc include iron, nickel, chromium, cobalt and molybdenum, either singly or in combination. The coatings may either have low alloy content or substantial alloy content. The coatings may also have multiple layers (duplex coatings). The corrosion inhibition of Co and Ni cations in the zinc oxide film on galvanized steel have been studied by Leidheiser and Suzuki (22). They proposed that Co ions on zinc surfaces act as electron traps to inhibit the cathodic reaction and reduce zinc corrosion.

Some of the recent developments in the area of

electroplated coatings and the companies involved in these developments are summarized in reference 2. Zn-Ni single phase (Γ) coatings with 11-15 at.% Ni (refer to Table 2) provide the best barrier protection for unpainted applications, while pure zinc provides the best galvanic protection. Dual phase ($\Gamma+\eta$) 9 at.% Ni coatings provide the best compromise between galvanic and barrier protection and a minimum paint delamination. Zn-Mn electroplated coatings are being developed by Nippon Kokan K.K in Japan. Coatings with 30 at.% Mn, have been shown to have a much better corrosion resistance than electrogalvanized coatings in salt-spray tests and cyclic tests (2).

Multizincrox is a multilayer electrogalvanized steel sheet, with an electroplated zinc layer and an outer electroplated layer of cubic shaped particles of metallic chromium in a hydrated chromium oxide matrix (23). Multizincrox is claimed to have a superior perforation and cosmetic corrosion performance compared to that of electrogalvanized coatings (21).

2.5 Effect of Strain in the Coatings on Corrosion Performance

While analyzing corrosion data of galvanized steels it must be noted that due to the lack of a standardized test, companies adopt different corrosion evaluation tests. A given material may perform better under one set of testing conditions, while showing significant corrosion in another. As a result there is a wide variation in the reported corrosion performance of zinc-coated sheet steels. Also, effects of coating deformation on corrosion performance are not clear at present. Some studies show that corrosion is not affected by cracks in the zinc as long as the galvanized panel is sufficiently phospated and painted (24,25). In many practical applications the paint is chipped in localized regions. Therefore corrosion studies of deformed, coated steel sheets in gravel impingement or scribe tests where the paint system is locally removed is of greater practical significance. This section cites some of the work in literature where a clear correlation between the deformation of the coating and the subsequent corrosion performance is shown.

Gronostajski and Ghattas (26) studied the influence of forming on the cracking behavior of coatings and the subsequent corrosion resistance of strained coated sheet steels. Hot-dip galvanized coatings were additionally coated with Polyvinylchloride or Polyethylene prior to deformation. They found zinc coatings to be more prone to cracking in biaxial stretching. The corrosion resistance was primarily affected by cracking in the zinc layer. The corrosion was more significant in biaxially stretched regions which started cracking at lower strains, compared to drawn or uniaxially strained regions which showed a greater resistance to cracking. Strain also resulted in thinning of the zinc layer which decreased the corrosion resistance further. Their results are summarized in Figure 2 which shows the extent of corrosion mapped onto a forming limit diagram.

Aoki et. al. (27) also found that corrosion behavior of a plastically deformed galvanized steel depends on both the mode of deformation and the amount of plastic strain. Strain in stretching operations (refer to Fig. 2) was effective in reducing corrosion resistance of galvanized panels while drawing operations had little influence in salt spray tests (27).

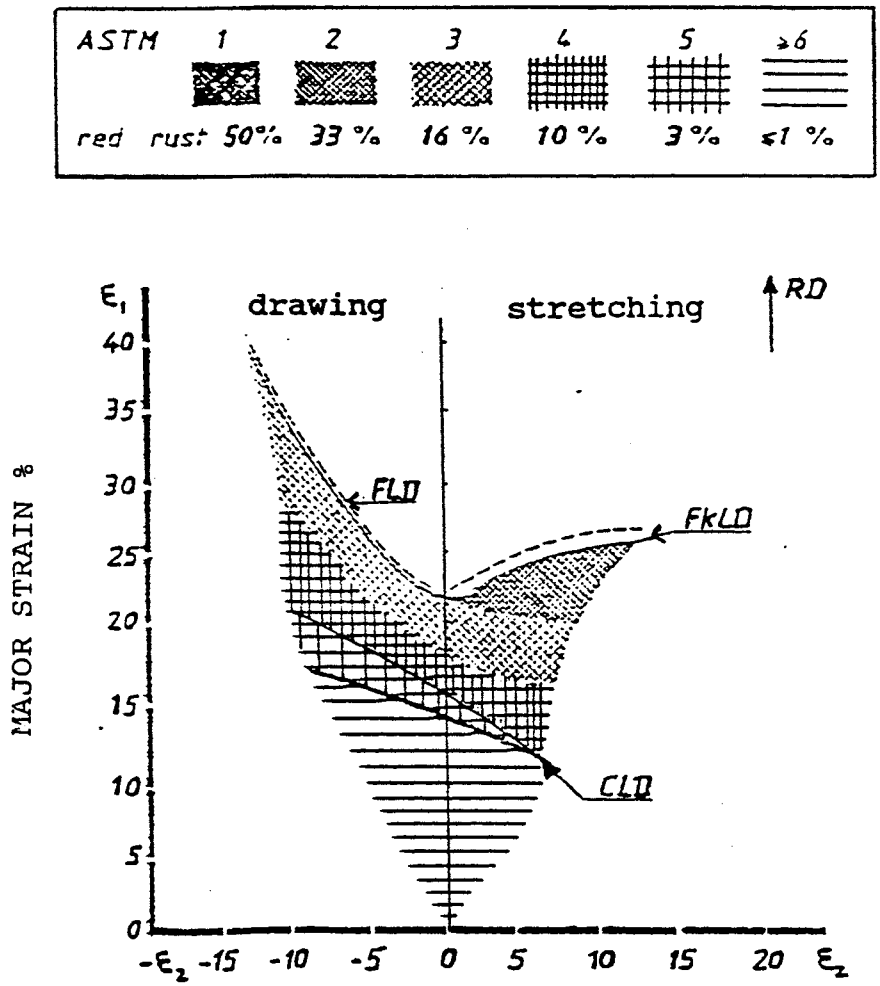

Figure 2 A formability diagram of hot dip galvanized steel which includes the cracking and flaking limit strains and the extent of corrosion (26). FLD-Forming Limit Diagram; FkLD-Flaking Limit Diagram; CLD-Cracking Limit Diagram

Robins et. al. (28) found that formability characteristics of coated sheet steels determined their cosmetic corrosion performance. Their corrosion evaluation included the scab and scribe tests, where panels were impinged with gravel or scribed to the metallic coating respectively. Such results once again emphasize the need to characterize the coatings in order to understand the formability and corrosion behavior of coated sheet steels.

2.6 Formability of Galvanized Steels

Sheet metal forming is a process that involves interactions between the material, tooling and lubricants and therefore a consideration of their properties is required to evaluate formability. Formability of coated sheet steels and effects of the coating on the formability of the steel have been studied by many workers (11,12,26,27,29-33). However, formability studies of precoated steel sheets without a consideration of deformation and fracture in the coating is not adequate since forming operations cause the coatings to crack or flake, thereby reducing the corrosion resistance (27,34).

2.6.1 Coating Deformation

Formability of coated sheet steels is limited by material failure which can be categorized as either bulk failure, i.e. necking, fracture, buckling, wrinkling etc., or surface failure due to the formation of defects. The latter failure type is pertinent to coating deformation and some of the surface defects which form include: i) cracking ii) flaking iii) powdering, and iv) galling. The fundamental mechanisms of formation of these defects have been extensively investigated (35,36). The following description of the defects is summarized primarily from the work of Makkimatilla and Ranta-Eskola (36).

When hot dip galvanized sheet is strained, a network of microscopic transgranular and intergranular cracks form even at small deformations, resulting in a distribution of independent coating particles adhering to the steel substrate. The subsequent plastic deformation of these particles is caused by shearing forces at the zinc-steel interface. If the coating adherence is inadequate, flaking occurs leaving unprotected steel.

Powdering produces coating debris due to microcracking

of a brittle surface layer that does not deform plastically to the required strain. Therefore, coatings with unfavorable crystallographic texture for slip are more prone to powdering. Powdering is a significant failure mode in alloy coatings with a limited number of slip systems. For example, Nakamori and Shibuya (37) found the powdering resistance of galvannealed coating sheet steels to be a function of the alloy phases present. They suggest that the presence of δphase (refer Table 2) is more detrimental for powdering than Γ phase.

In drawing operations adhesive friction between sliding surfaces (of the galvanized steel and the tool or die), resulting from a breakdown of the protective interfacial film, can produce flakes. If the adhesive junctions formed are strong the softer material is transferred to the opposite contact surface. This process is called galling. The asperities generated now carry the normal load between the contacting surfaces. Galling damage therefore increases with the normal load and sliding distance. A progressive buildup of coating material on die surfaces occurs during galling.

Fracture and flaking at the coating-steel interface

can occur at stress-free surfaces while powdering and galling need contact with a tool surface. Plastic deformation characteristics of crystals in the coating are critical in determining flaking and galling tendencies. This implies that both the microstructure of the coating as well as crystallographic texture are important considerations in surface defect formation. The applied stress state is another key factor that determines the type and extent of coating deformation. Belleau and Kelley (30) suggest that flaking is produced by compressive forces parallel to the surface while galling results from high normal pressures which promote sticking friction. In the presence of intermetallic phases in the coating and a compressive stress parallel to the substrate, powdering is favored over flaking due to low alloy ductility. Gronostajski and Ghattas (27) studied formability of hot dip coated steel sheets deformed by complex strain paths. They plotted the limiting strains in different strain paths, at which cracking and/or flaking of the coating occurred (Fig. 2). These cracking limit strains were much lower than forming limit strains of the base steel. Biaxial stretching produced cracks at random orientations in the coating. In contrast, in the work of Makkimatilla and Ranta-Eskola (36), biaxial strain (hydraulic bulging

tests) produced cracks in well defined crystallographic orientations in pure zinc and zinc alloy coatings. The difference in cracking behavior in the two studies could be a result of variations in coating texture.

The forming problems discussed thus far relate to coating deformation. However, in some coated sheet steels the formability of the base steel itself is affected during the coating process. For example, during hot dip galvanizing, Fe-Zn alloy layers are formed, primarily at the steel-coating interface. Formation of the alloy layer has been found to have very little effect on yield and tensile strength of the galvanized steel; while formability parameters like ductility, plastic strain ratio, limiting dome height (LDH) and strain hardening index, decrease with increasing alloy layer formation (31). The increased alloy formation is promoted by a post-dip heat treatment. This heat treatment also promotes diffusion of zinc to ferrite grain boundaries which causes intergranular embrittlement in the steel resulting in reduced formability (31,32). The Fe-Zn alloy layer also restricts straining in the sheet surface plane (31).

2.6.2 Friction of Coated Sheet Steels

Frictional behavior of zinc-coated steel sheets is markedly different from that of uncoated steel due to the lubricating effect of the zinc crystals. For example, hot dip galvanized steel was found to have a higher limiting drawing ratio (LDR) than cold rolled steel with the same plastic strain ratio (26). The increase in LDR was interpreted to result from a decrease in friction due to the presence of zinc. Gronostajski and Ghattas (27) also found variations in frictional behavior with different types of coating. This indicates that friction depends on the flow behavior of the coating. If this is so, texture should affect the frictional behavior of the material during forming operations.

The dependence of friction on the ductility of the coating is also illustrated in the work of Nakamura, Yoshida and Ishimoto (38). They studied the frictional characteristics of steel with different coatings: electrogalvanized pure zinc, electrocoated Zn-alloys and galvannealed. Frictional coefficients were monitored as a function of normal load, drawing velocity and oiling weight. Friction coefficients of electrogalvanized steel

sheets were very sensitive to variations in the above parameters, while the galvannealed steel sheets exhibited the least dependence on these factors. Their data are explained based on variations in drawing loads with changes in the tool-coating contact areas. The tool-coating contact area is a function of the ductility in the coatings. Ejima et al. (39) evaluated different precoated steels in stamping operations with reference to the extent of surface damage and frictional behavior. They found that in lab tests simulating forming conditions, the best precoated sheet steels were the Zn-Ni-Co and Zn-Fe alloy electroplated steels.

While material flow properties determine surface defect formation, lubricant characteristics determine the extent of surface strain in the coatings. The most effective lubricant promotes metal flow past the tool surface resulting in lower strain at the surface (10). In this respect a harder die material will also promote material flow at lower surface strains.

2.6.3 Evaluation of Friction Coefficients - A Bending under Tension Strip Drawing Test

Several tests have been developed to measure frictional properties of sheet steels (40). Some tests measure friction on sheet samples strained in the elastic region. Others measure friction while plastic deformation occurs on the sheet surface (40). The bending under tension type strip drawing test belongs to the latter category, and is used to evaluate friction coefficients of sheet steels, coated and uncoated. It was originally developed by Sulonen et. al. (41). The friction test is being extensively used (42) to characterize frictional properties of coated sheet steels.

In the bending under tension test a sheet metal strip is pulled over a cylindrical roll, shown in Figure 3. The pulling force, F_1, as well as the back-tension force F_2 are monitored during the test run. Strips are pulled over the roller twice in order to calculate a friction coefficient. The first test is one in which the roller is free to turn. A force balance leads to the equation

$$F_1^* - F_2^* = F_b \qquad [1]$$

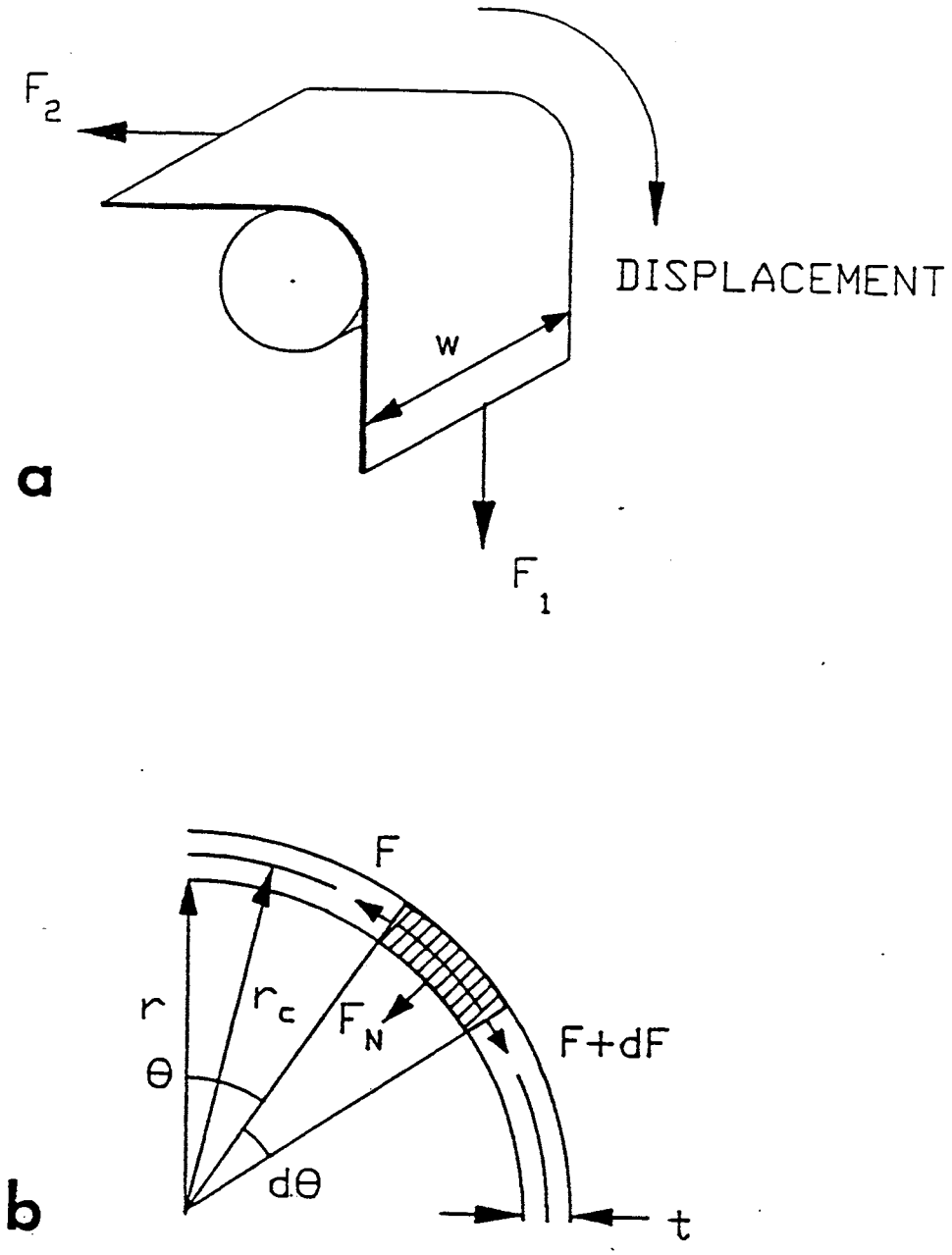

Figure 3 Schematic diagram of the bending under tension test roller and sheet metal strip geometry. Figure b shows forces in incremental portion of sheet metal strip (42)

where, F_1^* and F_2^* are free roller pulling and back tension forces respectively, and F_b is the force required to plastically bend the sheet metal strip. During the second test, the roller is fixed and both the plastic bending force, as well as the friction force must be overcome to pull the strip over the roller. A force balance for a fixed roller leads to

$$F_1 - F_2 = F_\mu + F_b \qquad [2]$$

where F_1 and F_2 are fixed roller pulling and back-tension forces and F_μ is the force required to overcome friction. F_b may be calculated from the previous test.

With proper integration over the arc of contact, the average contact pressure P and the coefficient of friction μ are given by

$$P = (F_1 + F_2)/2wr \qquad [3]$$

$$\mu = (2/\pi)\{(r + 0.5t)/r)\}\{\ln[(F_1 - F_b)/F_2]\} \qquad [4]$$

where, r = roller radius, t = sheet thickness, w = width

of the roller. This is for a 90^{o} contact angle between the sheet and roller. Coulombic friction and uniform pressure distribution over the roller is assumed. A more detailed derivation of these equations is presented by Sulonen's et. al. in reference 41.

In the bending under tension test, the coefficient of friction can be determined under conditions of varying imposed plastic strain. Also, the test conditions are easily varied, i.e, tool radius, lubrication methods and surface pressures may be controlled to simulate different forming conditions. Tool materials and surface conditions may also be easily varied.

The two equations of importance, Equations 3 and 4, give the average contact pressure generated in the friction test and the coefficient of friction under the given conditions, respectively. Contact pressure varies linearly with F_2, as long as F_1 is a linear function of F_2 (Equation 3). F_b, the force required to bend the sheet steel over the cylindrical roller, is constant for a given material. The corrected pulling force $(F_1 - F_b)$, is therefore a linear function of F_2. The friction coefficient μ is proportional to $\ln\{(F_1-F_b)/F_2\}$ in Equation 4, or

$\ln\{(C/F_2) + m\}$, where C and m are the y-intercept value and slope of the linear function between (F_1-F_b) and F_2. If C is 0, then μ is a constant with respect to changes in contact pressure or F_2. This situation is illustrated in Figure 4a. If C is positive, then at low contact pressures, μ increases with decreasing contact pressure as shown in Figure 4b. On the other hand, if C is negative, μ decreases with decreasing contact pressure, in the low pressure range (Figure 4c). At higher values of F_2, the ratio C/F_2 becomes insignificant and μ approaches the constant value given by (const.)*ln(m).

Variations in μ with contact pressure are not valid in a Coulombic friction regime. Therefore analyses based on Coulombic friction require the linear function between corrected pulling force (F_1-F_b) and back-tension to have a zero intercept value. Often, data generated do not give zero intercepts, and necessitate constraining the straight lines to go through the zero point. The justification for a linear fit between (F_1-F_b) and F_2 comes from the data measured in this work. A statistical analysis of the linear regression line through the data points gives sufficient confidence in this type of relationship between (F_1-F_b) and F_2.

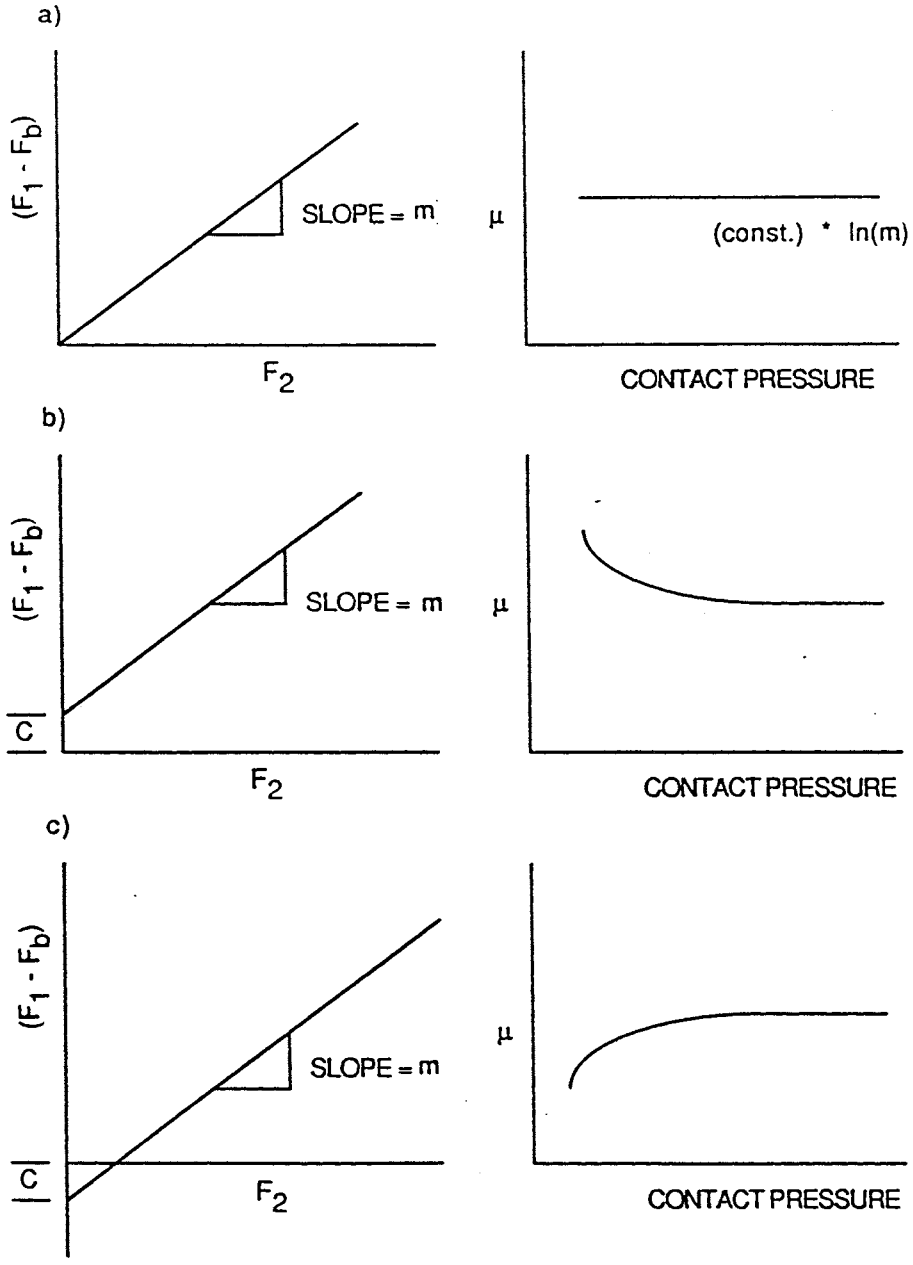

Figure 4 A schematic illustrating the different behavior of μ as a function of contact pressure for Coulombic friction in a bending under tension strip drawing test. (a) zero-intercept (b) positive intercept and (c) negative intercept

Equation 3 in the above analysis ignores variations in pressure over the contact area of the roller. Figure 5 from reference 43, addresses the issues on pressure distribution in sheet metal bending and unbending processes. The schematic in Figure 5a shows a sheet strip bent over a cylindrical roller. The arc of contact is less than one quarter of a cylinder due to elastic deflection of the sheet. Figure 5b plots the normalized pressure distribution over the arc of contact. Two pressure peaks exist at the entry and exit points of the region of contact between the sheet and the roller, as shown in Figure 5b. The difference between the peaks and valleys in pressure distribution can be as high as 20-30%. Therefore, the average contact pressure calculated in Equation 3, does not reflect a true situation. Furthermore, the true area of contact is restricted to roughness peaks on the surface, where the pressures will be significantly higher.

At high normal pressures Coulombic friction is invalid. This is illustrated in Figure 6, where the normalized friction shear stress is plotted as a function of the normalized contact pressure. The friction stress and the pressure were calculated on the basis of an apparent area of

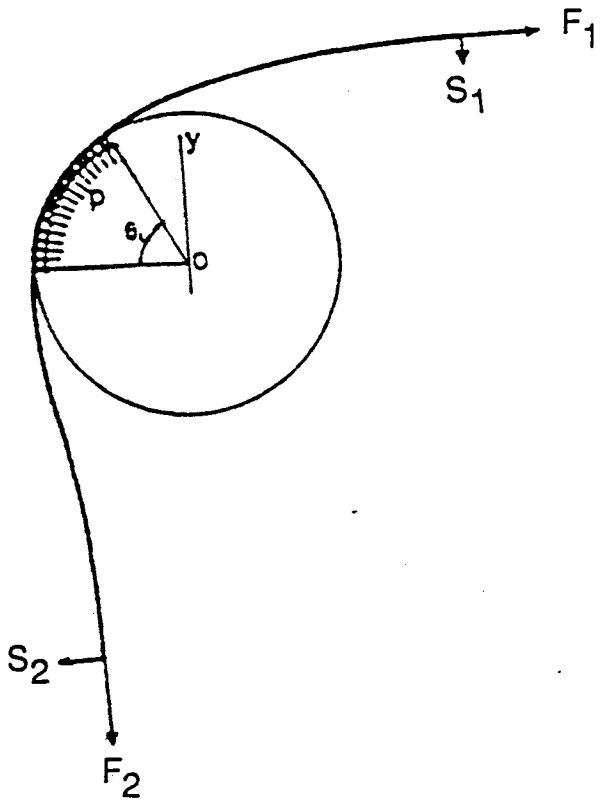

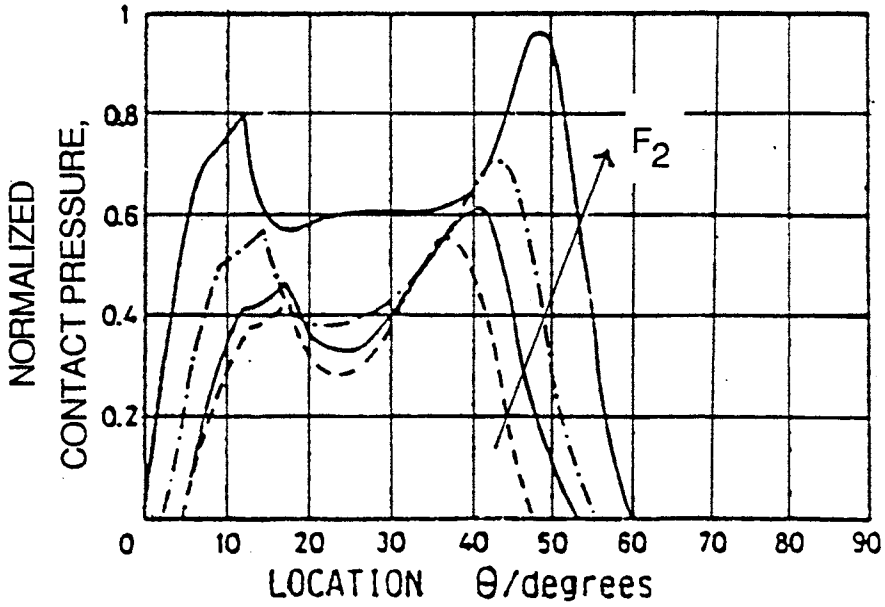

Figure 5 Contact pressure distribution over the arc of contact in sheet metal bending and unbending processes (43)

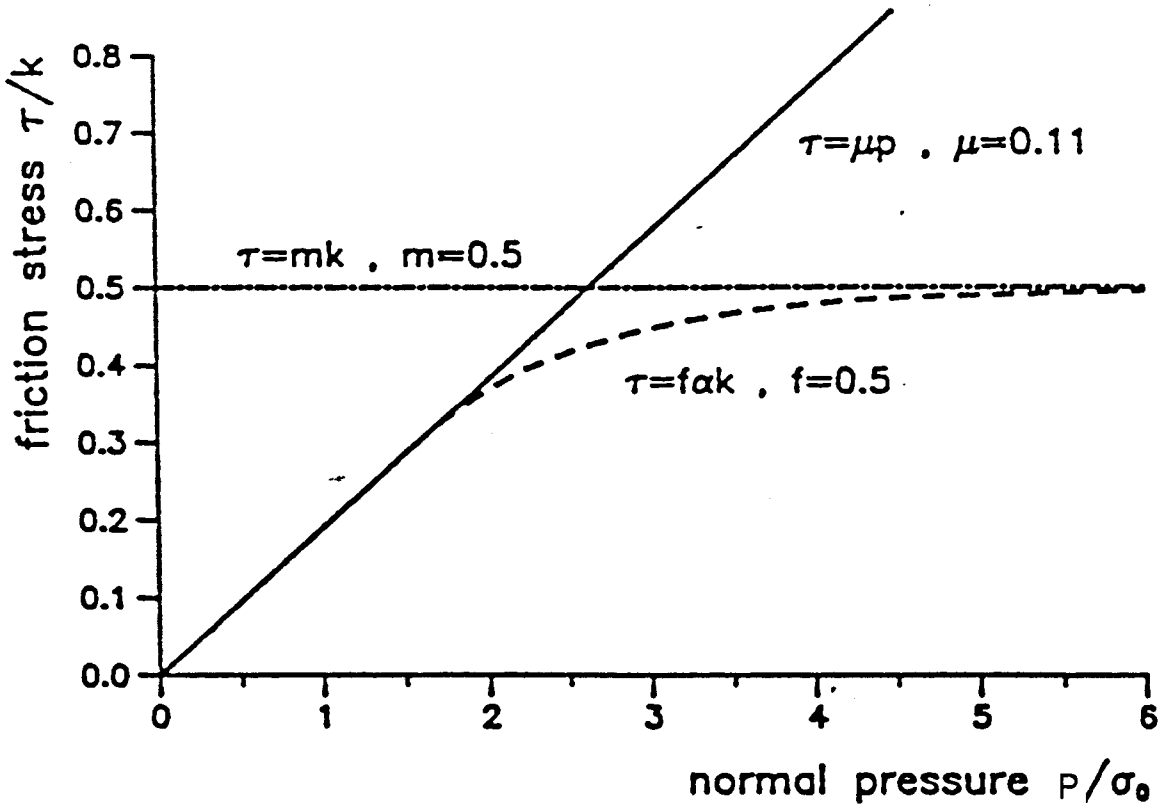

Figure 6 The behavior of friction stress (dashed line) as a function of the normal pressure in metallic friction for a system in which the maximum friction stress is limited by the material flow stress at the interface (44)

contact. The dashed line in Figure 6 represents experimentally observed variations in friction stress with contact pressure. The inclined straight line in Figure 6 describes the Coulombic friction model. In this model, the friction stress is a constant fraction of the applied pressure ($\tau = \mu P$). This fraction is called the coefficient of Coulombic friction, denoted as μ. As seen in Figure 6, Coulombic friction holds only at low contact pressures. The horizontal line in Figure 6 describes the constant friction model. Here the friction stress is a factor, m, of the shear strength of the material, k. m is called the "constant friction factor". This model is valid only at high contact pressures. In order to describe the real situation, a modified model comprising both these laws is required. Such a model would include the effects of material flow properties, asperity deformation and corresponding variations in true contact area, surface stress states and lubrication. A review of the modern theories of friction was undertaken to provide background material for such a model.

2.6.4 New Theories in Friction

Modern frictional theory emphasizes asperity

deformation on metal surfaces. Asperities are roughness peaks on a surface. They are characterized by the slope of the peaks and their density, as illustrated in Figure 7a. Figure 7a shows a smooth hard die surface and a rough soft coating surface prior to contact, while Figure 7b describes the situation after contact. After contact, the asperities deform, welded junctions in which the soft material bonds to the hard surface develop, and the indicated stresses are induced as sliding is initiated. Bowden and Tabor (45) established that the frictional force and the extent and type of surface damage during sliding depend on the physical properties of the sliding surfaces, especially the relative hardness of the two surfaces. On this basis, one can have a) hard metal sliding on a soft metal, b) the reverse of case a, and c) similar metals sliding. Figure 7 depicts the condition of a soft material sliding over a hard surface, which is of particular importance as it describes the bending under tension type strip drawing tests of galvanized coatings. Welded junctions are formed at points of contact, as indicated in Figure 7. McFarlane and Tabor (46) showed that both normal and tangential forces influence the deformation of these junctions at the interface. Under the initial contact load, asperities on the softer material deform plastically. In this condition very small tangential

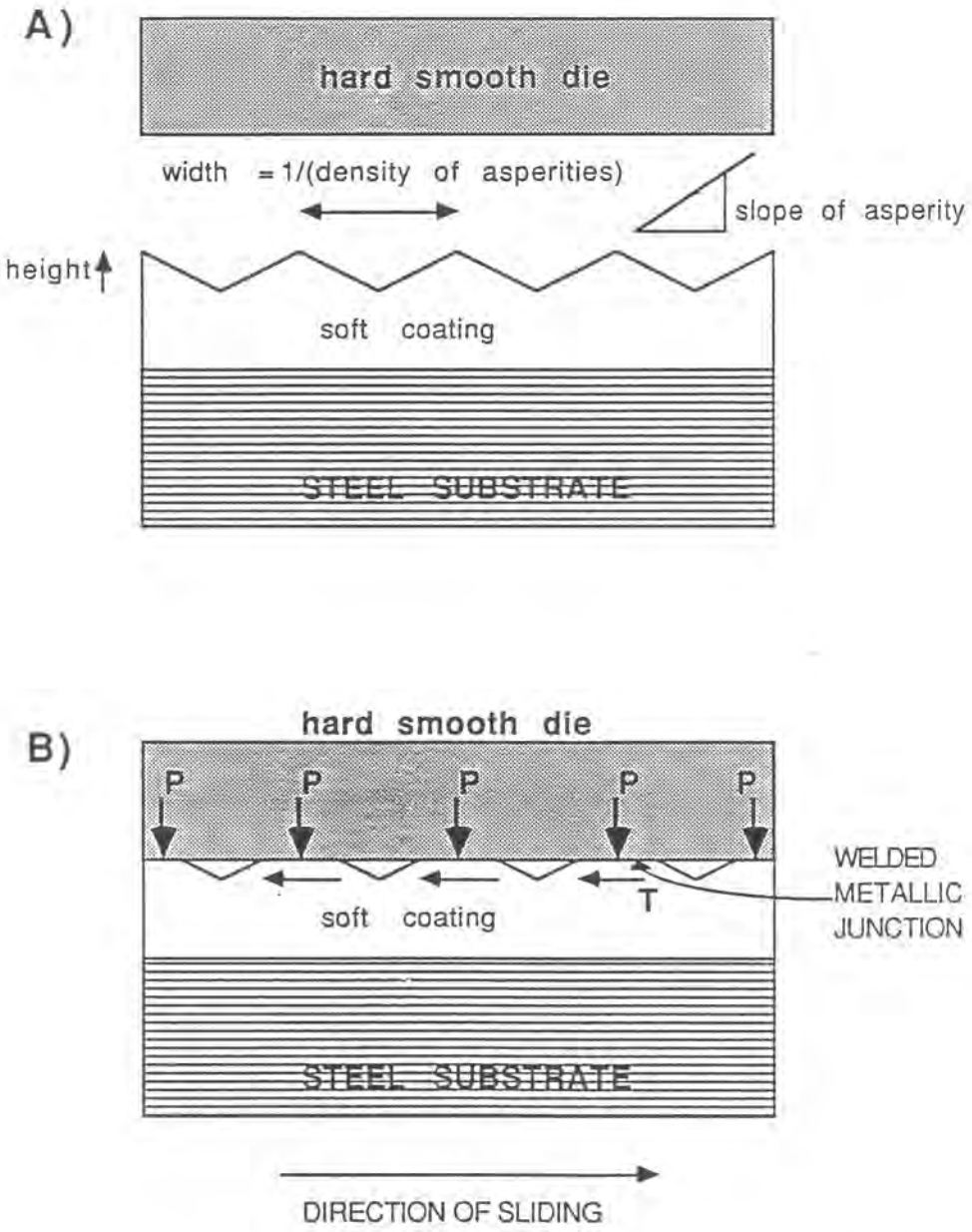

Figure 7 Schematic figures of a) asperities on a soft coating prior to contact with die, and b) welded junctions formed at die-coating interface after contact

forces are required to initiate microscopic sliding. During sliding, as the metallic junctions continue to deform, material flows around the regions of contact thereby increasing the true area of contact. For the same applied load therefore, the normal pressure decreases and shear or tangential force has to cause further flow. The regions of contact grow with sliding, accompanied by a corresponding increase in the tangential force required to continue sliding. A steady state is reached where the increase in tangential force is more rapid than the increase in the area of contact and macroscopic sliding occurs (46). Metallic junctions formed are responsible for friction and adhesion. Lubrication reduces the amount of metallic contact and leads to reductions in friction and adhesion (46).

Deformation of asperities can be monitored through a yield criterion such as the von Mises criterion. Application of von Mises equation requires knowledge of applied stresses, imposed constraints and material flow constants. This procedure will be detailed in the next section.

The initial analyses on asperity deformation by Bowden and Tabor (45) were followed by a number of other

investigations involving slip line field theory and the upper bound analysis. Wanheim and Bay (44,47) proposed a general friction model based on slipline analysis of asperity deformation which considers the effects of normal pressure, material flow properties, tangential stress, sliding length, asperity geometry, asperity deformation and the presence of entrapped lubricant.

In the next section studies on asperity deformation will be briefly reviewed. Following this review, the salient features of Wanheim and Bay's model for metallic friction will be presented.

2.6.5 Asperity Deformation Studies

Consider the example of a soft rough surface in contact with a hard smooth tool surface (Figure 7b). Contact is established at some of the asperities. The local pressures generated at these points are sufficiently high to cause plastic deformation even at small loads (45). The actual area of contact A is now given by the equation

$$A = W/p \qquad [5]$$

where, W is the applied load and p is the local pressure required to cause yielding. The value of p is 2k for simple compression without sticking or friction between the tool and the asperity, where k is the flow stress of the material in pure shear stress state. However constraints to material flow often raise the value of p. For example, Halling (48) has shown that for a model system of two cylinders in contact under plane strain conditions, the maximum shear stress at a subsurface point reaches a critical value k, when the maximum applied pressure P_o reaches a value of 3.1k. In this case the pressure distribution on the area of contact was semicircular, with the maximum in pressure occurring at the center, which is illustrated in Figure 8. At the point of maximum shear stress indicated in Figure 8, a plastic zone develops. As the load is increased, the plastic zone size increases and when the zone reaches the surface, the constraints on plastic flow are reduced. When the plastic zone reaches the surface, the deformation in the Halling (48) analysis can be viewed as an indentation. For indentation of surfaces the predicted mean pressures range between 4k and 6k (49). For hardness indentations, lower bound analysis predicts the pressure to be 4k. The upper bound estimate for this pressure is 6k while the slip line solution predicts a value of approximately 5.6k. Thus

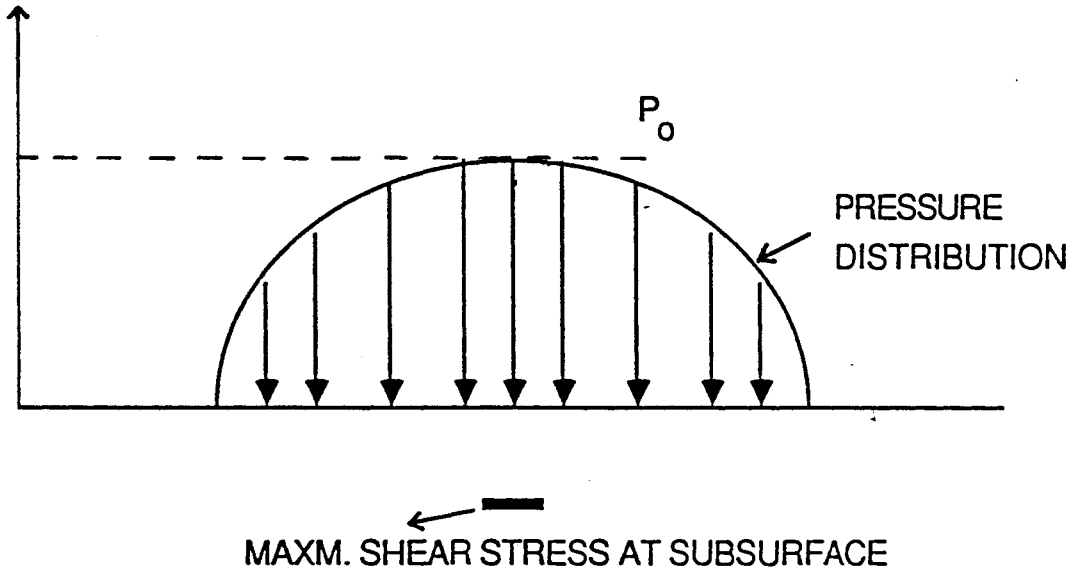

Figure 8 Schematic of a typical pressure distribution present during spherical ball indentations that produces maximum shear stresses at subsurface regions (48)

depending on the geometry of the plastic zone which develops between two contacting radii, the value of p in Equation 5 can vary between 2k and 6k. Once an appropriate value has been assigned for p, the real contact area can be calculated. Halling (48) has determined that for a case of a single rough surface in contact with a perfectly smooth surface (close to the example of zinc coating against the tool/die surface considered in this thesis), the relation between the load and the real area of contact is linear and independent of asperity heights, provided the asperities deform plastically with a constant flow pressure that is closely related to material hardness.

In order to cause sliding, welded junctions formed in the regions of contact need to be sheared, and the following analysis which ignores the complex stress-state at the interface can be used to approximate μ. If the shear strength of the welded junctions is given by s, and the contact area defined by Equation 5, then the frictional force F is

$$F = (W/p)s \qquad [6]$$

Therefore,

$$\mu = F/W = s/p \qquad [7]$$

For an ideal plastic material the local pressure to cause yielding, p, is approximately five times the critical shear stress s_m (i.e., k in the above analysis) in the bulk (49). If we assume $s = s_m$, then $\mu = 0.2$. However, for materials which cannot be approximated by an ideal plastic solid, s can also be associated with a specific interface shear strength, which may be different from s_m.

In general, plastic yielding under sliding conditions occurs in the presence of a complex stress state which involves a combination of the normal and tangential stresses. The stress state in a welded junction is illustrated in Figure 9. Figure 9 reflects one of the deforming welded junctions shown in Figure 7. For this condition, a plane stress state is assumed to describe the conditions within one welded junction. Application of the von Mises criterion (50) for the plastic flow of the welded junctions, gives the following relation

$$p^2 + 3s^2 = Y^2 \qquad [8]$$

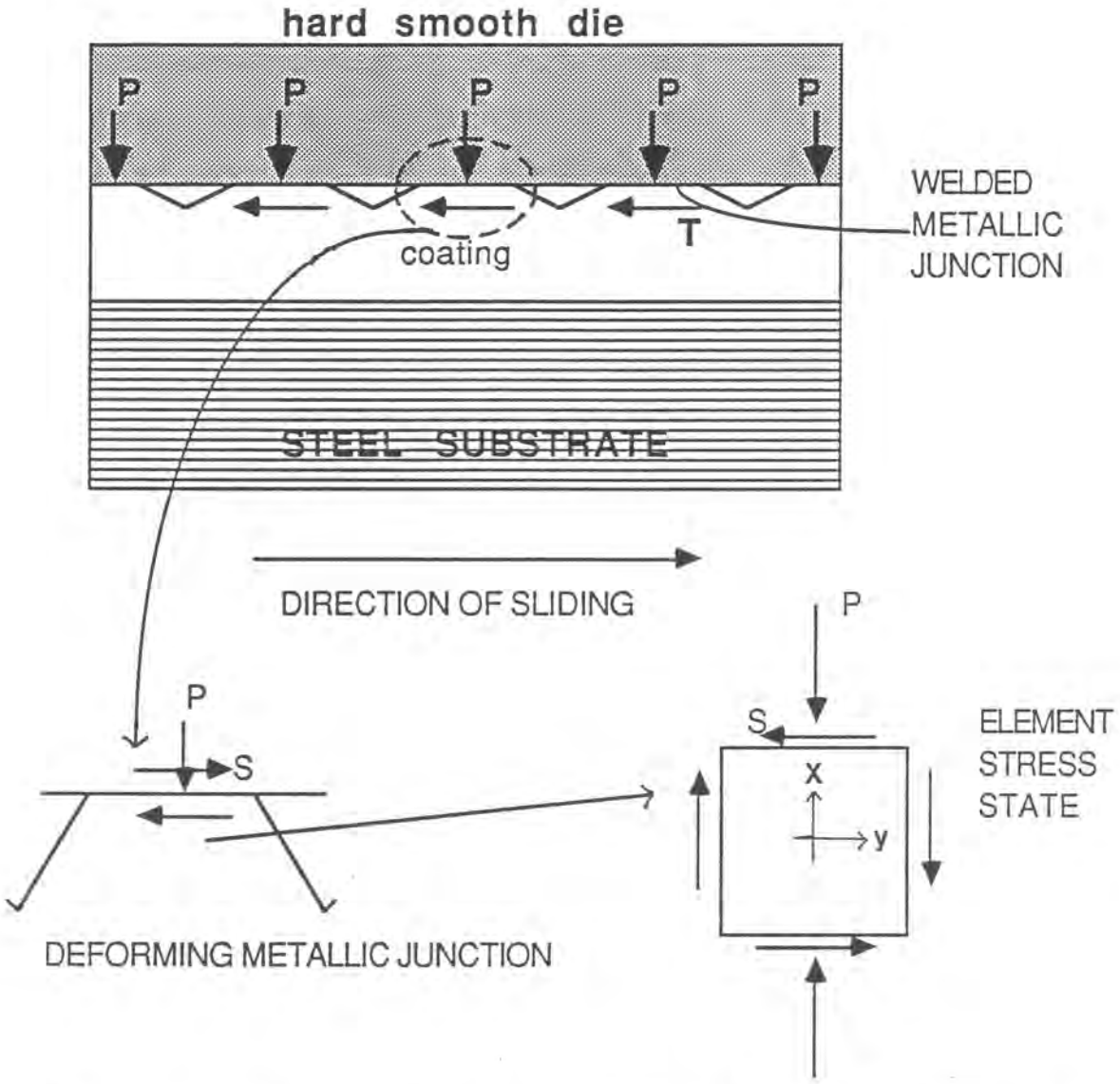

Figure 9 Stress-state in a welded metallic junction at the tool-material interface

where, Y = material constant, p = applied normal pressure, and s = applied shear stress. In experimental friction studies in which the true contact area is known, p and s can be directly calculated from external force measurements. The material flow constant, Y, is given by $\sqrt{3}(k)$, where k is the flow stress of the material in pure shear.

Material within a deforming junction in Figure 9 experiences constraint to flow from the surrounding material. The constraint manifests as additional compressive stresses in direction y. These additional stresses cannot be measured. Furthermore, they complicate the stress state, and Equation 8 becomes invalid. In order to avoid stresses that cannot be measured, and maintain a simple equation in the analysis, the effects of constraints on material flow are taken into account by altering the relation between p and s in Equation 8. Equation 8 can be rewritten as,

$$p^2 + \beta s^2 = Y^2 \qquad [9]$$

where, ß, a parameter which incorporates relations between stresses in a more complex stress state, needs to be determined. One has flexibility in the value of ß, which

can be used to reduce von Mises equations for complicated stress states into a form equivalent to the simple equation for plane stress state.

Equation 9 describes plastic flow in a junction mathematically. It does not provide an insight into the physical processes occurring during junction deformation, which is required to interpret some of the experimental observations made in friction studies. The following discussion will briefly describe the physical nature of junction deformation, followed by a continuation of the development of yield criterion equations.

As the shear stress is increased, microdisplacements occur due to increased flow of material. The size of the welded junctions and therefore the true area of contact increase with the applied shear stress. Growth of these junctions continues as long as the interface is strong enough to transmit the applied stresses. Macroscopic sliding initiates once the value of shear stress, s, reaches the shear strength at the interface s_m. When macroscopic steady state sliding occurs, junction growth stops, and the area of contact reaches a steady state value. This is seen in Wanheim and Bay's work (47), where the true area of

contact reaches the steady-state value fairly early in the sliding process. Figure 10, from reference 47, plots experimental measurements of the contact area ratio , (true area of contact/nominal area of contact) as a function of normalized sliding distance. The contact area ratio, , attains a steady state value early in the sliding process.

Green developed a theoretical analysis of the junction model for the cases of strong (i.e., ductile materials which exhibit strain hardening) and weak (i.e., brittle materials) junctions (51,52), and showed that due to the long life of junctions in ductile materials compared to brittle materials, the friction is higher in the former. Contaminant films reduced shear strength of the junctions and therefore reduced friction (51). Other workers extended Green's analysis of asperity deformation to many practical systems involving rough surfaces on the die and work piece (53-55). Tabor (56) modified his (45) initial asperity deformation model to account for interfacial films separating surfaces in contact regions. The film strengths ranged from zero (perfect lubrication) to the shear strength of the asperities (strong junctions).

The above modeling work provides several methods of

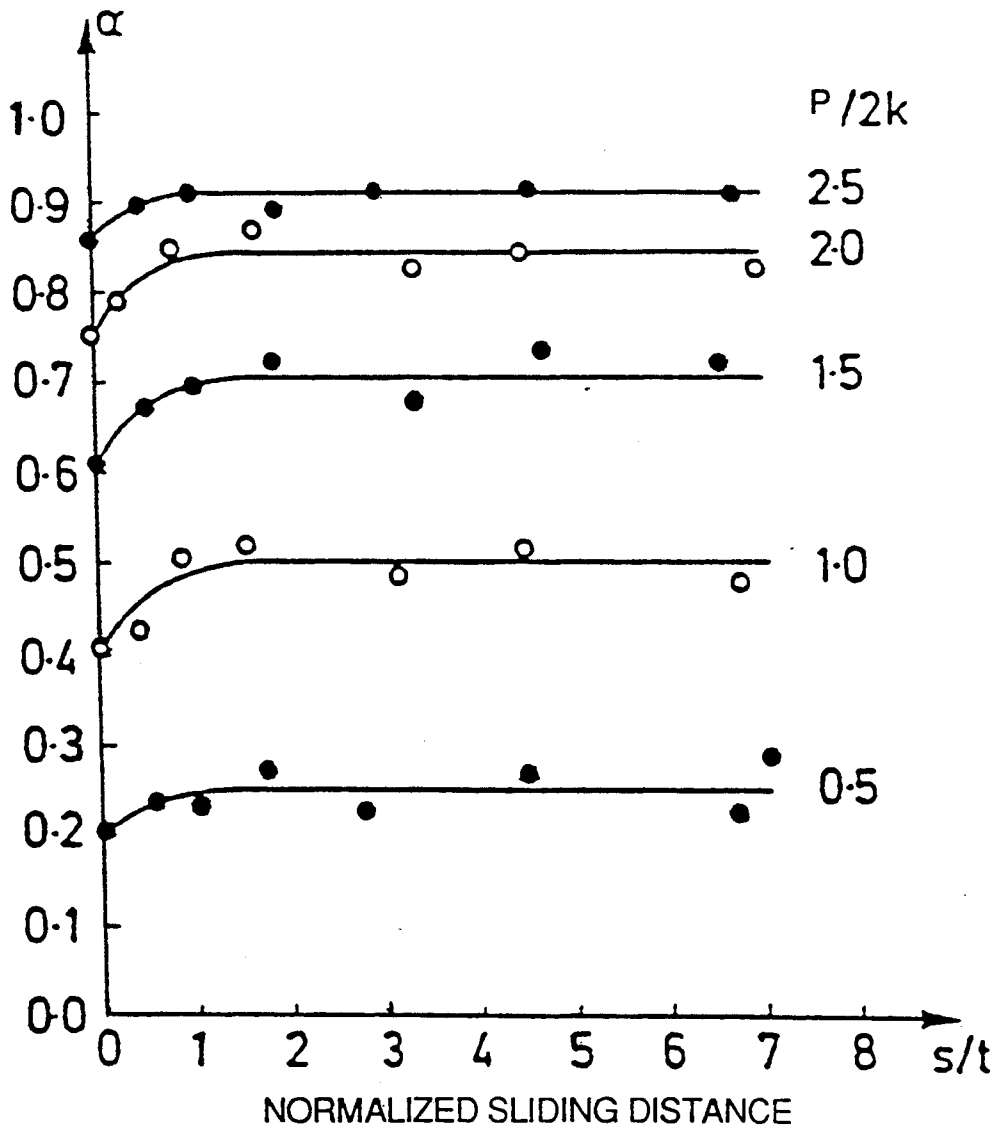

Figure 10 Experimentally measured true contact area ratio α, as a function of sliding distance (47)

looking at physical deformation of a welded junction. The one approach that has been described in detail, in this work, is the application of von Mises yield criterion to a plasticly deforming junction. The development of this approach will now be continued.

Rubenstein (57), expanded the asperity deformation model to include work hardening of materials (non-ideal plastic behavior). He assumed an exponential law to describe the true stress-strain curve for ductile materials. Consequently, Y changes with strain. The yield equation for the junction takes the form

$$p^2 + \beta s^2 = (\text{const.})A_p^{\,x} \qquad [10]$$

where, x is the strain hardening exponent, A_p the true area of contact,and p and s are the true stresses. If α is the ratio of true area of contact to the apparent area of contact, and P and S represent nominal (i.e., defined over the total apparent area) normal and tangential stresses, then Equation 10 can be rewritten as

$$P^2 + \beta S^2 = (\text{const.})A_p^{\,x}\alpha^2 \qquad [11]$$

Equation (11) is a direct relation between and the stress state that can be used to predict true areas of contact under combined shear stress and pressure, prior to the onset of macroscopic sliding. Rubenstein also suggested that ß is constant for a fully work hardened material (57). If the applied shear stress becomes equal to shear strength at the contact region before the material is fully work hardened, ß becomes pressure dependent and loses significance (57). For a partially work-hardened material if the shear stresses are less than the interface shear strength long enough for the contact regions to fully work-harden, ß stays constant.

Even though, equation 11 suggests a way of predicting as a function of contact pressure, p, practically it is not possible to do so unless precise values are determined for ß and x. There is a large variation in reported values of ß (49). x needs to be determined for each material of interest, under the conditions of the test. Therefore, the approach discussed above to predict may not be simple and accurate. Wanheim and Bay predicted values for based on slipline analysis of asperity deformation. Their results are presented in the next section and used as a theoretical basis for the study of friction on coated sheet steels. Later, experimental measurements of α will be presented

which support Wanheim and Bay's predictions.

2.6.6 Wanheim and Bay Model for Metallic Friction

In the general friction model of Wanheim and Bay, the nominal friction shear stress is given by

$$\tau = f\alpha k \qquad [12]$$

where, f is a measure of adhesive bonding at the interface, α is the fractional true area of contact, and k is the flow stress in pure shear. For pure sticking friction, f = 1. f differs from the friction factor, m, in the constant friction stress model in that, the effects of true areas of contact and asperity geometry are not included in f. The influence of true areas of contact on friction stress is incorporated in α, which is the true contact area ratio (true contact area/apparent contact area). α depends on f, k, asperity geometry and the contact pressure. In Equation 12, f and k are constants for a given workpiece material and tooling, and α is experimentally measurable. Determining α as a function of contact pressure will help in the estimation of friction stress as a function of contact pressure.

In order to evaluate α, slipline field theory solutions were developed for asperity deformation at low pressures where the deformation zone of each asperity is isolated and at high normal pressures where the deformation zone in an individual asperity overlaps the deformation zone of the adjacent asperity. Asperity deformation was modeled by considering flow strength, normal pressure, friction factor and asperity slope, as the primary factors controlling slipline field theory solutions. Predictions of the contact areas as a function of contact pressure were obtained. Controlled asperities on surfaces were deformed in the experimental setup of Wanheim and Bay, and their deformation monitored for comparison with theory. The experimental design and theoretical calculations are explained in references 44 and 47 respectively.

Wanheim and Bay's theoretical predictions are summarized in Figures 11 and 12. Figure 11 plots the predicted increase in the fractional true contact area with normal pressure for different friction factors. The true contact area ratio increases linearly with pressure up to a certain limit. At higher pressures the ratio approaches unity,for dry sliding conditions. For lubricated systems,

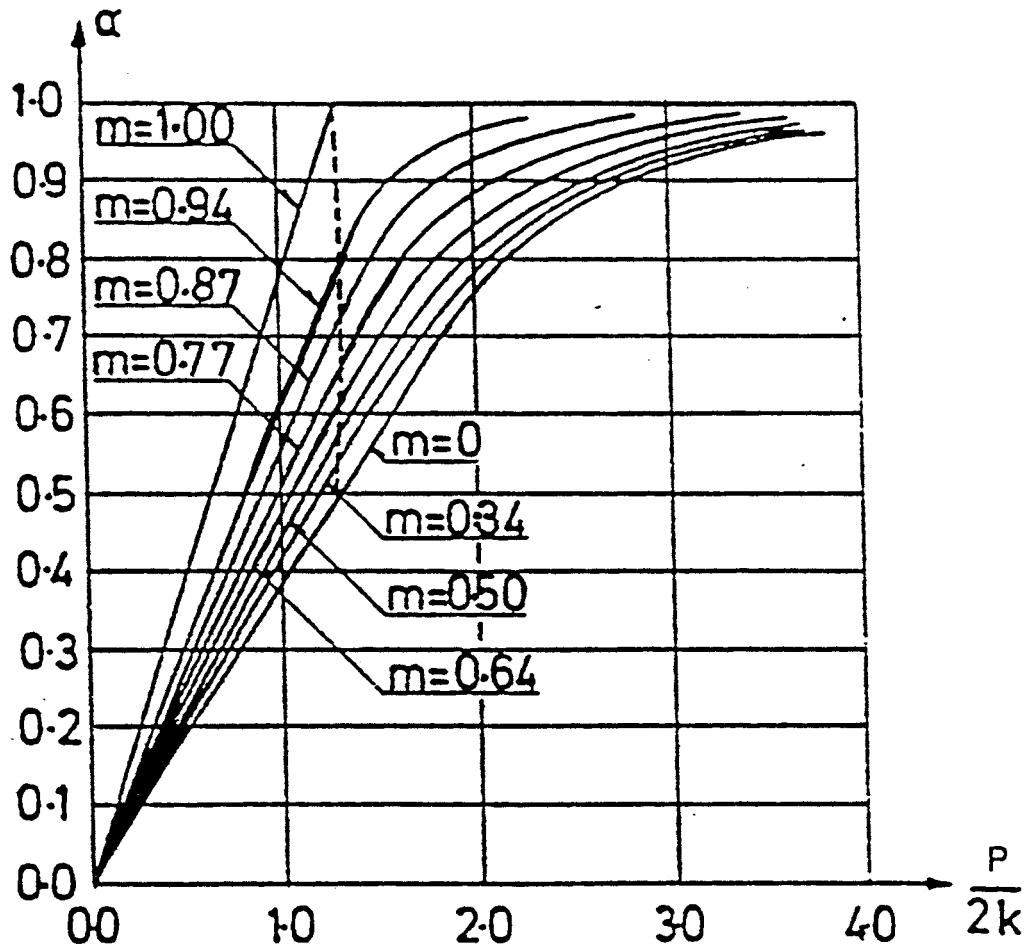

Figure 11 Predicted true contact area ratio α, as a function of the bond strength factor f and the nominal contact pressure, in metallic friction (47)

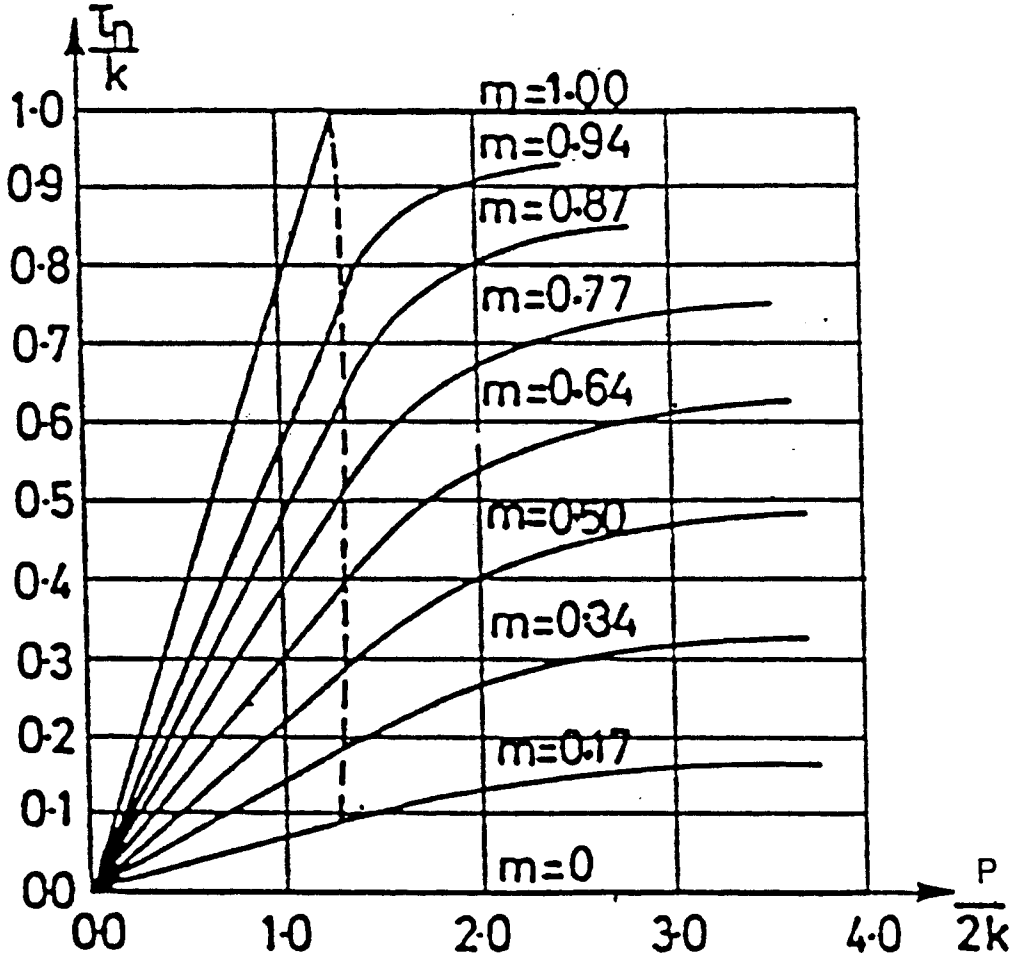

Figure 12 Predicted nominal shear stress as a function of the nominal contact pressure and bond strength factor f, in metallic friction (47)

presence of trapped lubricant will physically prevent α from attaining a value of 1. Figure 12 plots the corresponding shear stress or friction stress as a function of the normal pressure. The friction stress is calculated from equation 12, once values for f and α are known from Figure 11. The friction stress is a linear function of normal pressure up to the pressure limit indicated by the dashed vertical line in Figure 12. Within this range, Amontons law [$\tau = \mu p$] applies. Beyond this limit, the friction stress reaches a limiting value asymptotically. The limiting value is given by $(\tau/k)_{max.} = f$, the assumed friction factor. This behavior of the friction stress is closer to reality. Once the limiting value of friction stress has been reached at the higher pressures, the constant friction model is valid. Neither Coulombic friction nor the constant friction is applicable in the intermediate pressure range, i.e, the transition zone.

Asperity slopes change during deformation. In the presence of friction, the two slopes on either sides of an asperity are no longer symmetrical, since the stress field is asymmetrical (44). When the bond strength factor, f, reaches a value close to 1, stress equilibrium is not achieved and asperities will continue tilting in the

direction of sliding, until the gaps between asperities are filled and real contact area reaches the nominal value, even at relatively low normal pressures. In the absence of complete sticking friction ($f < 0.9$), the real contact area reaches the nominal value only at relatively high normal pressures. Also, in the presence of sliding, fairly early in the sliding process the real area of contact attains a steady state value for the given pressure condition, as shown in Figure 10 (47).

Wanheim and Bay (47) showed that trapped lubricants caused an increase in the normal pressure required to obtain the same area of contact compared to a case where the lubricant is absent. Lubricant bulk modulus, normal pressure and metal flow stress are the main parameters which determine α.

In Figure 12, the limit of proportionality between the friction stress and the normal pressure is at a value of 1.3 for the (P/2k) ratio. Therefore for $P/2k < 1.3$, μ has a constant value, which can be calculated by estimating the slope of the lines in Figure 12. The relation between μ and f, derived from Figure 12, is shown in Figure 13 (47). For $P/2k > 1.3$, μ becomes pressure dependent and loses

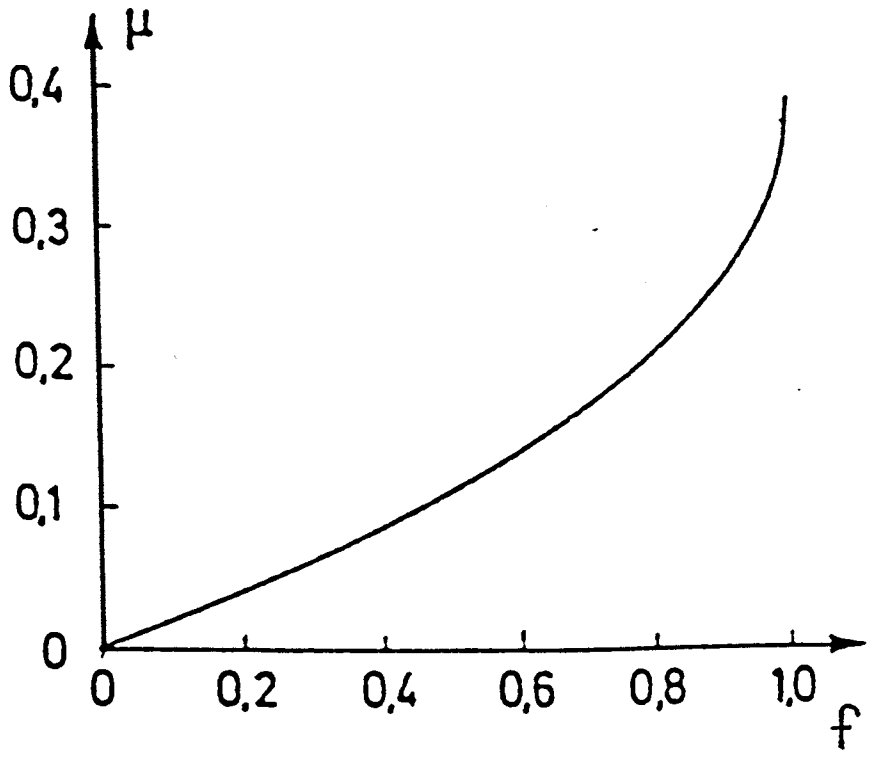

Figure 13 Relation between the friction coefficient μ and the bond strength factor f, calculated from Figure 12 (47)

significance in analysis. If Coulombic friction is assumed valid in the high pressure range (i.e., $p/2k > 1.3$), the value of μ will decrease with increasing values of p. The maximum limit for μ in Figure 13 is 0.39, which is the same limiting value reported by Alexander (58) in the plane-strain compression of a plastic-rigid material.

2.6.7 Summary of the Understanding Gained from Asperity Deformation Studies

The asperity deformation studies considered so far in the analysis of friction are summarized below. For the case of a smooth hard surface contacting asperities on a rough soft surface, pressures generated at the points of contact are sufficiently high to induce plastic deformation, and the contact area is determined by the flow strength of the deforming material; when shear stresses are introduced, further plastic flow occurs, increasing the contact area. For the same applied load, pressure drops and shear stress has to be increased to meet the yield criterion. With an increase in the tangential force, the shear stress reaches the shear strength of the interface, at which point macroscopic sliding occurs and junction growth stops. Thus the true area of contact reaches a steady-state value fairly

early in the macroscopic sliding process. The bond strength factor, f, also influences the true area of contact and the nominal shear stress values. During sliding at a given nominal pressure σ attains a higher value, for a higher f, thereby increasing the tangential force (and thus stress) necessary for sliding. This explains why the nominal shear stress in Equation 12 is of the form $\sigma(fk)$. The limiting value of shear strength at the interface must be equal to fk, which is reached at higher pressures. Correspondingly, the limiting value of $(\tau/k)_{max}$ is f, in Figure 12. When f = 1, complete sticking friction exists, and higher tangential stresses are required to cause macroscopic sliding. In the presence of contaminant films or lubricant films the value of f decreases due to a reduction in the extent of adhesive bonding at the workpiece-tool interface. As a result, junction growth at the workpiece-tool interface stops earlier since critical shear strength at the interface is reached earlier. This implies that the true area of contact is less compared to a dry sliding condition for the same load. Shear strengths in the presence of lubricants can be calculated by a rule of mixture, once the true area of metal-metal contact is known (59). This approach is valid for a mixed regime, where the lubricant film thickness is such that a significant fraction of the load is supported

by contact at roughness peaks (59,60).

2.6.8 Factors Influencing Friction

The frictional property of a material surface can be influenced by many factors. Some of these factors are external to the material itself and include imposed stress state, contact pressure, surface properties such as roughness, lubrication, sliding speed and other process parameters. Friction is determined by the material response to these imposed conditions, that is, the surface flow and fracture behavior. The flow and fracture behavior of the coating is a function of crystal structure, strength, ductility and texture. Ultimately these are some of the material factors that influence friction and coating deformation. Of these, texture and crystal structure (with associated variations in strength and ductility) are important factors in determining friction on coated sheet steel surfaces. In the following sections a review of the available information on the effects of these variables on friction is presented along with the results of experiments designed to evaluate the significance of each in controlling the frictional properties of coated sheet steels.

2.6.9 Effect of Crystallographic Texture and Crystal Structure on Friction

Studies on surface and sub-surface deformation (61-65) illustrate the importance of material flow and fracture behavior in friction. Texture affects material flow behavior and will therefore play a role in determining frictional properties of materials. The effects of texture on friction are pronounced in metals with a hexagonal close packed structure of atoms (HCP). Buckley and Johnson (66) showed that for HCP metals exhibiting slip predominantly on basal plane, friction coefficients were lower on the basal planes, compared to prismatic planes $\{10\bar{1}0\}$ (66). Further, friction was lower when sliding occurred along one of the slip directions. Buckley and Johnson (66) also suggested that surface recrystallization and subsequent texturing were taking place during sliding. The loads and sliding speeds encountered in many engineering applications cause high levels of local deformation and high surface temperatures. These conditions promote recrystallization at the surface, which has been observed in many metals (66). Recrystallization in a single crystal, introduces grain boundaries and increases the shear strength of the material. This results in an increase in the coefficient of

friction (66). On the other hand, for a random polycrystalline material dynamic recrystallization and subsequent texturing could result in a lowering of the friction coefficient (66).

Buckley and Johnson (66) also evaluated the role of crystal structure on friction. Increasing the number of slip systems will result in higher ductility and therefore higher friction. Copper having a face centered cubic structure of atoms (FCC) with twelve active slip systems at room temperature and provision for cross-slip exhibits higher ductility than some of the HCP metals. This factor becomes important since it influences the true area of contact (66). The second factor involved in friction especially in the mixed or boundary lubrication regime is the shear strength of the metal junctions. With HCP single crystals that have extended regions of easy glide and negligible work hardening, less force is required to fracture the junctions. For FCC metals, extensive plastic deformation and work hardening results in an increase in shear strength (66). Thus, FCC metals exhibit higher friction coefficients compared to HCP crystals. Polycrystalline materials will in general exhibit higher friction coefficients compared to single crystals of the

same material, except in the case of a textured surface (66). It must be realized that within a very thin layer of the order of surface roughness, a significant deformation gradient develops with a high strain at the surface (62).

The experiments of Buckley and Johnson (66) were performed under conditions of high vacuum (10^{-9} - 10^{-7} torr), with single crystal riders sliding on a polycrystalline disk of the same material. Here the main component of friction is the shear at the interface. With rider and disk made of different materials of varying hardness, plowing may become significant. The effect of surface texture is less significant under such conditions due to the influence of the orientation of many other planes in the crystal on friction (66). Plowing is important when a hard rider or asperity slides on the surface of a soft metal such as copper. Komvopoulos et. al. (67) have shown that plowing predominates friction in boundary lubrication regime. However, their experiments were also performed with pin and disks made of the same material. The materials tested were polished aluminum, copper and chromium, using mineral oil lubricant (67).

3.0 EXPERIMENTAL DESIGN

An ideal coating should exhibit significant resistance to both fracture and corrosion. The coating should not only afford good barrier protection but also form passive corrosion products in the regions where the steel substrate is exposed. Sufficient ductility in coatings will ensure fewer cracks when deformed. Ductility will be achieved by a favorable combination of texture and microstructure. A favorable stress state is one which promotes plastic flow in the coating. Practically, a combination of an ideal coating material subjected to a favorable stress state will be rarely encountered. Therefore, in many cases, formability and corrosion performance of coated sheet steels depend on the deformation behavior of the coatings under a non ideal combination of several variables such as:

1. texture
2. microstructure
3. material strength
4. thickness
5. grain size
6. surface roughness
7. imposed stress state, and

8. type of lubrication and die material

Considerable amount of coating evaluation work has been published. Most of the published work presents results of either a corrosion or a formability evaluation. In some cases corrosion performance of deformed coated sheet steels have been studied. However, a clear understanding of the reasons for observed coating behavior under different conditions is lacking. A fundamental model linking coating performance to coating properties and applied stress states would help, not only in interpreting the results of several performance evaluation tests, but also in predicting coating behavior under new service conditions. Such a model would also help in the design of suitable coatings for improved formability and corrosion performance. This work attempts to gain a fundamental understanding of the effect of above mentioned variables on deformation of the coatings.

In order to obtain a conceptual understanding of coating deformation, a set of schematics showing deforming zinc grains on a steel substrate will be presented in the next section. Deformation behavior of zinc grains, in these schematic figures, will be predicted as a function of

stress state, texture and crystal structure (zinc alloys). The understanding gained from this approach will then be used as a basis to devise an experimental procedure to test coating deformation behavior and its influence on friction.

3.1 Conceptual Understanding of Coating Deformation and Its Influence on Friction

Consider the schematic in Figure 14, depicting zinc grains on a steel substrate. For simplicity, single grains are shown to occupy the entire thickness of the coating. The orientation in grains A and B are different as shown by the tilt of the primary slip planes in zinc, the HCP basal planes (the plane highlighted in each grain). Assume that the mode of failure in these coatings is intergranular fracture. Upon application of a uniaxial tensile stress without the concurrent application of a normal contact pressure, grain A can plasticly deform to accommodate strain, while grain B is unfavorably oriented for slip. A crack will therefore form at the A-B grain boundary as shown in Figure 14b. Now consider a change in stress state by adding a normal compressive force perpendicular to the coating surface as shown in Figure 15. The application of the normal force will contribute towards increasing the

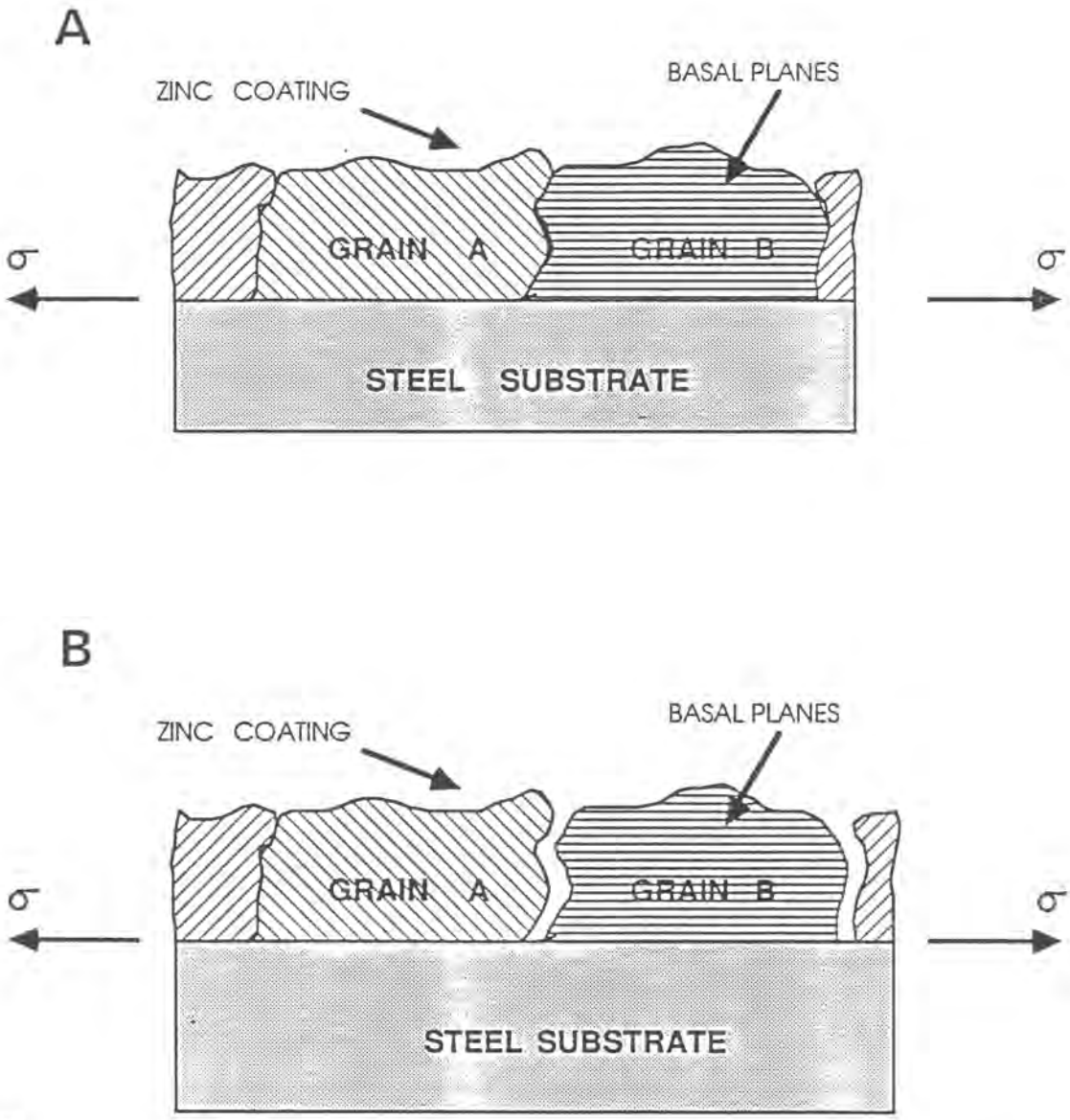

Figure 14 Zinc grains of differing orientations on a steel substrate subjected to tensile stress parallel to coating surface. Grain B is unfavorably oriented for slip

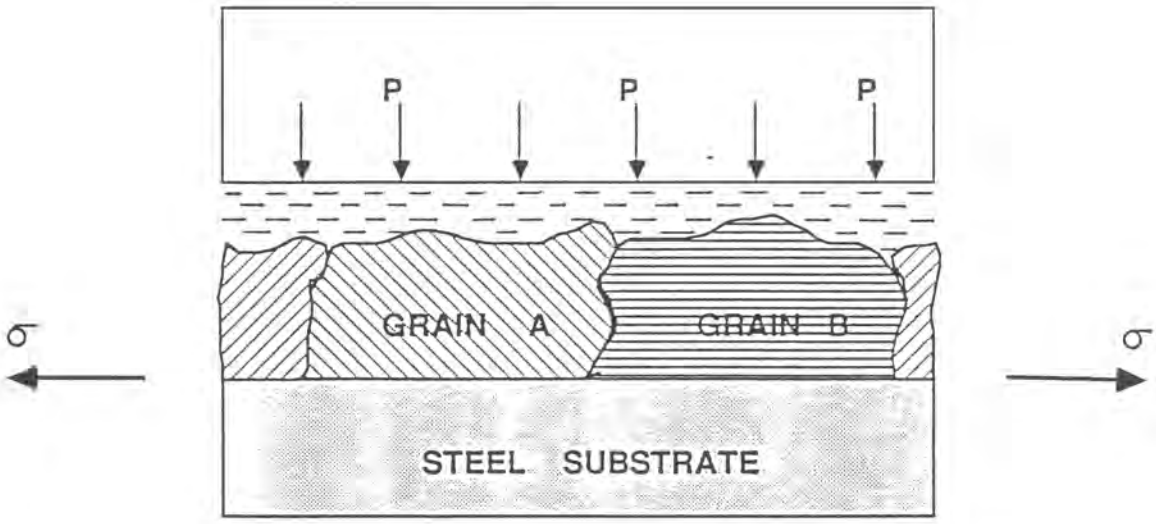

Figure 15 Zinc based coating on steel subjected to a normal compressive pressure and a tensile stress parallel to coating surface. Grain B is unfavorably oriented for slip in the absence of a normal pressure

value of maximum shear stress which occurs on planes inclined at 45^{o} to the surface. This could lead to secondary slip in the grains, thus avoiding intergranular cracking. A compressive stress perpendicular to the basal planes promotes twinning in zinc (Appendix A). Twinning can reorient grains such that primary slip can take place in the twin region. To interpret the effects of normal pressure on flow in coatings which exhibit limited slip either due to texture or crystal structure, consider the hypothetical change in coating texture (as measured by normalized X-ray peak intensity ratios (68)) with normal pressure for two coatings, a zinc coating with basal planes parallel to surface and a zinc-alloy coating. The hypothetical changes are illustrated in Figure 16. In Figure 16, the solid line represents texture changes in a pure zinc coating, where at some critical pressure twinning occurs which is followed by plastic flow and texture changes. The dashed line represents hypothetical texture changes in an alloy coating, where at some critical pressure conditions for slip are satisfied. Note that the pressure applied in Figure 16, promotes plastic flow over cracking.

Intergranular cracking can cause isolated zinc grains adhering to the steel substrate as shown schematically in

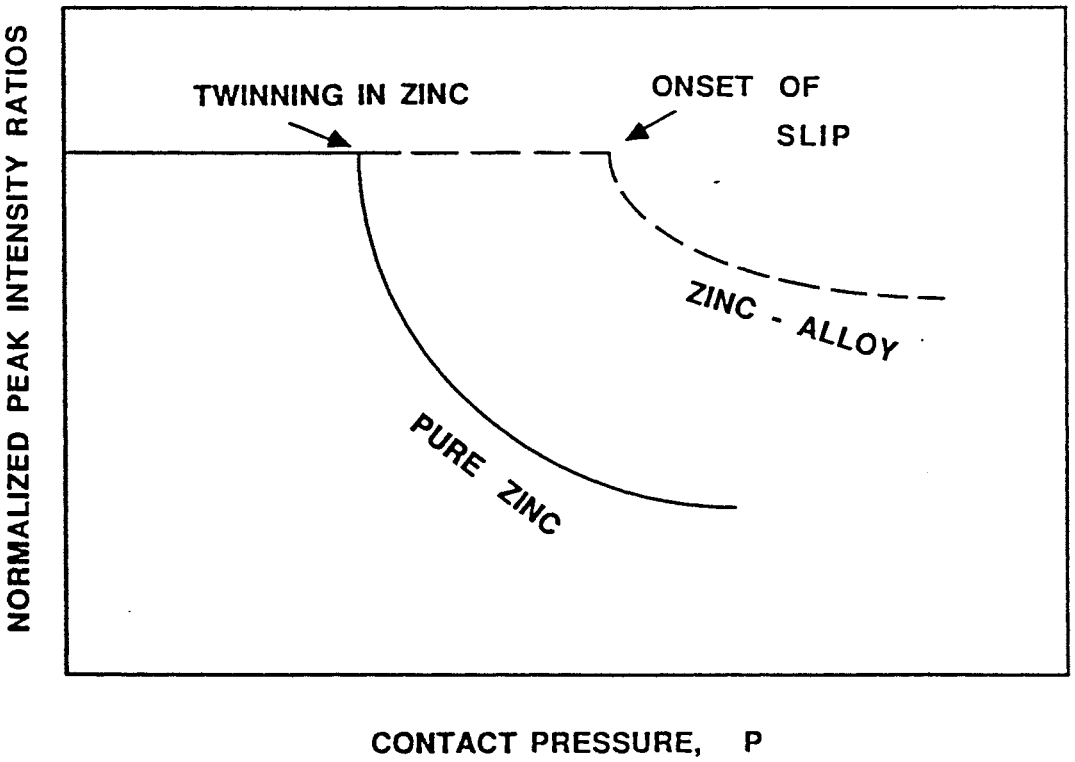

Figure 16 Texture or peak intensity change in Grain B (in Figure 15) as a function of normal compressive pressure

Figure 17. Typically intergranular cracking is promoted in brittle coatings, for example a hot dip pure zinc coating with unfavorable texture for plastic flow or a hot dip zinc alloy coating with multiple layers of intermetallic phases. In both these coatings, there is at least a thin intermetallic layer adjacent to the steel-coating interface. Figures 17b and 17c show two types of cracking that can occur in isolated grains of such coatings. Both modes of failure start with the cracking of the intermetallic layer adjacent to the interface, due to its inability to flow with the steel. The cracking of the intermetallic layer adjacent to the interface will continue in a hot dip pure zinc coating until the fractured particles are small enough that the loads transferred at the interface are insufficient to break these particles any further. The cracks originating at the interface propagate through the grain to the free surface if the coating material is completely intermetallic, as is the case in alloy coatings (Figure 17c).

Surface defects which develop as a result of forming are a function of the material flow properties and imposed stress states. Consider another area of concern in forming, where material properties play a significant role.

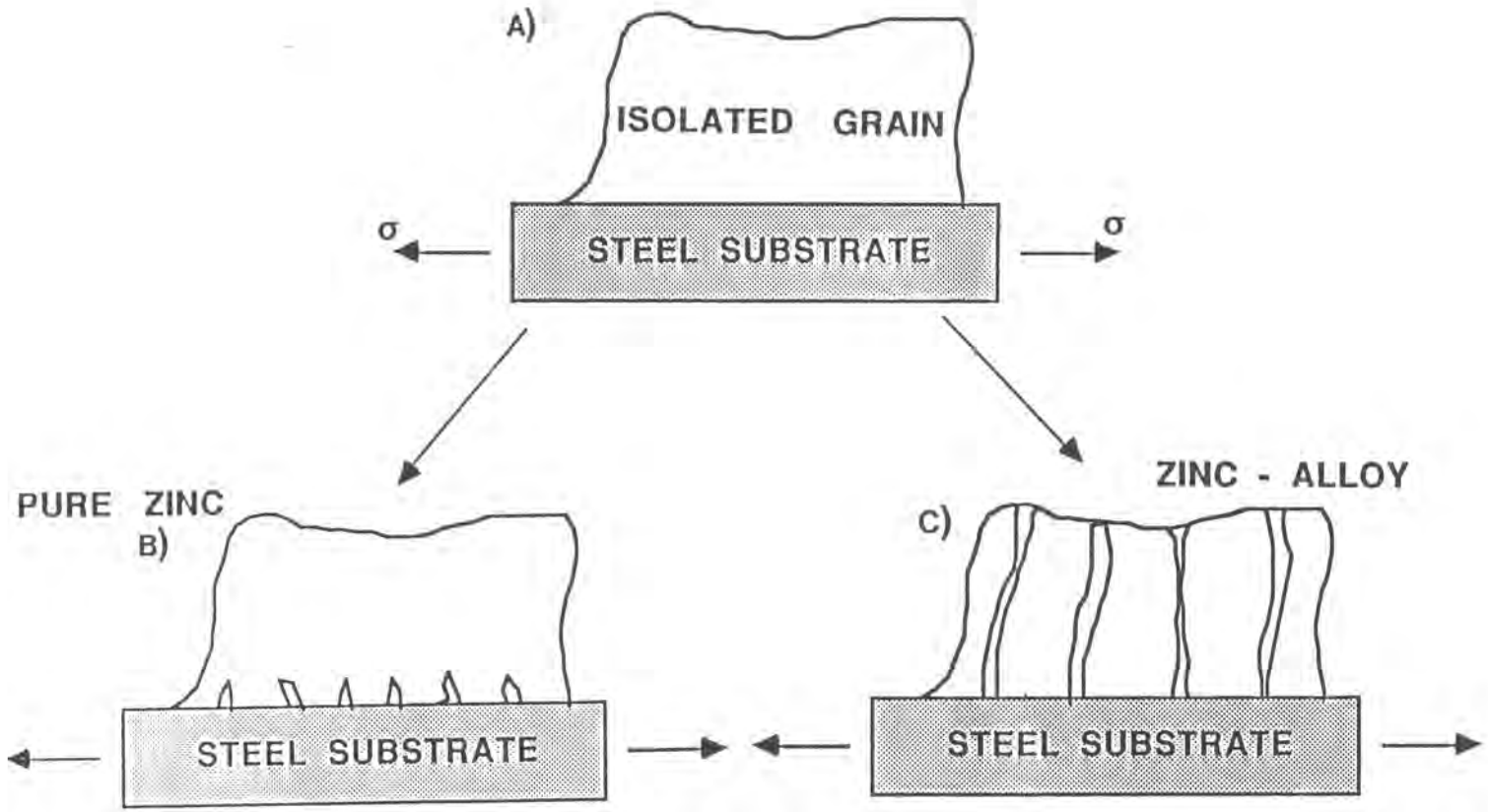

Figure 17 Fracture behavior of isolated grains of a zinc-based coating adhering to steel b) hot dip zinc grain c) hot dip zinc-alloy grain

Friction behavior of zinc-coated steel sheets are markedly different from that of uncoated steel. Friction coefficients vary for different coating materials. The schematic in Figure 15 shows a thin lubricating film between tool and coating surfaces. In this situation the normal pressure from the tool will aid in yielding but will not influence friction. However, when a breakdown of the lubricating layer leads to tool-metal contact, both normal pressure and material flow properties will directly influence the frictional behavior. Figure 18 shows schematically the tool in contact with pure zinc grains at the asperities in the coating. Due to high local stresses, zinc at these contact points will deform plastically, increasing the tool-coating contact areas. The increase in true areas of contact, increases the drawing load required to cause sliding. The increased drawing load causes an increase in the nominal shear stresses calculated over the apparent area of contact. If μ is defined as the ratio between the nominal shear stress and nominal pressure, μ will increase with pressure. This is schematically illustrated in Figure 19, where μ for the pure zinc coating is shown to increase with pressure. If the zinc crystals are replaced with brittle zinc-alloy crystals, the coating

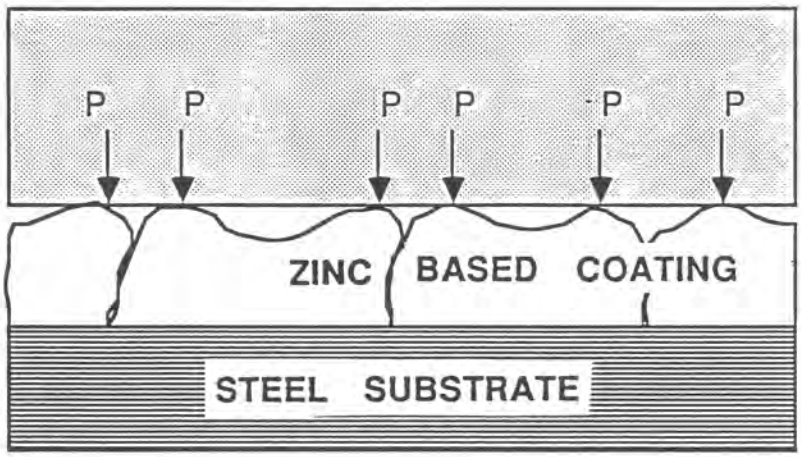

Figure 18 Tool surface in contact with the grains of a zinc-based coating. High local stresses will be generated at the points of contact (asperities on coating surface)

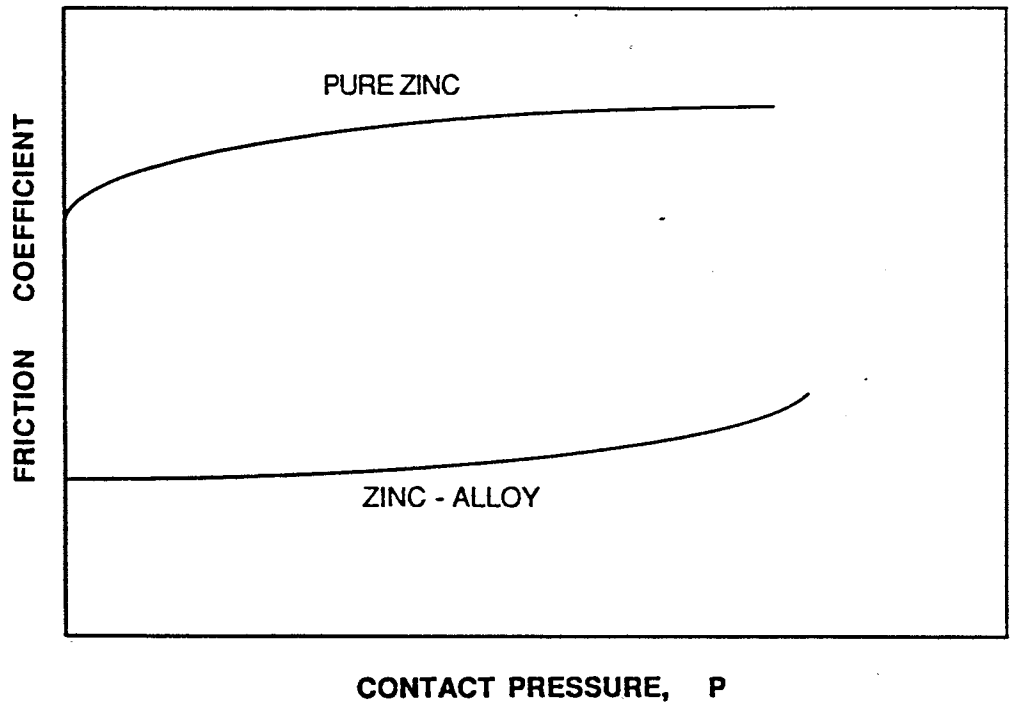

Figure 19 Changes in friction coefficients of pure zinc and zinc-alloy coatings with variations in contact pressure between the tool and the coating

will fracture at the tool contact points, leading to powdering. As a result the friction coefficients will be lower than the corresponding value for pure zinc due to a lack of significant increase in contact area and/or sticking conditions. In this respect, surface roughness measurements after the forming operation would be useful to determine the extent of metal-metal contact. Calculation of true contact areas will help evaluate the applicability of Wanheim and Bay model for metallic friction to coated sheet steels. This is an important aspect of the experimental design as it can provide an insight into friction mechanisms on coated sheet steels. Due to the flattening out of initial asperities or roughness peaks, it is predicted that surface roughness plays only a minor role in friction.

In order to evaluate the above mentioned concepts of coating deformation and friction a set of experiments were carried out as described in the next section. To test the effects of coating on the formability of coated sheet steels, two types of tests are required. The first type of test fundamentally evaluates the deformation behavior of coatings as a function of texture and microstructure. The second kind of test evaluates the frictional behavior of the coatings. A uniaxial tension test was used to evaluate the

deformation behavior of the coating. The mechanical testing program was supplemented by extensive X-ray diffraction (XRD) and scanning electron microscope (SEM) studies. A simple stress state such as uniaxial tension was chosen so that different material responses to stretching operations can be clearly elucidated. The understanding obtained from these tests can then be used to predict material responses under a more complex stress state.

Frictional behavior of the various coatings were evaluated in a bending under tension type of test (41). The bending under tension type of test is being extensively used to study the effects of coating properties such as texture and crystal structure, and the effects of imposed loading conditions such as contact pressures and sliding speeds, on the frictional behavior of several coated sheet steels (41). The bending under tension type of test has the advantage of being able to test selectively frictional properties on any given side of the coated sheet steel. The two sides of the coated sheet steel can be evaluated separately. The coating is subjected to a complex stress state when it is in contact with the roller in this test. Portions of the coated sheet steel not in contact with the roller are subjected to a simple stretching operation.

In the next chapter, the material selection, the mechanical and friction test conditions and the analytical techniques used in this program will be briefly discussed.

4.0 EXPERIMENTAL PROCEDURE

4.1 Materials Selection

Two different sets of materials were chosen for the fundamental deformation studies and the friction studies respectively. The first set of materials were chosen as part of a continuation of ongoing research on coating deformation. The second set of materials selected for friction analysis belonged to a small group of coated sheet steels that were chosen for extensive friction and formability studies. Both sets of materials were carefully chosen to include variations in texture and crystal structure. A third set of coated sheet steels, containing hot dip pure zinc coatings, were presented for analysis, during the course of the research program. These materials were not part of the experimental design and were acquired from an industrial source. Analysis of these materials presented an unique opportunity to apply the fundamental coating deformation model that is developed in this work, to solve an industrial problem. The characteristics of the various sets of materials will be described below.

Table 3 lists the characteristics of the coated sheet

TABLE 3 - Characterization of Coated Sheet Steels used in uniaxial tension tests

Coating Type	Coating Composition	Coating Thickness (μm)	Supplier
EG30 (Electrogalvanized)	Zinc	5.0	Bethlehem Steel
EG70 (Electrogalvanized)	Zinc	10.0	Bethlehem Steel
EG100 (Electrogalvanized)	Zinc	13.0	Bethlehem Steel
GA (hot dip)	55%Al,43.5%Zn 1.5%Si	17.0	Bethlehem Steel
GF (hot dip)	95%Zn, 5%Al, 0.2%Misch Metal	15.0	Inland Steel

steels chosen for the fundamental tensile deformation studies. The designations EG30, EG70 and EG100 refer to 30 gm/m^2, 70 gm/m^2 and 100 gm/m^2 electrogalvanized coatings, respectively. GA and GF refer to Galvalume and Galfan coatings. All sheets were coated on both sides. The electrogalvanized coatings of varying thickness were chosen to study effects of coating thickness on coating morphology and texture and subsequently their deformation behavior as a function of these factors. The Galvalume and Galfan alloy coatings were chosen to study the effects of coating phase composition and microstructure on coating deformation. Figure 20 shows the Al-Zn binary phase diagram, where the nominal compositions of the coatings analyzed in this work are indicated by vertical lines. As noted in Table 3, some of the coatings have minor additions of other components. Galvalume and Galfan coatings have widely different compositions and therefore can be expected to have completely different phases and microstructure. The effects of microstructural variations on the deformation behavior of these coatings were evaluated in the uniaxial tension tests.

An unique opportunity was provided to extend the understanding obtained from uniaxial tension studies, to an

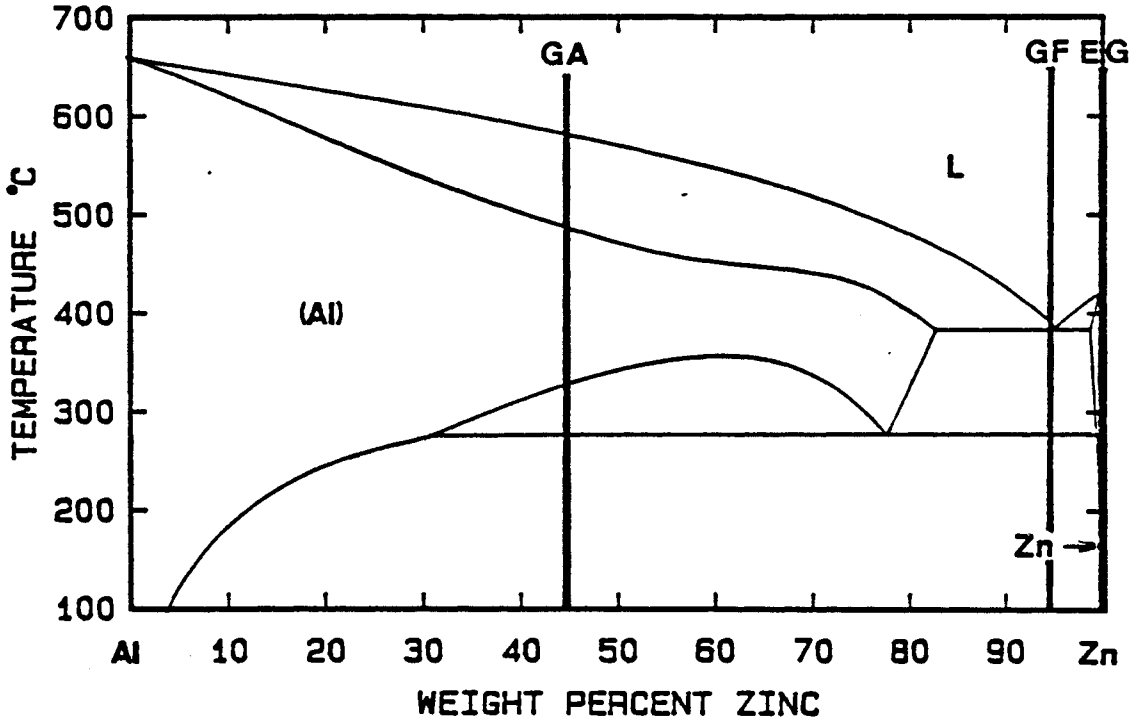

Figure 20 The Al-Zn equilibrium binary phase diagram (68). Nominal compositions of the coatings studied are shown by vertical lines. GA-Galvalume, GF-Galfan, EG-Electrogalvanized

investigation of the role of texture and crack formation during forming on subsequent atmospheric corrosion of hot dip galvanized parts. Specifically, an analysis of the corrosion behavior in galvanized parts revealed that (69), flexible tubes made in an industrial operation from certain batches of hot dip galvanized steel with relatively large spangle sizes corroded rapidly on localized areas of the parts. In contrast, parts formed from other coated steels with either coarse or fine spangles had acceptable corrosion-resistance. It was hypothesized that the corrosion responses of the different hot dip zinc coatings were due to texture effects, in addition to the effects of spangle size. To evaluate this hypothesis, three coated materials which were formed in a commercial forming operation were selected for analysis. The three hot dip zinc coatings, identified as X, Y and Z chosen for this study represented a distribution in spangle sizes and crystallographic textures, as summarized in Table 4. Coatings X and Y have relatively large spangle sizes, but different texture. Coatings Y and Z have similar texture, but different spangle sizes. Deformation behavior of the coatings were studied under SEM, in a biaxially stretched region on the formed flexible tube. The forming operation will be discussed in Section 4.2, while the results of this

TABLE 4 - Spangle size and texture of hot dip zinc coatings chosen for biaxial stretching

Coating Code	Rel. Spangle Size	Rel. Basal Tex.
X	Large	Moderate
Y	Large	Strong
Z	Small	Very Strong

study will be presented in Chapter 5.0.

The characteristics of the materials chosen for friction work are summarized in Table 5. The electrogalvanized and the hot-dip zinc coatings were chosen to evaluate the role of texture in friction. The galvannealed coating was chosen to evaluate the role of crystal structure in friction.

4.2 Mechanical and Friction Testing

All coated sheet steel samples used for the deformation study, were deformed in tension at a strain rate of 0.25/min, in a floor model Instron. Surface deformation and fracture observations by SEM were performed on microtension samples deformed in a previous study (11), as well as full scale tension samples. The microtension samples were smaller in size than a standard ASTM tension specimen (11). Full scale tension samples strained to various amounts, were subjected to both microscopic and X-ray diffraction analyses. As a result, coating deformation behavior and texture changes could be monitored as a function of strain. The method of quantification of texture, employed in this work, will be discussed in

Table 5 Characterization of coated sheet steels used in friction analysis

Material	Gage (inches)	Coating Type	Coating Texture	Coating Weight
Inland 70G70G	0.028	Electrogalvanized	Non-Basal,	70 gm/m^2
Stelco GOHD	0.032	Hot Dip Zinc	Basal planes parallel to surface	60 gm/m^2
Inland 60N40N	0.030	Hot-dip Zn-Fe Alloy Coating (Galvannealed coating)	Possible Texturing of δ-phase crystals	60 gm/m^2 on one side and 40 gm/m^2 on the other side

Section 5.1.2.

A schematic of the commercial roll forming operation that was used in the industry to manufacture flexible tubes is shown in Figure 21, along with the shape of the formed sheet as it exits the roll. As indicated in Figure 21, the formed sheet has two biaxially stretched zones on the top surface, and two more on the bottom surface. Deformation of the hot dip zinc coatings in these zones were monitored through SEM analysis.

Friction testing was done in a bending under tension type strip drawing test. A schematic of the test apparatus is presented in Figure 22 (41). As shown in the schematic, the forward pulling force is exerted by an MTS system. In this case, the lower ram of MTS 10 Kip load system supplies the pulling force. An independent manually operated hydraulic system supplies the back-tension force. The back-tension force is a result of forcing the hydraulic fluid through a controlled back-tension valve. The sheet is held by the two grips shown in Figure 22. The roller can be fixed or allowed to rotate freely. Other details on the test equipment are presented in References 41, 70 and 71.

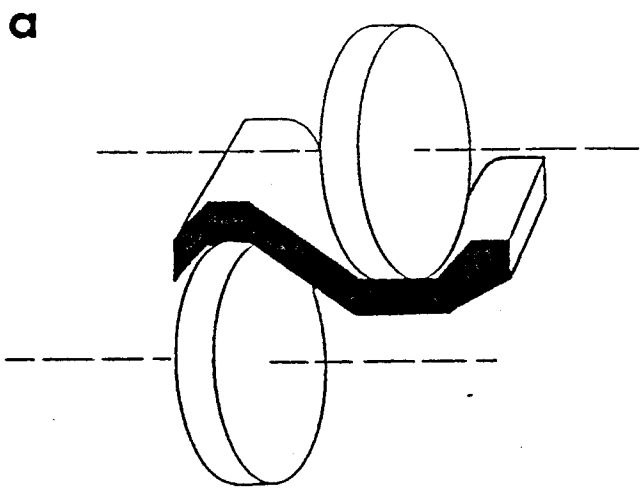

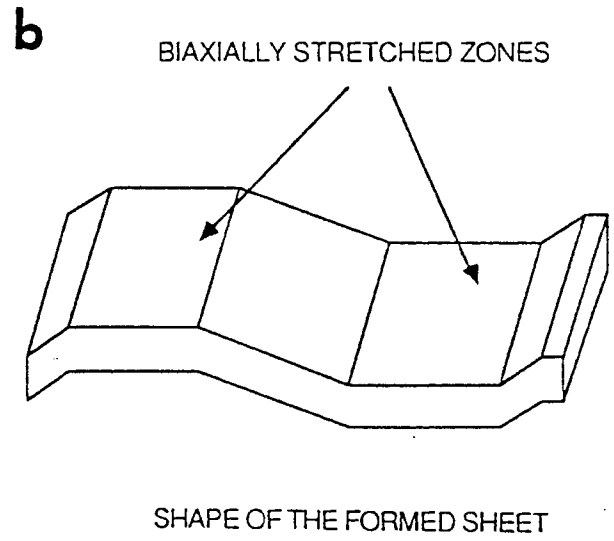

Figure 21 Schematic diagrams of a) the roll forming operation and b) the formed sheet with biaxially stretched zones indicated

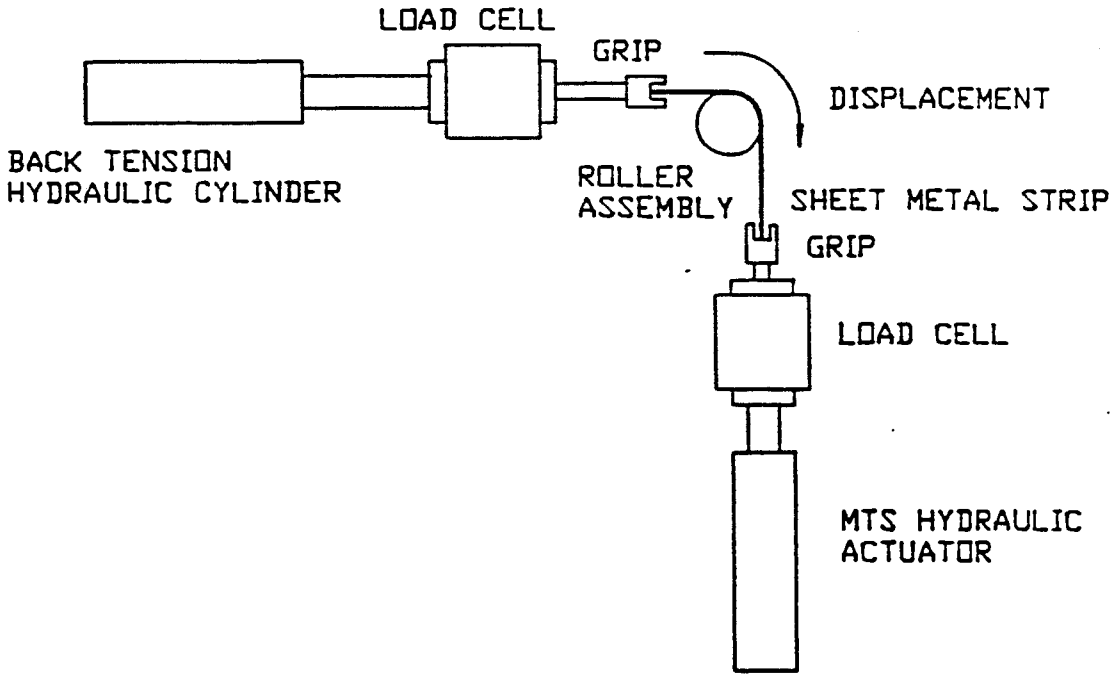

Figure 22 Schematic of the bending under tension type strip drawing test configuration (42)

The displacement rate used in all the friction tests was 100 inches/min. The coated sheet steels were tested at different back-tension levels (i.e., different contact pressures). At each back-tension level, three tests were run with a fixed roller configuration and one test was run with a free roller configuration. In each test, both the forward pulling force and the back-tension force in pounds were measured. From these measurements, values of the average contact pressure and the coefficient of friction can be calculated using the analysis presented in Section 2.4.3. At each back-tension value, three tests were run with a fixed roller, in order to obtain a better statistical estimate of the measured parameters in the test. Coating surfaces on the test samples that experienced contact with the roller, were examined under the SEM and in X-ray diffraction studies in order to monitor the deformation behavior and texture changes with contact pressure. An extensive SEM investigation was completed on all three coatings (in Table 5) in order to obtain an estimate of variations in true contact area as a function of the contact pressure.

4.3 Analytical Techniques

The two primary analytical instruments employed extensively in this work were the scanning electron microscope (SEM) and the X-ray diffractometer.

A Jeol JXA-840 scanning microanalyzer was used to study coating microstructures and deformation behavior in strained coated sheet steel samples. The microanalyzer was equipped with a Tracor-Northern energy dispersive X-ray spectroscopy (EDS) system, for performing semi-quantitative elemental analysis. Since the X-ray energy detector in the system had a beryllium window, lighter elements such as C and N could not be detected. However, the system was adequate to analyze the principle elements present in zinc and zinc-alloy coatings.

A Rigaku rotating anode X-ray diffractometer was used to study coating crystal structure and texture. Diffraction conditions were satisfied for the coating surface at all angles of incidence in a simple reflection technique. Therefore, only planes parallel to the coating surface contributed towards diffracted peak intensities. Filtered Cu-Kα radiation with a wavelength of 1.5405 Å was

used to obtain the diffraction patterns. Peak intensities were measured, where necessary, as integrated intensity by step scans through the peaks. The main peaks in the X-ray diffraction patterns were the Zn peaks. An analysis of the sampling depth indicated that for the Zn peaks of interest entire coating thicknesses were being sampled even in the thicker electrogalvanized coatings. Zn peaks monitored to follow texture changes were: Zn{0002} (primary slip plane, cleavage plane), Zn{10$\bar{1}$0}, Zn{10$\bar{1}$1}, Zn{10$\bar{1}$2} (twin plane), Zn{11$\bar{2}$2} and Zn{10$\bar{1}$3}. Other planes were not monitored either due to low peak intensities or lack of physical significance relative to flow and fracture in zinc.

5.0 RESULTS AND DISCUSSION

Table 6 summarizes the analyses performed on each of the selected coated sheet steels studied here. The important results from the analyses are presented in this chapter along with interpretive discussion. First the characterization of all the coatings in the as-received condition will be presented. This characterization includes both morphology and texture of the coatings. Next, results from uniaxial tensile deformation of the coatings listed in Table 3 will be presented. Following this the results from the analysis of deformation in hot dip zinc coatings subjected to the roll forming operation will be presented. Finally results from the friction tests will be presented. These include friction measurements in the bending under tension type strip drawing test as well as characterization of coatings subjected to this test.

5.1 Microstructure and Texture Characterization of As-Received Coatings.

5.1.1 Surface Morphology of As-Received Coatings

The surface morphologies on as-received coatings are

Table 6 Summary of Types of Analysis performed on each of the Selected Coated Sheet Steels in this investigation

Coating Type	As-received		Uniaxial Tensile Deformation		Friction Tests		Deformation in Roll forming operation	
	SEM	XRD	SEM	XRD	SEM	XRD	SEM	XRD
Electrogalvanized Zinc coatings								
EG 30	x	x	x	x				
EG 70	x	x	x	x				
EG 100	x	x	x	x				
Inland 70G70G	x	x			x	x		
Hot Dip Zinc Coatings								
X	x	x					x	
Y	x	x					x	
Z	x	x					x	
Stelco 60 HD	x	x			x	x		
Zinc-Alloy Coatings								
Galvalume (GA)	x	x	x	x				
Galfan (GF)	x	x	x	x				
Inland 60N40N	x	x			x	x		

SEM - Scanning Electron Microscopy
XRD - X-Ray Diffraction

shown in Figures 23-32. Figure 23 shows the surface morphologies of the as-received electrogalvanized steels used in uniaxial tension tests (68). Sets of parallel ledges are shown in relief on the surfaces. These ledges have been identified as edges of zinc basal planes (68) and have been related to hetero-epitaxial growth from the steel surface. Coating weight and thickness increase with the number of active electrogalvanizing cells. With the increase in the thickness of the zinc layer, preferentially oriented grains may grow at the expense of the less favorably oriented grains, resulting in a larger grain size at the surface. This may account for the difference in surface morphology shown in Figure 23, where the sets of parallel ledges are coarser in the heavier coatings. Other workers have found different morphologies varying from nodular to platelet appearance (72,73). These morphologies are related to plating conditions such as variation in the pH of electrolytes, addition of specific impurities to the plating bath, different types of electrodes, varying current densities, and constant versus fluctuating current, etc. (72).

Figure 24 shows cryogenically fractured cross sections (74) of the electrogalvanized coatings corresponding to

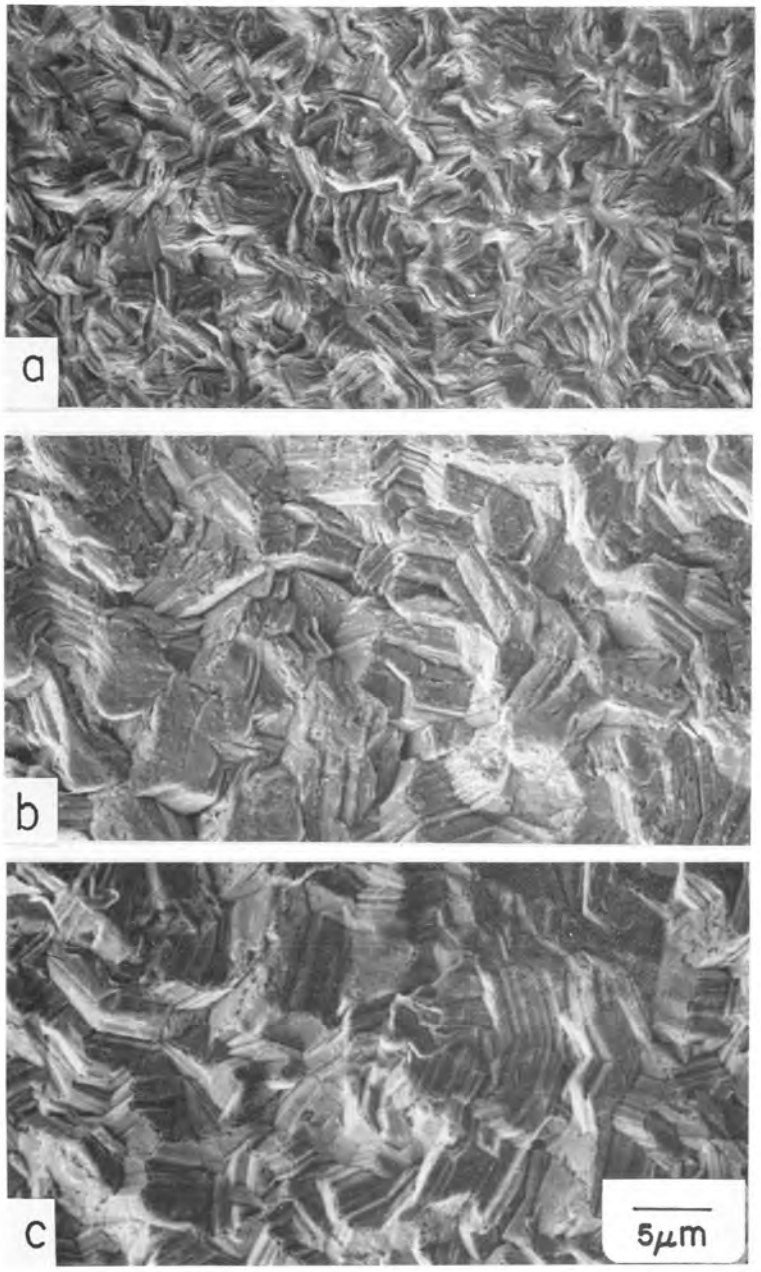

Figure 23 Surface morphologies of as-received electrogalvanized coatings (a) EG30 (b) EG70 (c) EG100

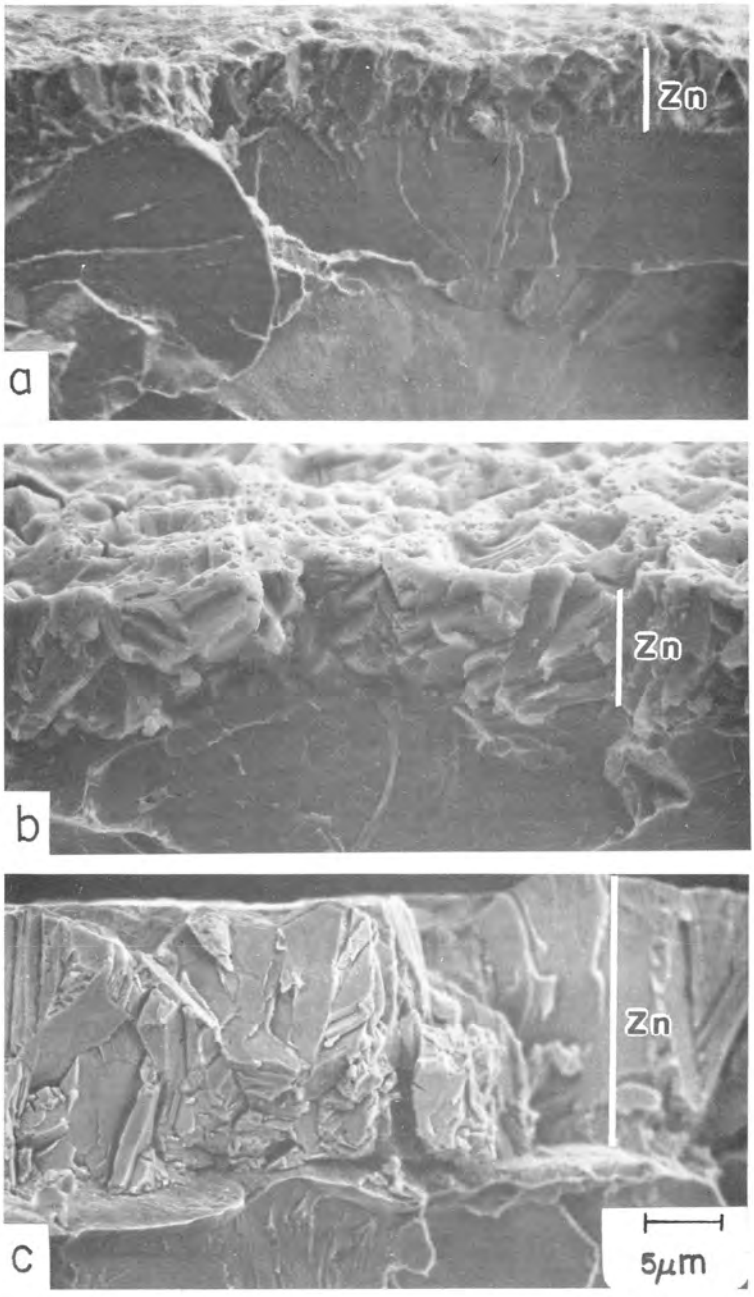

Figure 24 Cleavage fracture through electrogalvanized coatings (a) EG30 (b) EG70 (c) EG100

Figure 23. The cleavage planes in steel are the {100} planes, while zinc cleaves along the basal plane, Zn(0001). The cross section of the EG100 coating (Figure 23C) shows some amount of grain coarsening in the regions closer to the surface of the coating (in a 10 μm region from the surface). This again demonstrates preferential growth of favorably oriented zinc crystals. Preferential growth of certain grains affect the grain size, surface roughness, and surface texture.

Figure 25 shows the α-Al dendrites on the as-received surface of a Galvalume coating. In Galvalume coatings, a diffusion layer is formed between the steel and the bath, called the "alloy layer", which consists of Fe-Al and Fe-Al-Si compounds (21). The overlay above the alloy layer consists of the α-Al dendrites, Zn-rich interdendritic regions, and Si particles which form as a result of supersaturation of the Al-Zn bath with Si upon cooling.

Figure 25 also shows interdendritic regions which are Zn-rich between the α-Al dendrites. The nominal compositions of these regions were confirmed by semiquantitative EDS (X-Ray energy dispersive spectroscopy). Other investigators (21) show that the

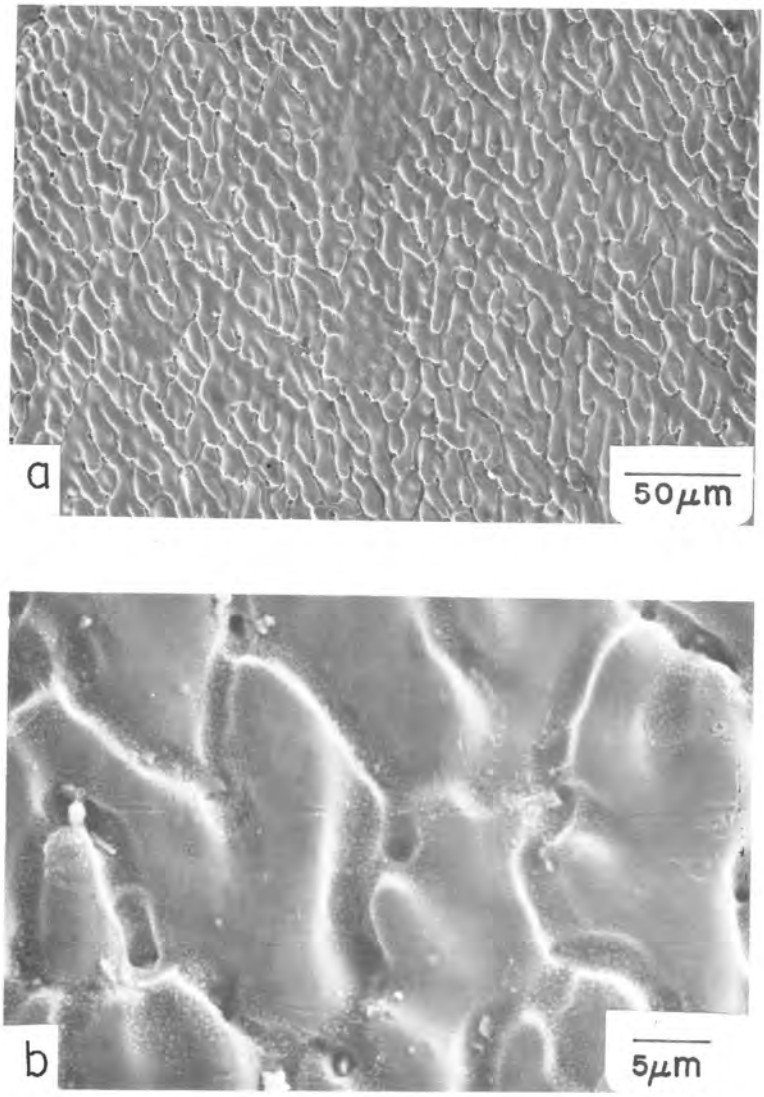

Figure 25 Unetched surface of As-Received Galvalume coating showing the α-Al dendrites and the interdendritic regions which are Zn-rich

composition of the α-Al dendrites compares well with what is expected from the Al-Zn binary phase diagram (Figure 20). The particles in the interdendritic regions in Figure 25b were analyzed and found to be Al rich (approximately 65-70 % Al, 25-30 at % Zn with traces of Fe and Si).

Figure 26, a SEM micrograph, shows a two-phase eutectic structure on the surface of a Galfan coating. Galfan has a near eutectic composition in the Al-Zn binary system, as shown in Figure 20. The microstructure of Galfan consists of rod eutectic structure of zinc-rich and aluminium-rich phases, as seen in Figure 20. The fineness of the structure increases with the cooling rate and the microstructure is completely eutectic when cooled at high rates (20). If the cooling rate is slow, primary zinc or aluminium-rich phases are also formed (20). Figure 26 also shows clear boundaries between the eutectic colonies. The matrix within each colony is the Zn-rich phase, while the dark spots are the Al-rich phase.

Figure 27 shows a macrophotograph of the spangles on the surface of hot-dip pure zinc coatings, that were chosen for the biaxial stretching operation. The difference in spangle size between the large and the small spangled

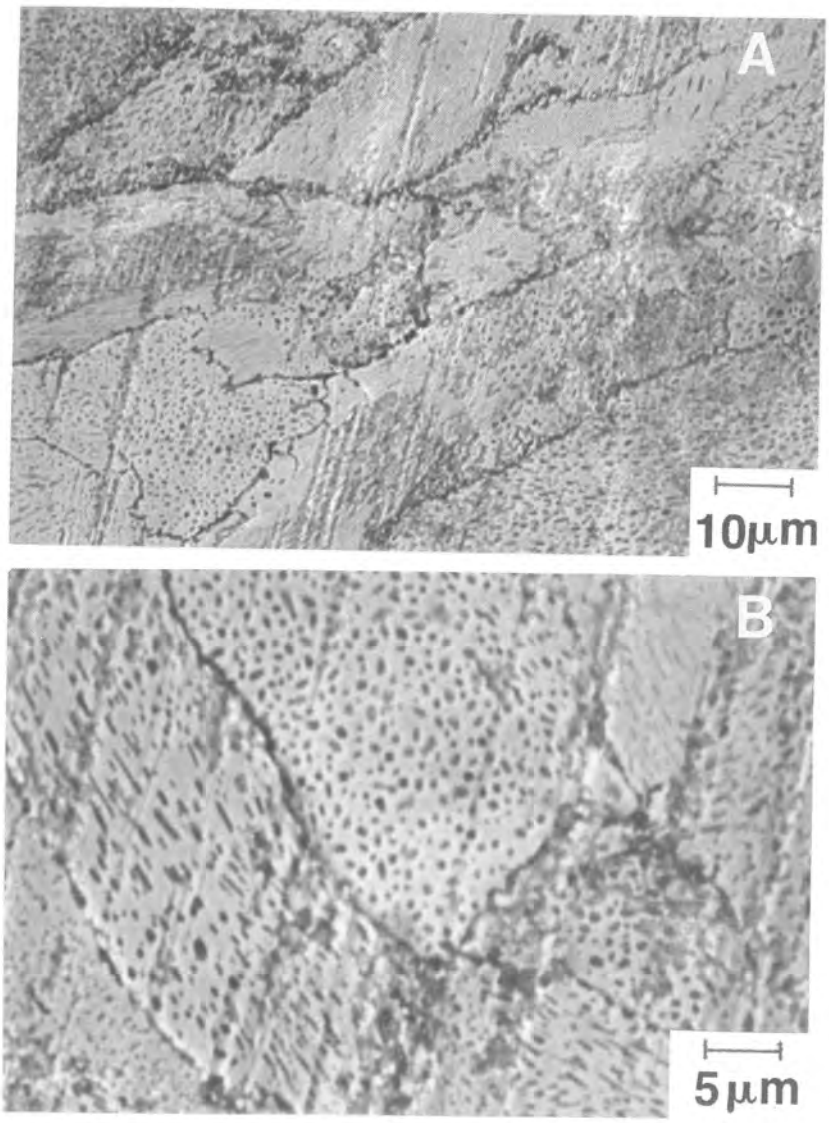

Figure 26 Surface morphology on as-received Galfan coating showing the two phase eutectic structure. The dark spots are the Al-rich phase in a Zn-rich matrix. Spangle boundaries are clearly seen on the coating surface

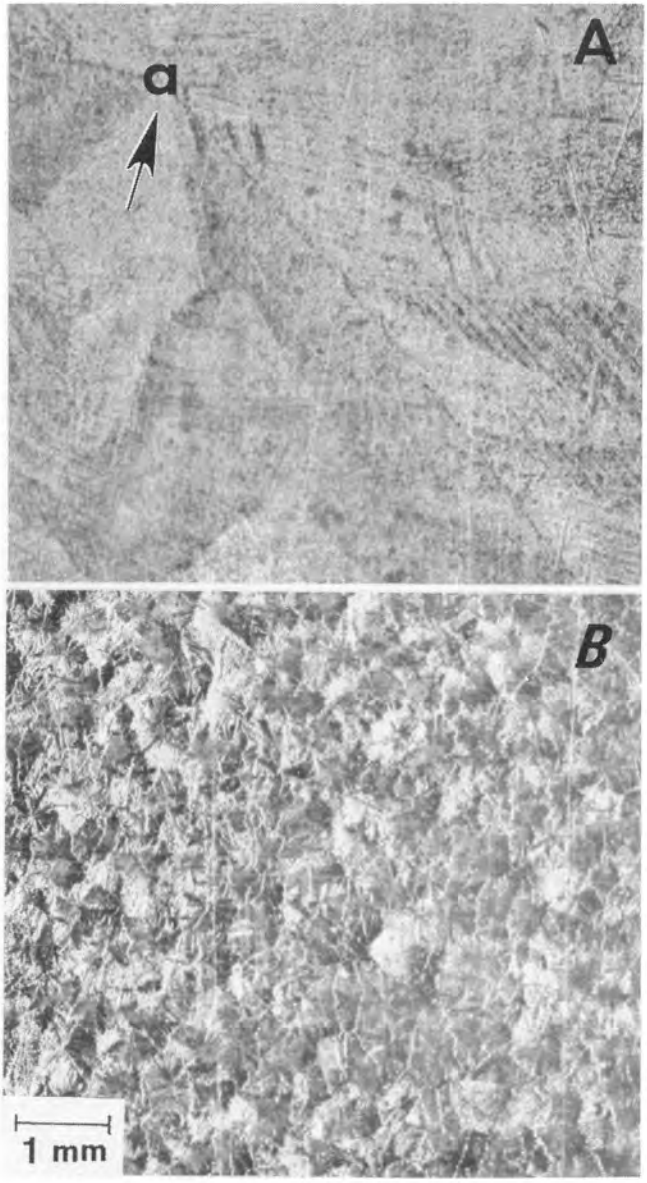

Figure 27 Surface spangles in hot dip zinc coatings a) coarse spangles specimen X, b) fine spangles specimen Z (Light macrographs)

coatings, is greater than an order of magnitude. A spangle on galvanized iron consists of many grains growing from several nuclei which are related to each other in crystallographic orientation (17,18). Thus, each spangle is subdivided into spangle sectors, and each sector of the spangle represents an individual crystal. The spangle sectors are approximately triangular in shape and the spangle itself has a star-like appearance. This arrangement is shown in Figure 27A, where a star-like pattern originates at point a. The size of spangles can be controlled by proper additions of lead, tin and cadmium to molten zinc bath (10). For example a low Pb content in the bath promotes small spangle sizes or a spangle-free appearance.

Figure 28 presents the surface morphology on an Inland 70G/70G electrogalvanized coating. Once again, parallel sets of ledges associated with edges of sets of zinc basal planes can be seen in relief. This coating has a different texture compared to the electrogalvanized coatings that were analyzed in uniaxial tension tests.

Figure 29, presents SEM micrographs of the surface on the Stelco60HD hot dip pure zinc coating that was subjected

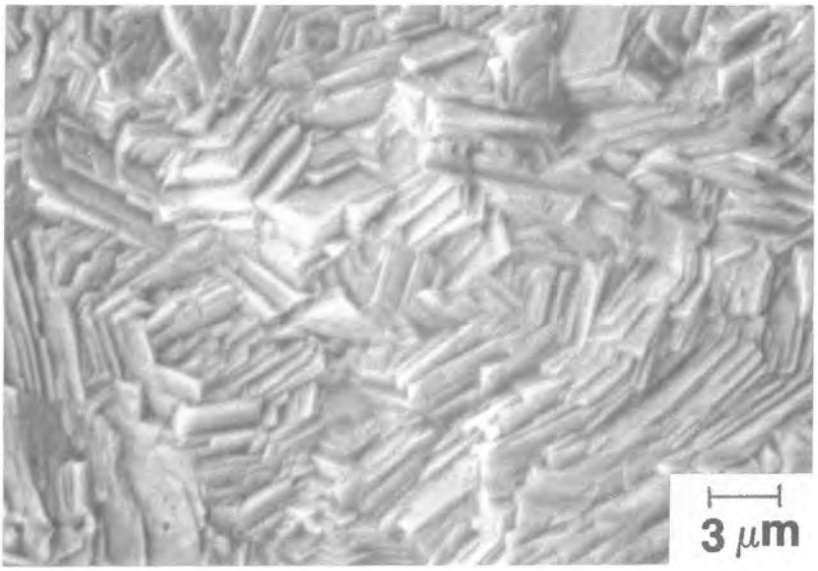

Figure 28 Surface morphology on as-received electrogalvanized zinc coating (Inland 70G70G). Parallel ledges in relief represent edges of sets of basal planes in zinc crystals

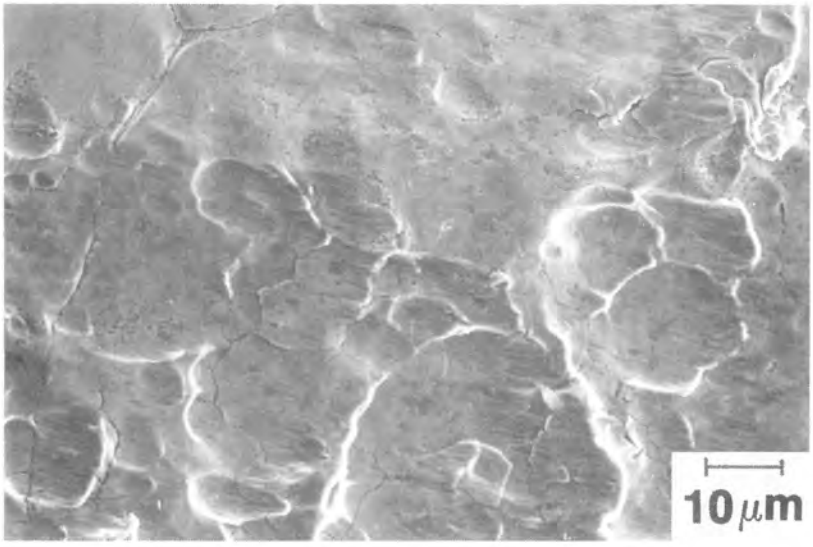

Figure 29 Surface morphology on as-received hot dip zinc coating (Stelco 60HD). Gouge marks and a network of microcracks are seen on the coating surface

to the friction test. As will be shown later, this zinc coating had a strong basal plane texture. The key features on this micrograph are the presence of a network of possible microcracks, and gouge marks. It was difficult to discern spangle sectors or spangle boundaries in the SEM. The line running across the left hand side of the micrograph in Figure 29 could be a spangle boundary. The microcracks and the gouge marks could be the result of a minor rolling operation.

Figure 30 presents features on the surface of an Inland 60N40N galvannealed coating. Evidence for two types of alloy crystal morphology is seen. The crystal morphology shown in Figure 30b is on the surface of the coating. It consists of polygonal particles of different sizes distributed randomly. Within the holes in the coating in Figure 30a, a different crystal morphology is seen. This is expanded in Figure 30c, and is probably characteristic of a subsurface alloy layer. The alloy particles are elongated along one direction and have a rod like geometry. In Figure 30a, flattened regions of the coating are visible. They are probably a result of a temper rolling operation. EDS analysis on the flattened region gave a composition of 92 wt% Zn and 8 wt% Fe, while

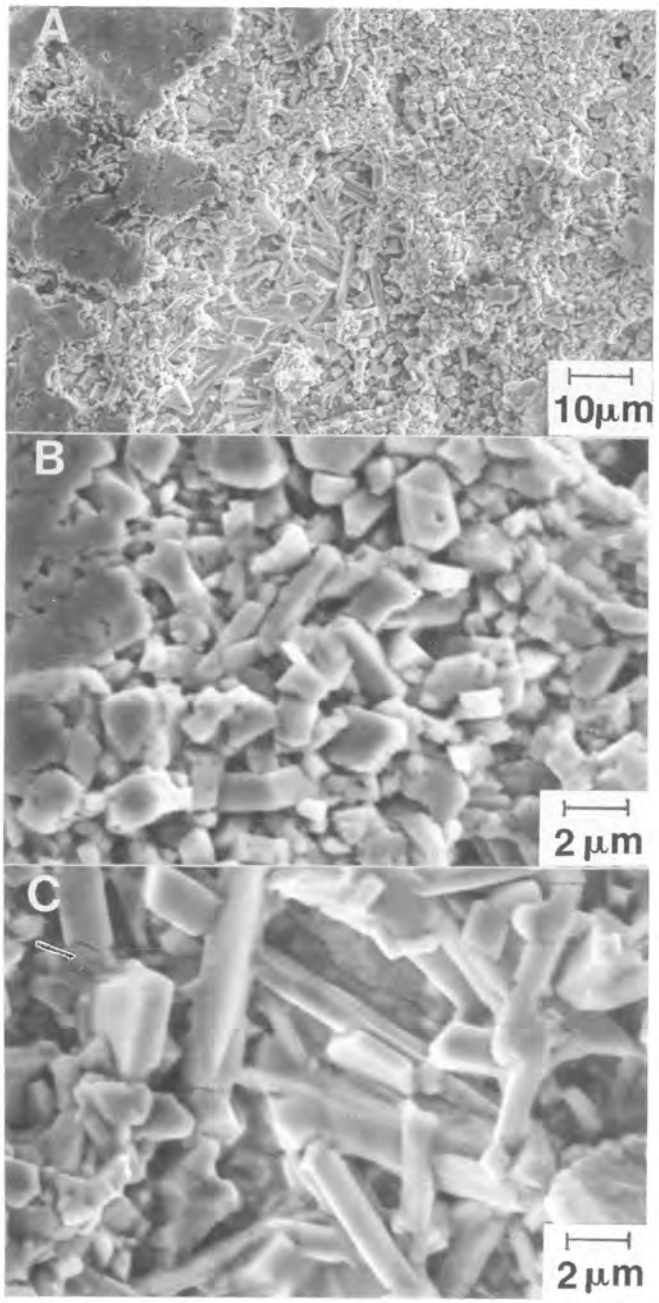

Figure 30 Surface morphology on as-received galvannealed coating (Inland 60N40N). a) powdering or flaking is indicated by the holes in the coating, b) morphology of alloy crystals on surface, c) morphology of alloy crystals in a subsurface layer

analysis in the holes in Figure 30a gave 84 wt% Zn and 16 wt% Fe. Therefore, the two different morphologies reflect varying compositions leading possibly to different intermetallic phases.

5.1.2 Texture on As-Received Coatings

The orientation of the crystals in a coating, were determined by X-Ray diffraction. X-Ray diffraction was carried out on all as-received coatings. Texture was quantified in terms of normalized peak intensities, where necessary. For the electrogalvanized coatings, all the zinc peaks were normalized to the Zn{10$\bar{1}$1} peak, i.e., the individual peak intensities were divided by the intensity of the Zn{10$\bar{1}$1} peak in a given diffraction pattern, and the ratio multiplied by 100. Zn{10$\bar{1}$1} peak is the most prominent peak in a zinc powder diffraction pattern. Table 7 lists the normalized intensities of the Zn peak obtained from the electrogalvanized coatings investigated in the uniaxial tension tests, along with those obtained for a powder sample (76). In order to quantify texture, "deviation parameters", of Zn peaks were calculated for each of the coatings in both the as-received and strained condition (68). The deviation parameter of a Zn{hkil} peak

Table 7 Relative intensities of Zn peaks obtained from Zn powder and as-received electrogalvanized coatings

Peaks	Zn Powder (I_r)	EG30 (I_c)	EG70 (I_c)	EG100 (I_c)
Zn{0002}	54%	10%	19%	26%
Zn{10$\bar{1}$0}	40%	17%	16%	16%
Zn{10$\bar{1}$1}	100%	100%	100%	100%
Zn{10$\bar{1}$2}	28%	17%	18%	30%
Zn{11$\bar{2}$2}	23%	31%	76%	82%

I_r - normalized intensities of peaks for random orientation of crystals.

I_c - normalized intensities of peaks obtained on the coating surfaces.

is defined as:

$$\Delta\{hkil\} = [(I_c - I_r)/I_r]*100 \qquad [13]$$

where $\Delta\{hkil\}$ is the deviation parameter, in percentage, for Zn{hkil} peak, I_c is the normalized intensity of the Zn{hkil} peak obtained on the coating, and I_r is the normalized intensity of the Zn{hkil} peak obtained on a powder sample (random crystal orientation). A value of zero for all $\Delta\{hkil\}$ corresponds to a random pattern. Values different from zero qualitatively indicate texture differences.

The X-Ray diffraction patterns which are direct traces of the experimental intensity versus 2θ data obtained on as-received EG30, EG70 and EG100 samples are shown in Figures 31-33. Comparing the X-Ray patterns in these figures with the pattern for a random sample, shown in Figure 34, clear deviations from randomness in orientation are seen. With the use of the procedure discussed above, deviation parameter of individual Zn peaks were calculated for the three electrogalvanized coatings with varying coating weights. The deviation parameters of Zn{11$\bar{2}$2} peak which is the most dominant peak in these coatings and the

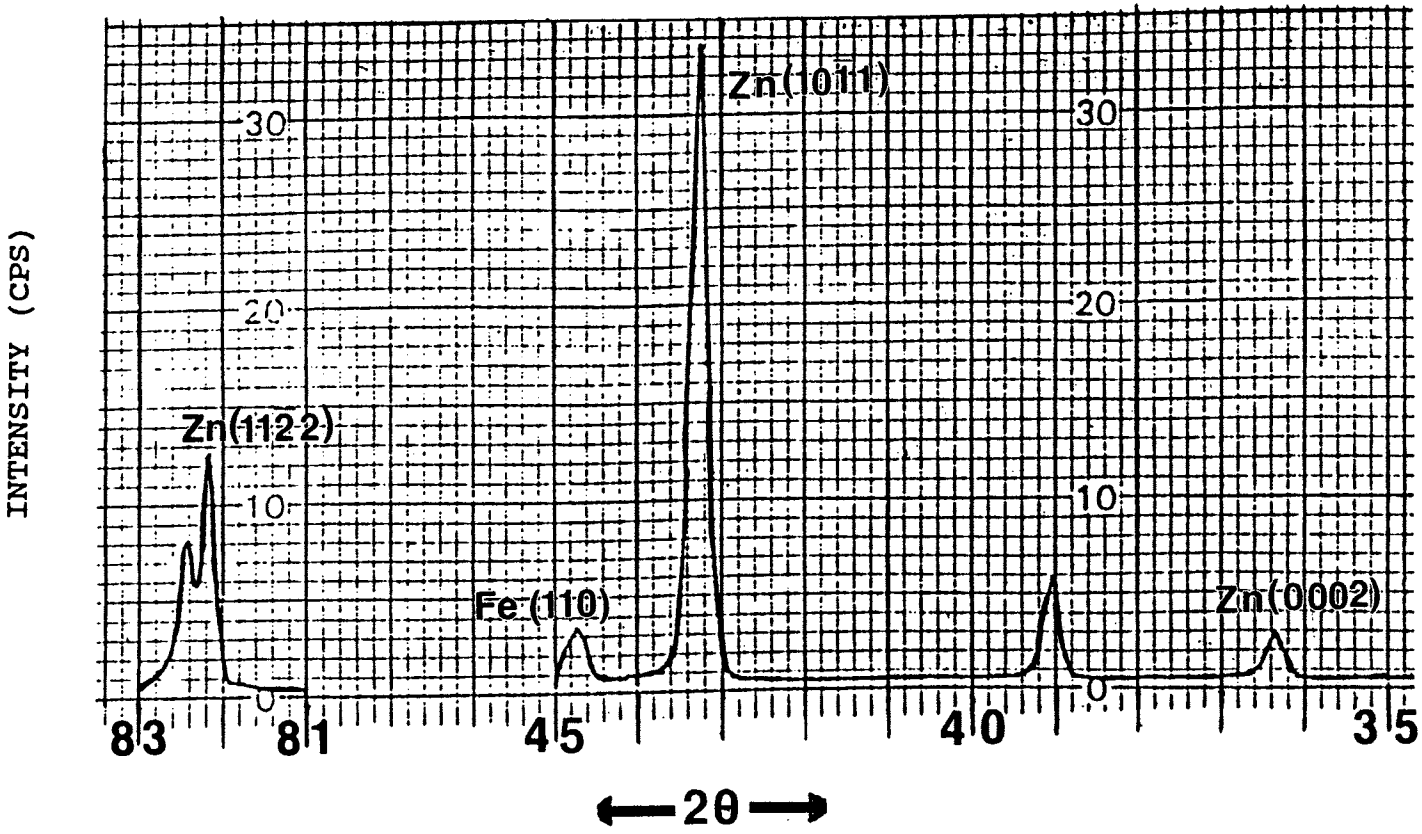

Figure 31 X-ray diffraction pattern obtained from an as-received EG30 electrogalvanized zinc coating

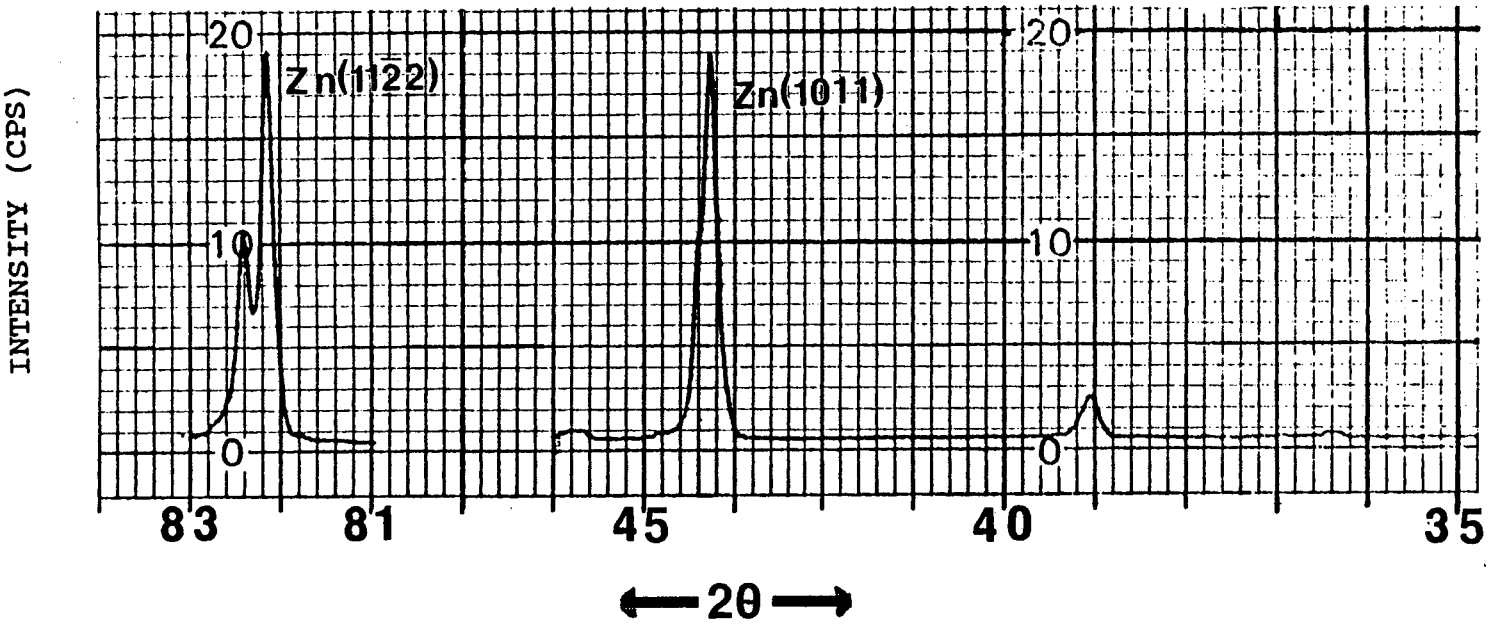

Figure 32 X-ray diffraction pattern obtained from an as-received EG70 electrogalvanized zinc coating

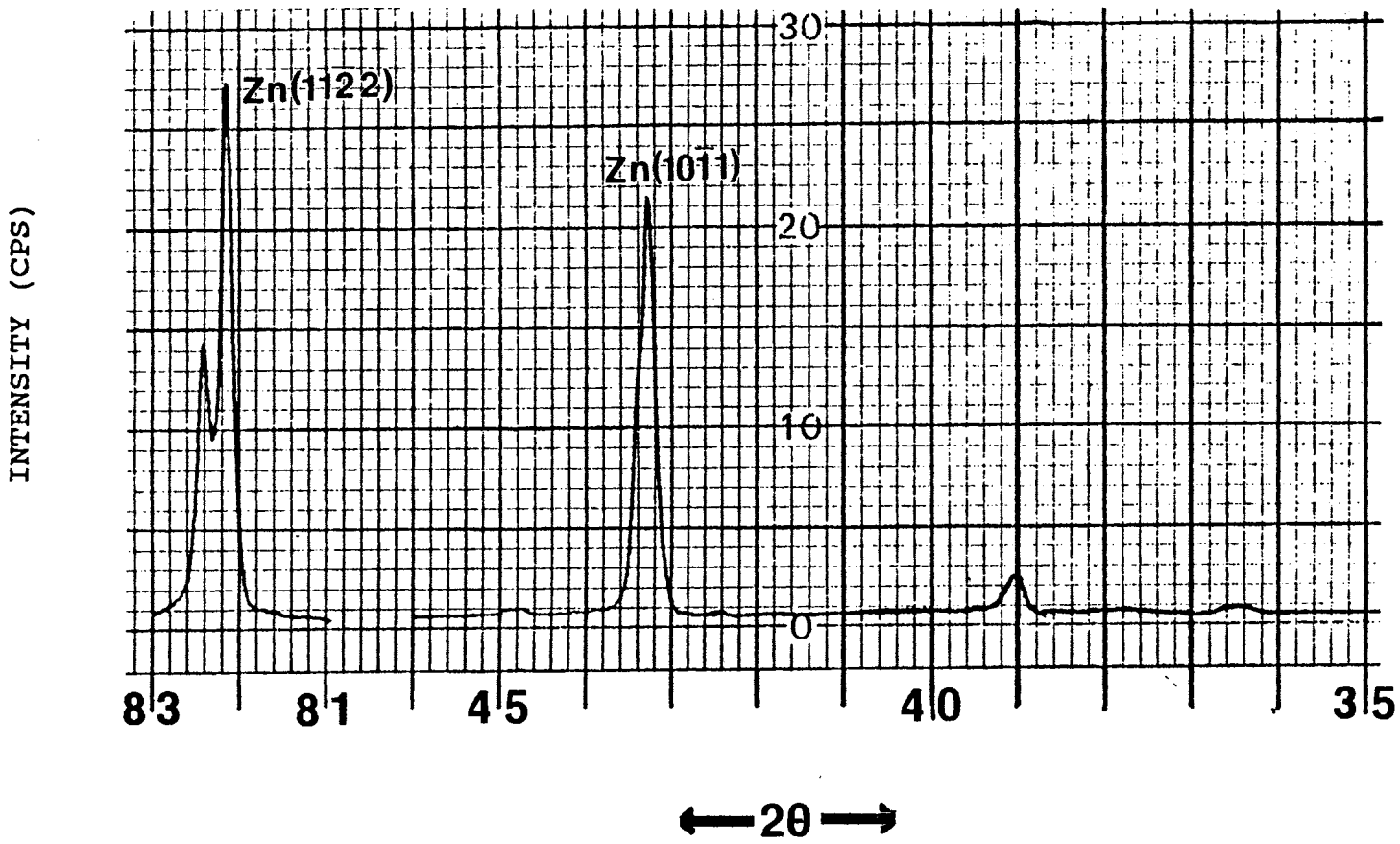

Figure 33 X-ray diffraction pattern obtained from an as-received EG100 electrogalvanized zinc coating

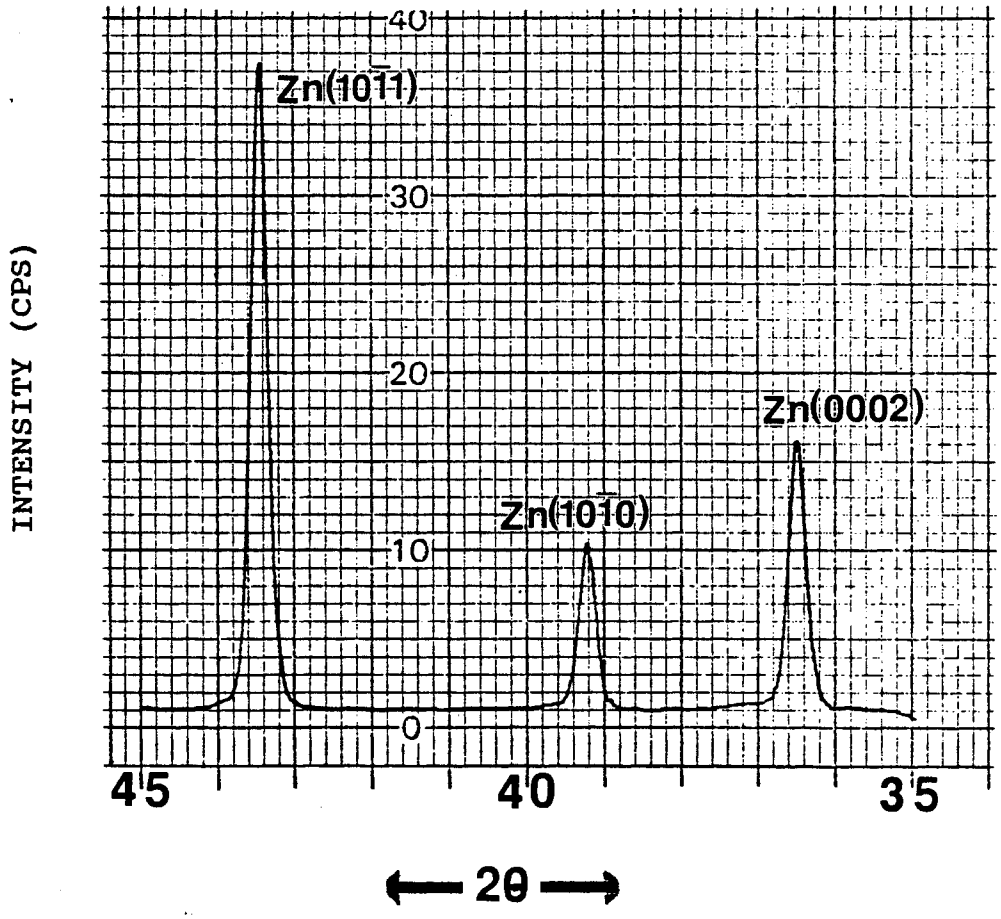

Figure 34 X-ray diffraction pattern obtained from zinc powder sample

Zn{0002} (basal plane) peaks are plotted as a function of coating weight in Figure 35. Zn $\{11\bar{2}2\}$ was the only peak that showed a positive deviation from randomness even in the thinnest of the electrogalvanized coatings (EG30). Figure 35 also shows that the basal plane peak exhibits a negative deviation from randomness in all three coatings. As the coating weight is increased, from 30gm/m^2 (EG30), to 100gm/m^2 (EG100), $\Delta\{11\bar{2}2\}$ increases significantly and reaches a value of +250% in the EG100 coating. This indicates a definite development of texture with coating weight and is consistent with the preferential growth of certain favorably oriented grains as noted earlier (Figs. 23 and 24). The texture analysis shows that grains with Zn$\{11\bar{2}2\}$ planes parallel to the surface are the preferred grains. $\Delta\{0002\}$ shows relatively little change with coating weight. In contrast, Lindborg (77), using a similar system of measuring texture, has found the Zn$\{11\bar{2}0\}$ prism planes to align parallel to the surface in zinc crystals electroplated from a cyanide bath. He found that Zn$\{11\bar{2}0\}$ texture increased with the thickness of the electroplate and suggested that a {100} texture in cold rolled steel favored a Zn$\{11\bar{2}0\}$ texture in the coating. Kamei and Ohmori (72) have suggested that the {0001} plane in the zinc crystals align with the {110} planes in the

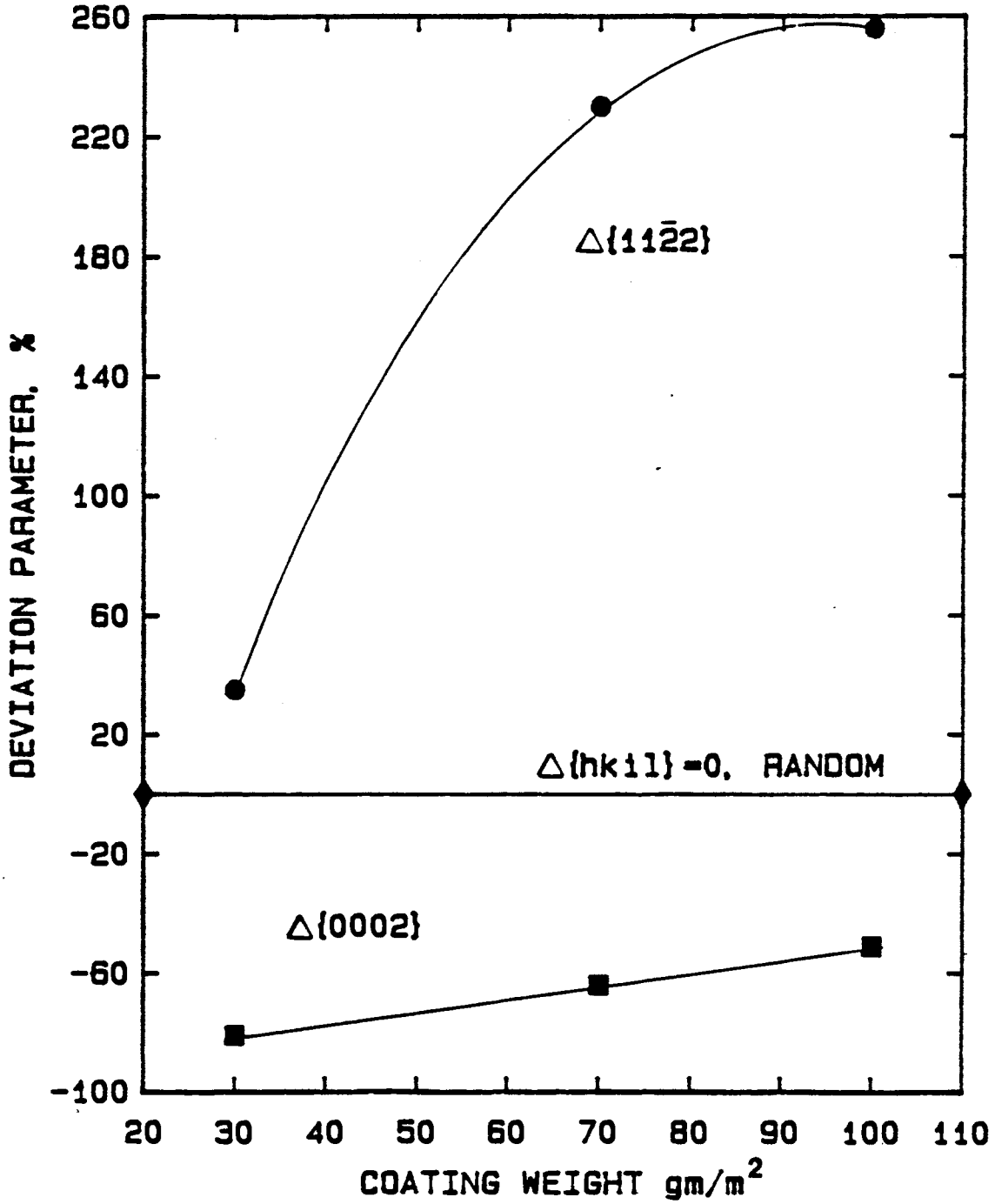

Figure 35 Deviation parameters of Zn(11$\bar{2}$2) and Zn(0002) vs the coating weight in electrogalvanized coatings listed in Table 3

steel substrate. The reason for the influence of steel texture is the fact that in the absence of intermetallic layers, the zinc atoms interact directly with the Fe atoms, resulting in a matching of specific planes in Zn with specific planes in Fe.

In this study, the positive deviation of Zn{11$\bar{2}$2} planes in the EG30 coating indicates a possible preference for nucleation of grains with these planes parallel to the surface. The significant increase in Zn{11$\bar{2}$2} peak intensity with thickness indicates preferential growth. Thus preferred nucleation and growth appear to influence the texture of the electrogalvanized coatings studied here.

X-ray diffraction from a Galvalume surface produced peaks from the Al-rich phase in addition to the primary zinc peaks. The zinc peaks did not show any significant preferred orientation. The peaks from the Al-rich phase were at $2\theta = 36.8^{o}$, $2\theta = 38.6^{o}$ and $2\theta = 44.8^{o}$. The prominent Al peaks showed significant anisotropy in intensities, with rotation about the normal to the sheet surface being analyzed. Figure 36 shows the Zn and Al peaks for an initial zero position and for 180^{o} rotation from that position about the normal to the diffracting

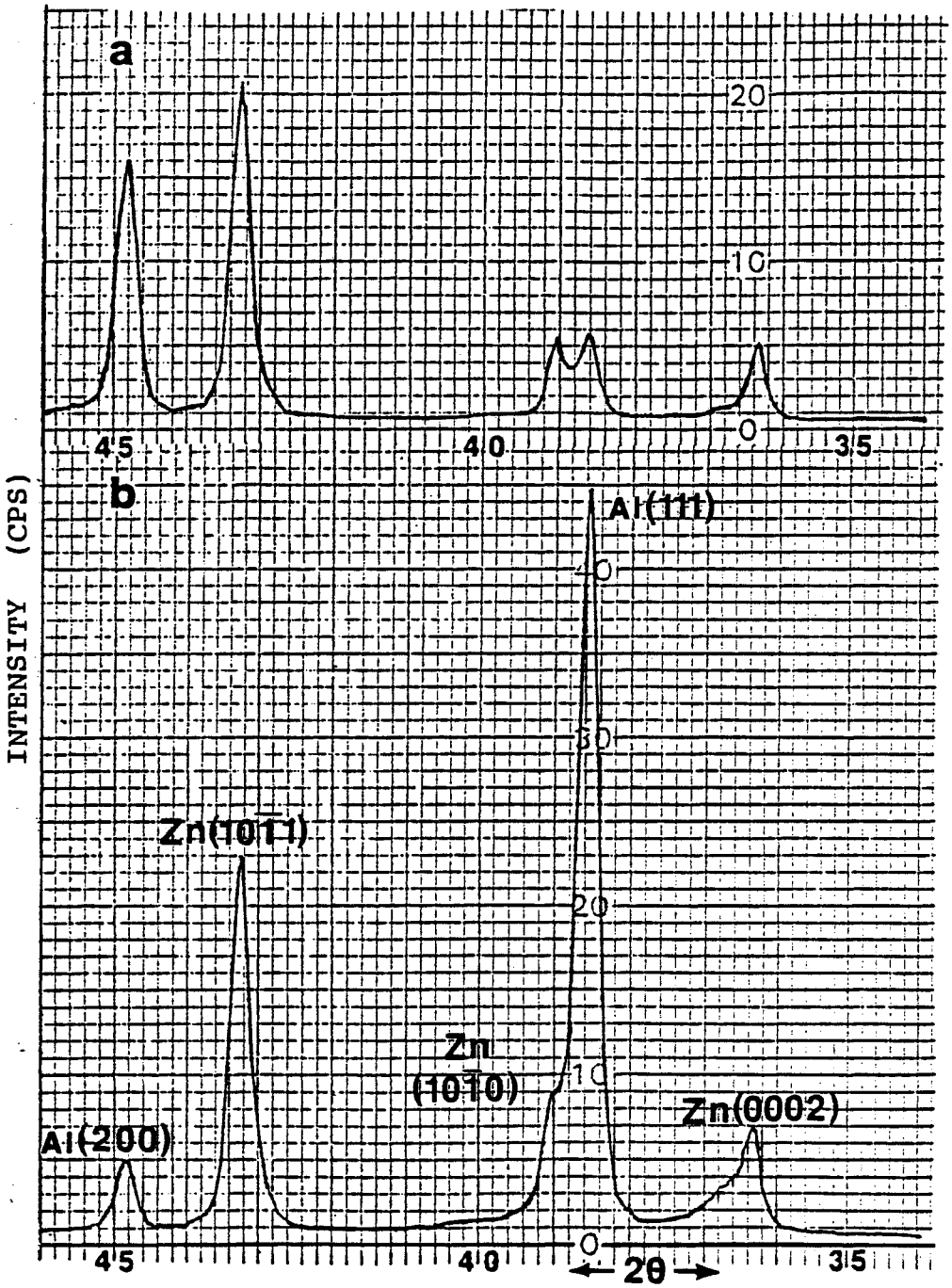

Figure 36 A section of the X-ray diffraction pattern obtained on an as-received Galvalume coating surface showing the Al and Zn peaks. (a) zero position (b) 180° rotation with respect to (a) about the normal to the diffracting surface .

surface. The Al (111) peak is significantly more prominent for the 180^{o} orientation. An explanation for the anisotropy could be given in terms of the effect of spangles on an X-ray diffraction pattern. Samples used for X-ray analysis are often smaller than the size provided for, in the sample holder (approximately 1.5 x 2 cm^2). The size of the X-ray beam is even smaller, and radiates only a portion of the sample surface. If the sample is not centered in the holder, rotation causes different areas on the sample to be exposed to the X-ray beam and thus the effects shown in Figure 36 reflect a sampling area effect. Since Galvalume coating has a pronounced spangle structure, plots a and b in Figure 36 represent patterns from different spangle sectors contributing to diffraction at different locations on the sample. Since spangle sectors have different crystallographic orientations, the diffraction pattern shows variations in peak intensity ratios with X-ray beam position on the sample. Significant variations in Al peaks suggest very specific orientations of Al dendrites within each spangle sector. Also, an intense Al(111) peak in Figure 36b, indicates that many spangle sectors have Al dendrites oriented in such a way that the Al(111) planes are almost parallel to the coating surface. Note that the Zn peaks do not change their

relative intensities between the two plots. This is because the pattern of Zn peaks obtained on Galvalume, shown in Figure 36, is closer to what is obtained from a Zn powder sample, shown in Figure 34. The Zn-rich interdendritic regions have no preferred orientation, parallel to the surface, and rotation or translation of sample has no effect on the Zn peak ratios.

As a result of this anisotropy in some of the prominent peaks in the Galvalume X-ray diffraction pattern, texture changes were not calculated as a function of strain even though strained sample surfaces were analyzed by X-ray diffraction.

The X-ray diffraction pattern recorded on Galfan coatings is plotted in Figure 37. It shows a strong Zn(0002) peak, which suggests that Galfan has a strong basal plane texture. Unlike Galvalume, Galfan has no pronounced spangle structure and only a small amount of the Al-rich phase. The prominent Zn(0002) peak obtained on Galfan showed very little change with translation or rotation of the sample. Deviation parameters of Zn peaks, for Galfan calculated from peak intensities normalized to the Zn(0002) peak, will be presented later in a table along

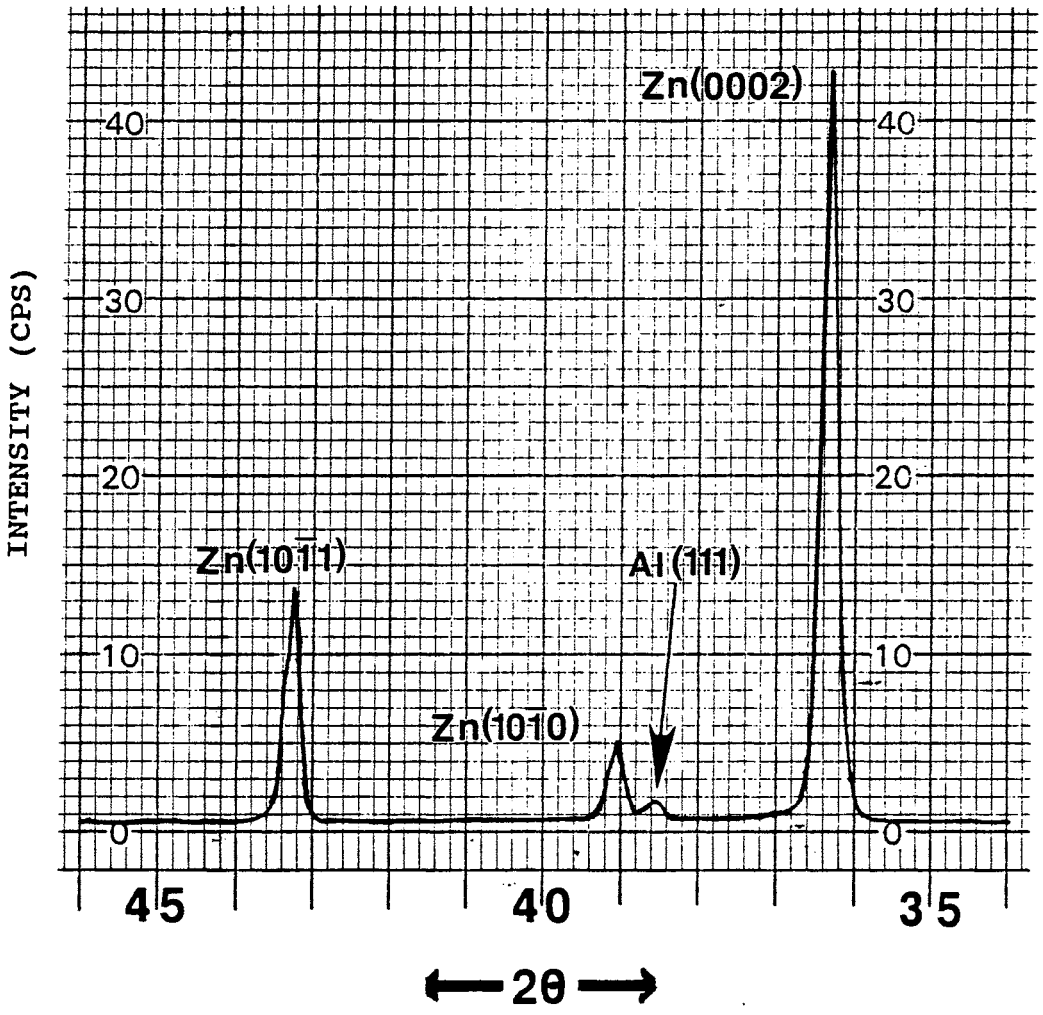

Figure 37 X-ray diffraction pattern obtained from an as-received Galfan coating

with results from uniaxial deformation.

The X-ray diffraction patterns obtained for the three hot-dip zinc coatings X, Y and Z are given in Figures 38-40. In these figures, traces obtained at two different locations on each sample are presented. For each material, the pairs represent the maximum observed differences in the recorded diffraction patterns. For the large spangled materials X and Y, the diffraction pattern varies significantly with location. In these materials, a relatively small number of spangles contribute to the diffracted intensity in each pattern. Thus the diffraction pattern depends on the distribution of crystallographic orientations in spangle sectors being analyzed. In a fine spangled material (e.g. coating Z) a higher number of spangles contribute towards diffraction. As a result, variations in peak intensities with specimen translation are minimal. This is seen in Figure 40, which shows identical peak intensity ratios at different locations on the fine spangled material, Z. Now, consider the Zn{0002} peak at a 2θ value of 36.3°, in Figures 38-40. Specimen Z (Figure 40) shows a strong and uniform basal plane texture, specimen Y (Figure 39) shows a strong but non-uniform basal plane texture and specimen X (Figure 38)

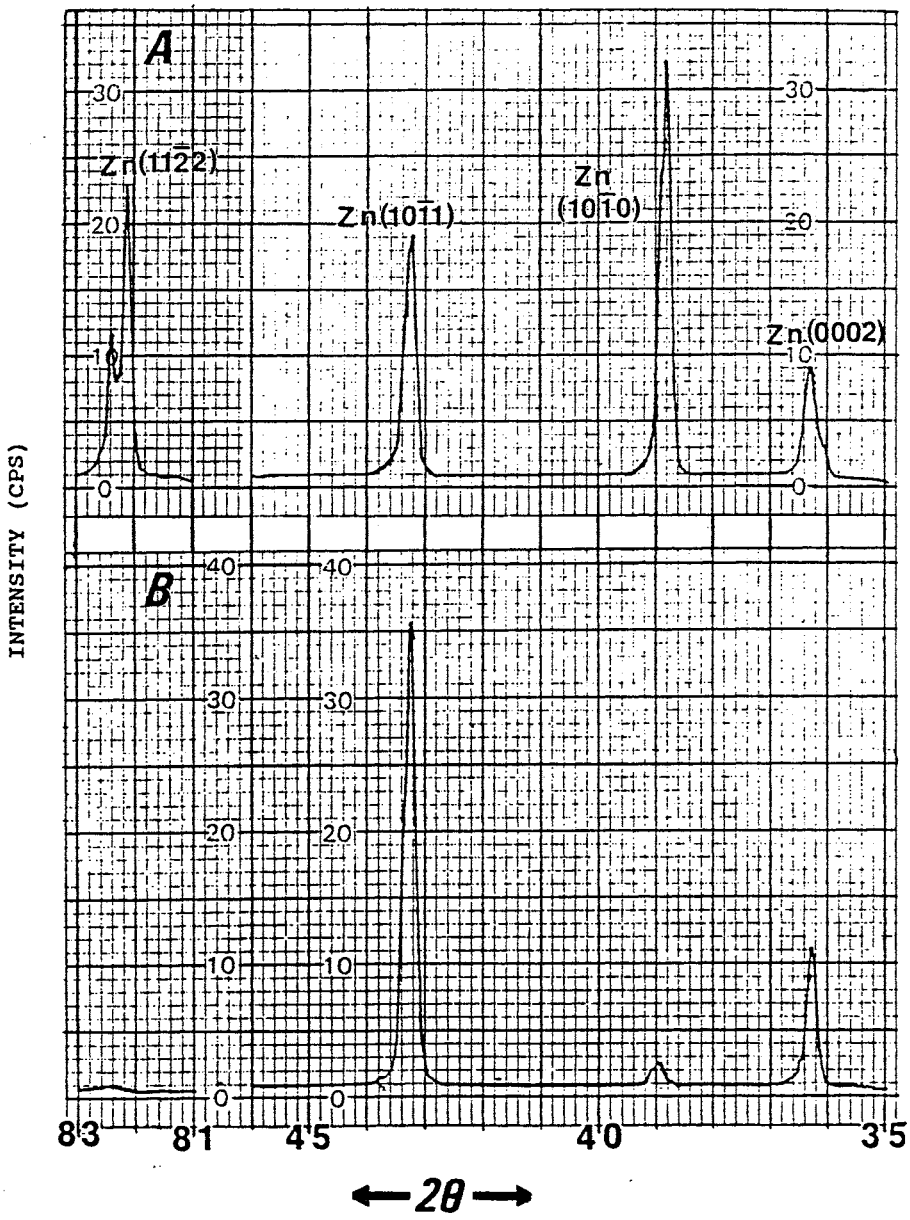

Figure 38 X-ray diffraction pattern obtained from hot dip zinc coating, specimen X. Plots A and B show profiles from different locations on specimen X

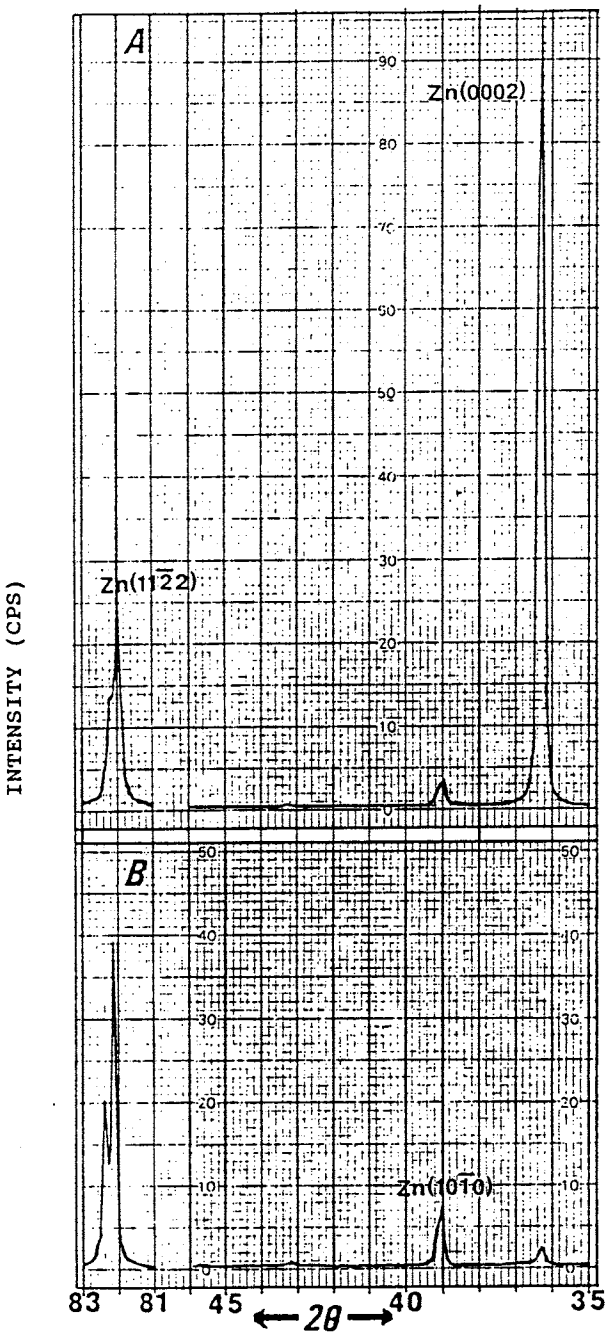

Figure 39 X-ray diffraction pattern obtained from hot dip zinc coating, specimen Y. Plots A and B show profiles from different locations on specimen Y

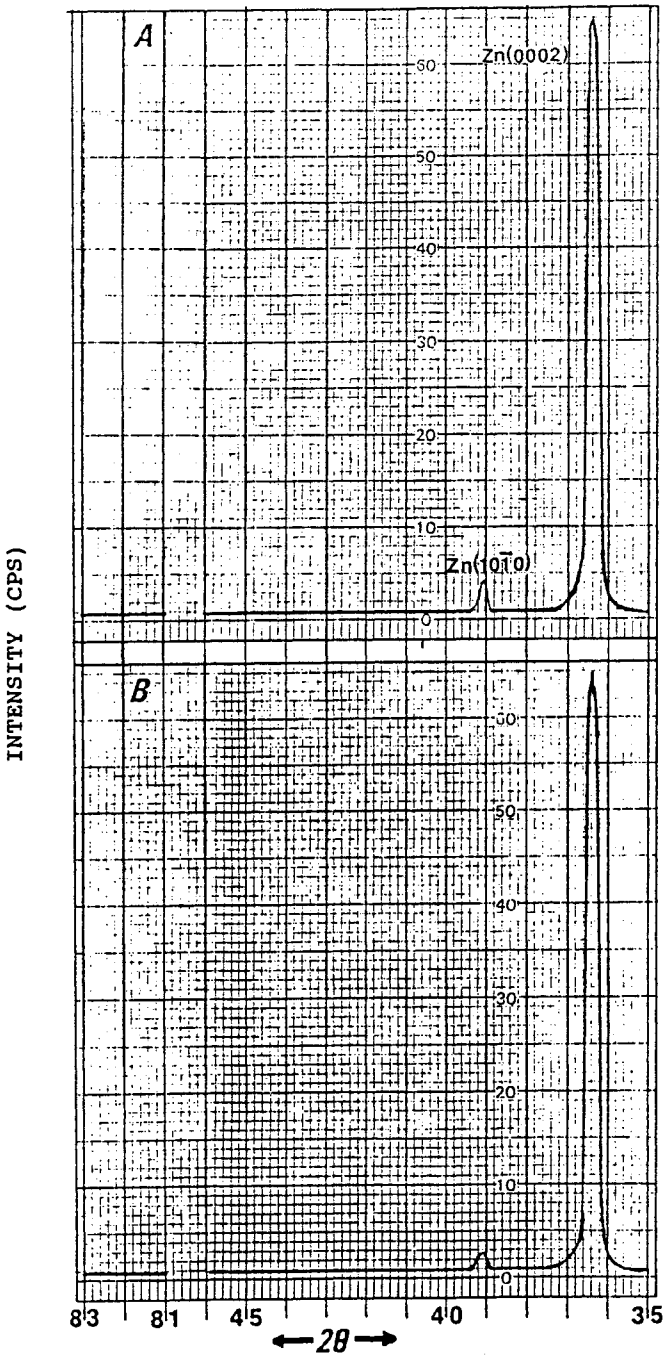

Figure 40 X-ray diffraction pattern obtained from hot dip zinc coating, specimen Z. Plots A and B show profiles from different locations on specimen Z

shows a lack of preferred basal plane orientation parallel to the coating surface.

The coating materials chosen for friction analysis were also subjected to X-ray analyses in the as-received condition. Figure 41 shows the X-ray diffraction pattern obtained on the surface of Inland 70G70G, an electrogalvanized zinc coating. This coating has a dominant Zn{10$\bar{1}$3} peak, i.e., many crystals have the {10$\bar{1}$3} planes parallel to the surface. This suggests that the basal planes of the crystals are favorably tilted to the surface for plastic flow during stretching operations.

Figure 42 shows the X-ray diffraction pattern obtained on Stelco 60HD, a hot dip pure zinc coating. A very strong basal plane texture is present in these coatings. Stelco 60HD is a coarse spangled coating. Thus only few spangles contribute to diffracted peak intensities. The consistent dominance of the Zn{0002} peak in several samples analyzed suggests a truly strong basal plane texture in all the spangle sectors.

Figure 43, shows the X-ray diffraction pattern obtained on the galvannealed coating in Table 6 (Inland

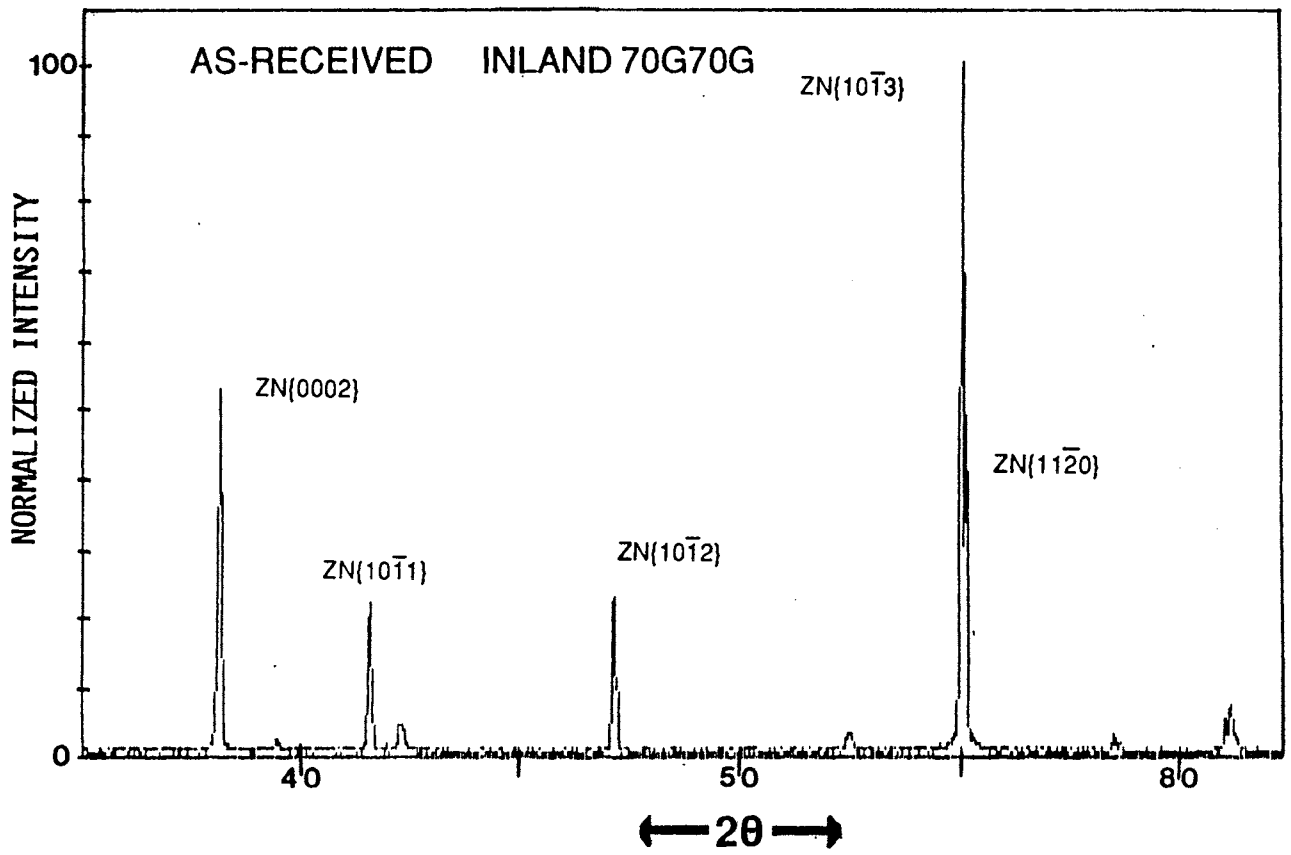

Figure 41 X-ray diffraction pattern obtained from as-received Inland 70/70 electrogalvanized zinc coating surface

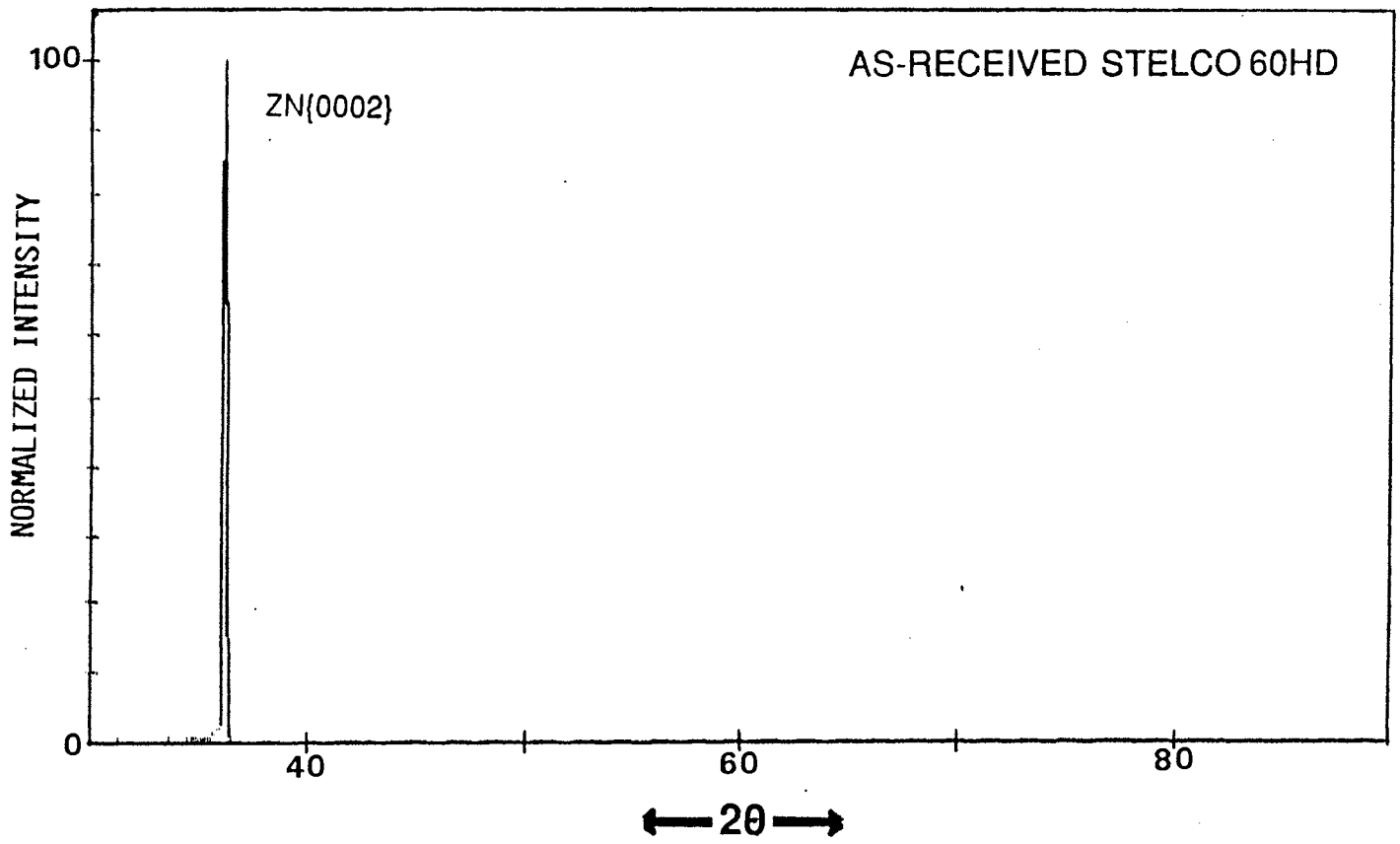

Figure 42 X-ray diffraction pattern obtained from an as-received Stelco 60HD hot dip zinc coating surface

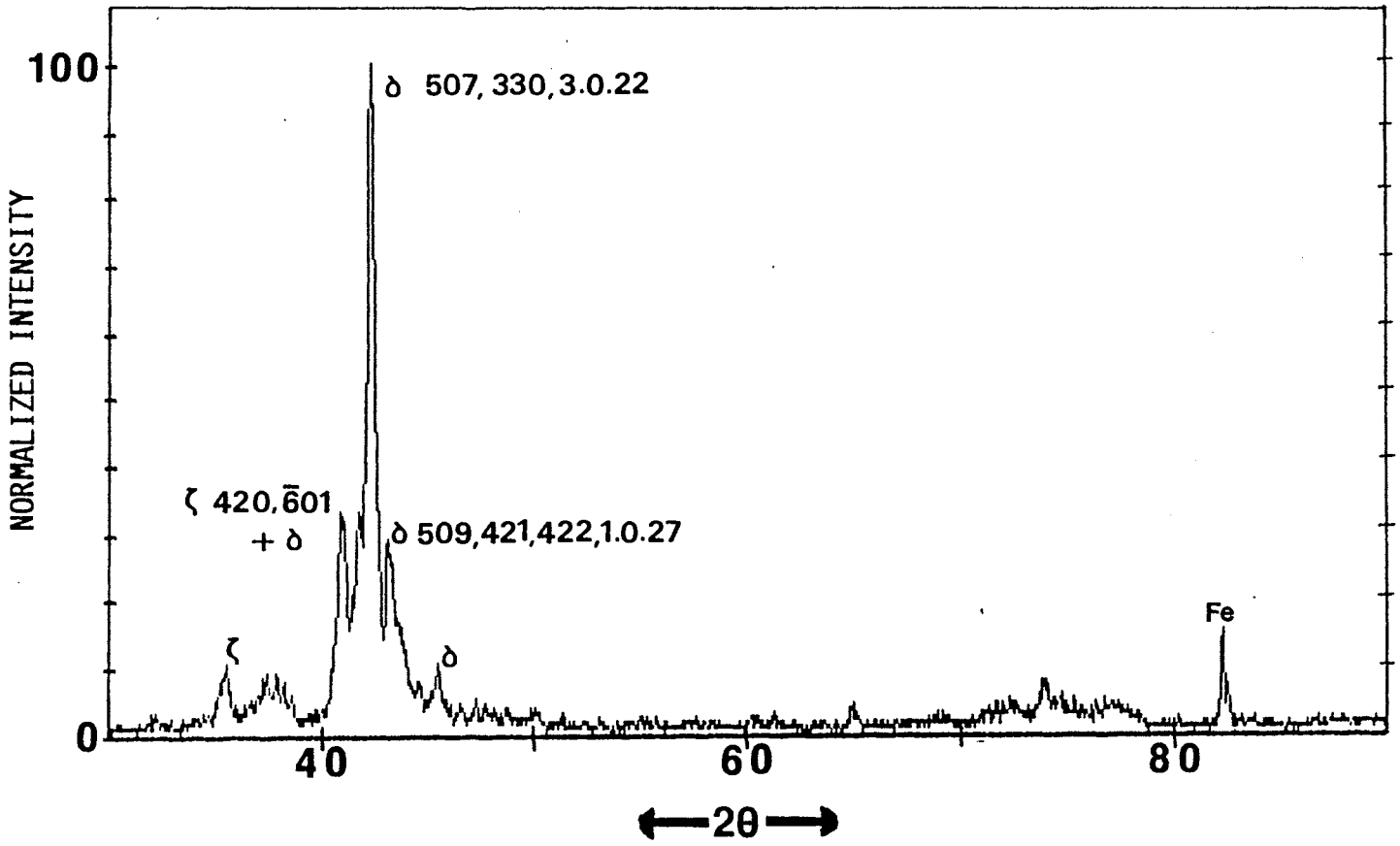

Figure 43 X-ray diffraction pattern obtained from an as-received Inland 60N40N galvannealed coating surface

60N40N). The peaks in the diffraction pattern originate from the different Zn-Fe phases present in these coatings. The pure zinc peaks are absent and the pattern observed in Figure 45 is quite different from those obtained for pure zinc. The coating is primarily composed of $\delta(FeZn_{10}$, hcp) and $\zeta(FeZn_{13}$, monoclinic) phases (Refer to Table 2). From the X-ray diffraction patterns, the coating appears to have a ($\delta+\zeta$) two phase region with traces of Γ_1 closer to the steel-coating interface. The phases were identified primarily by comparing observed X-ray peak positions in the diffraction patterns, with those published in literature for these phases by Bastin and Van Loo (78-80). As seen in Figure 1, which shows a portion of the Fe-Zn phase diagram, a gradient in Fe composition in the coating can establish layers of ($\delta+\Gamma_1$), δ and ($\delta+\zeta$) phases in the coating, starting from the steel-coating interface and ending at the free surface. The pure zinc phase, η, seems to be absent in the coating. The intermetallic phases ζ, δ and Γ_1, are brittle and promote extensive cracking in the coating when the coating is subjected to stretching strains.

The most prominent peak from powder samples of the δ phase occurs at a d-spacing of 2.13Å (79). In the

galvannealed samples, this prominent δ-phase peak is the dominant peak occurring at a 2θ value of 42.3°, which is shown in Figure 43. Other δ phase peaks found in the galvannealed coating however, differ in their intensity ratios with respect to the dominant peak. Thus some amount of texture is present in this phase. The most dominant ζ phase peak, in a powder sample occurs at a d-spacing of 2.17 Å or a 2θ value of 41.5° (80). Other ζ peaks are clustered in a 2θ range between 40° to 44°, along with overlapping δ phase peaks (79, 80). As a result of such peak interferences, no conclusions can be made on either the amount of ζ phase in the coating or texture in ζ phase.

5.1.3 Summary of Understanding Gained from Microstructure and Texture Evaluation on As-Received Coatings

Among the electrogalvanized coatings chosen for uniaxial tension tests, the EG30 coating has an excess number of grains with the $\{11\bar{2}2\}$ planes parallel to the surface of the coating. These grains grow preferentially as the weight of the coating is increased to 70gm/m^2 (EG70) and 100gm/m^2 (EG100). As a result, the heavier electrogalvanized coatings have a marked texture on the surface with a larger percentage of grains with the $\{11\bar{2}2\}$

planes parallel to the surface. With this texture, the basal planes, the primary slip planes in hcp zinc are favorably oriented for high resolved shear stress when subjected to uniaxial tension. The electrogalvanized zinc coating Inland 70G70G, chosen for friction testing has a $Zn\{10\bar{1}3\}$ texture, which is also favorable for plastic flow when the coating is subjected to stretching strains.

The texture which developed in the electrogalvanized coatings with an increase in coating weight appears to be a result of preferential nucleation of certain grains with proper texture relationship with the steel substrate and the subsequent preferential growth of these grains. The growth of the zinc crystals in the electrodeposit must be a function of the plating conditions, since surface morphology has been shown to be a function of plating conditions (73).

A basal plane texture develops in most hot dip zinc coatings. The zinc-rich phase of the hot dip Zn-Al alloy coating Galfan also develops a strong basal plane texture. Other investigators have shown that a strong basal plane texture develops in hot dipped coatings when intermetallic compounds are not formed (81), as in the case of Galfan.

Most hot dip coatings analyzed in this work, showed a basal plane texture parallel to the coating surface. A basal plane texture is not an ideal orientation for flow when tensile stresses act parallel to the coating surface because, the resolved shear stress on the basal slip planes is zero.

The Zn-Fe alloy coating, Inland 60N40N galvannealed, is composed of brittle intermetallic phases, which can promote cracking in the coating, when subjected to stretching strains.

5.2 Coating Deformation in Uniaxial Tension

In this section, results on changes in coating microstructure and texture, with strain in uniaxial tension tests will be presented. The coatings that were subjected to uniaxial tension tests are listed in Table 3

5.2.1 Microstructure of Deformed Coatings

All coated steel sheets listed in Table 3 were deformed and fractured in uniaxial tension. Only the results on the EG100 and the Galvalume coated samples are

presented here as representative examples of different coating deformation behaviors (68,11). Figure 44 shows the same region on an EG100 microtension specimen strained to 20% [Figure 44a] and 50% [Figure 44b]. The tensile axis runs vertical in the plane of the paper. The arrows in the lower right-hand corner illustrate the extensive plastic deformation sustained by the electrogalvanized coating. The arrow in the middle of each micrograph shows a grain that deforms along its basal slip planes and rotates with increasing amounts of strain. Similar observations on the EG30 coating after straining showed areas of exposed steel due to considerable thinning of the coating by plastic deformation (68,11).

Figure 45 shows a selected region on the surface of a Galvalume microtension specimen after tensile strains of 12% [Figure 45a] and 31% [Figure 45b] (70,11). A network of smaller cracks develops at low strains [Figure 45a], then coalesce and widen to form larger cracks with increasing strain. This suggests that the coating accommodates strain mainly by interdendritic cracking. Figure 46 shows regions on a Galvalume tension specimen, very close to the neck (68). Figure 46a shows a large crack in the coating exposing the steel substrate. The

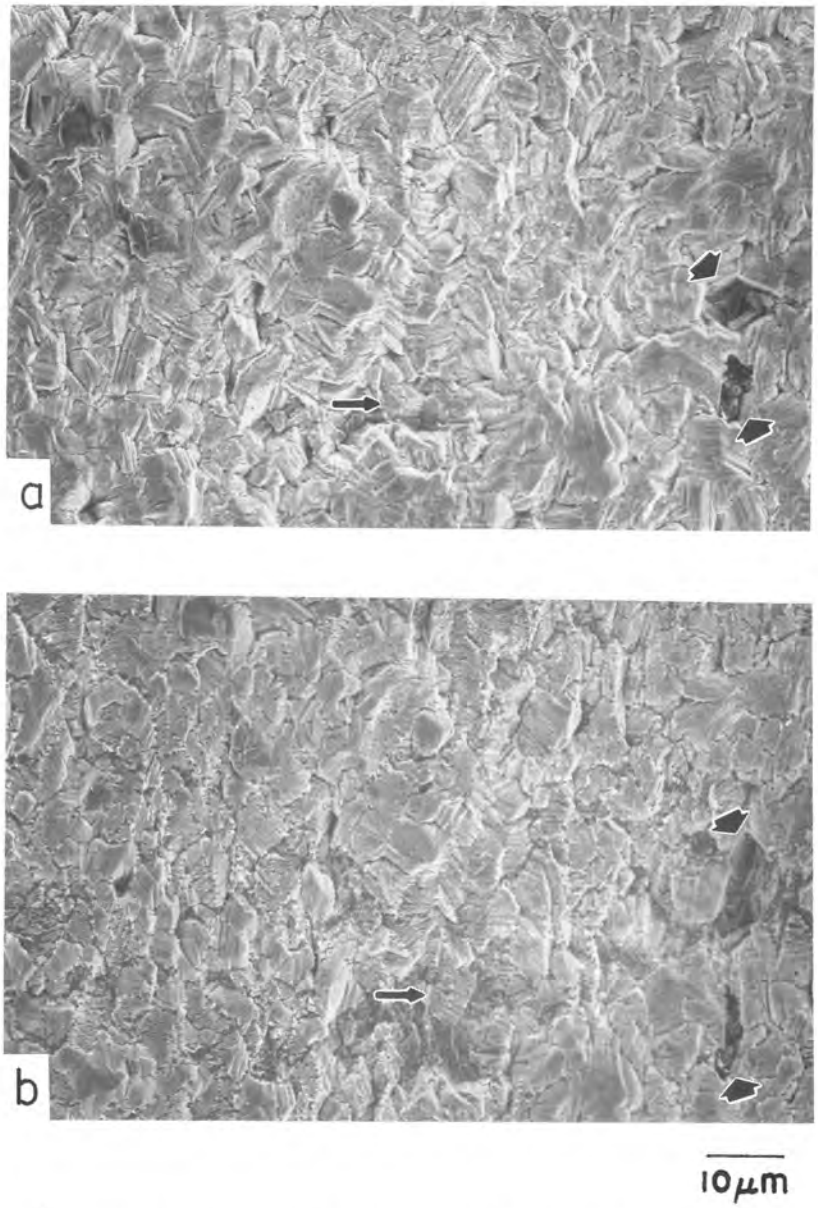

Figure 44 A selected area on a EG100 microtension specimen after (a) 20% strain (b) 50% strain

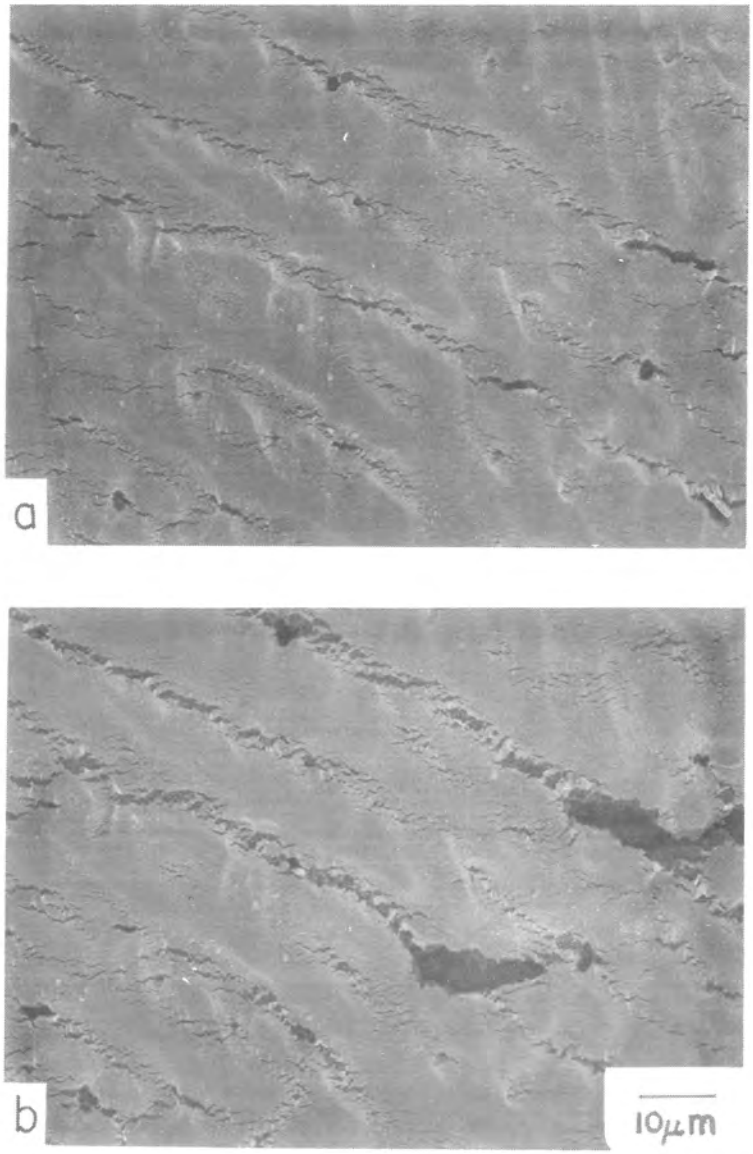

Figure 45 A selected region on a Galvalume microtension sample after (a) 12% strain (b) 31% strain

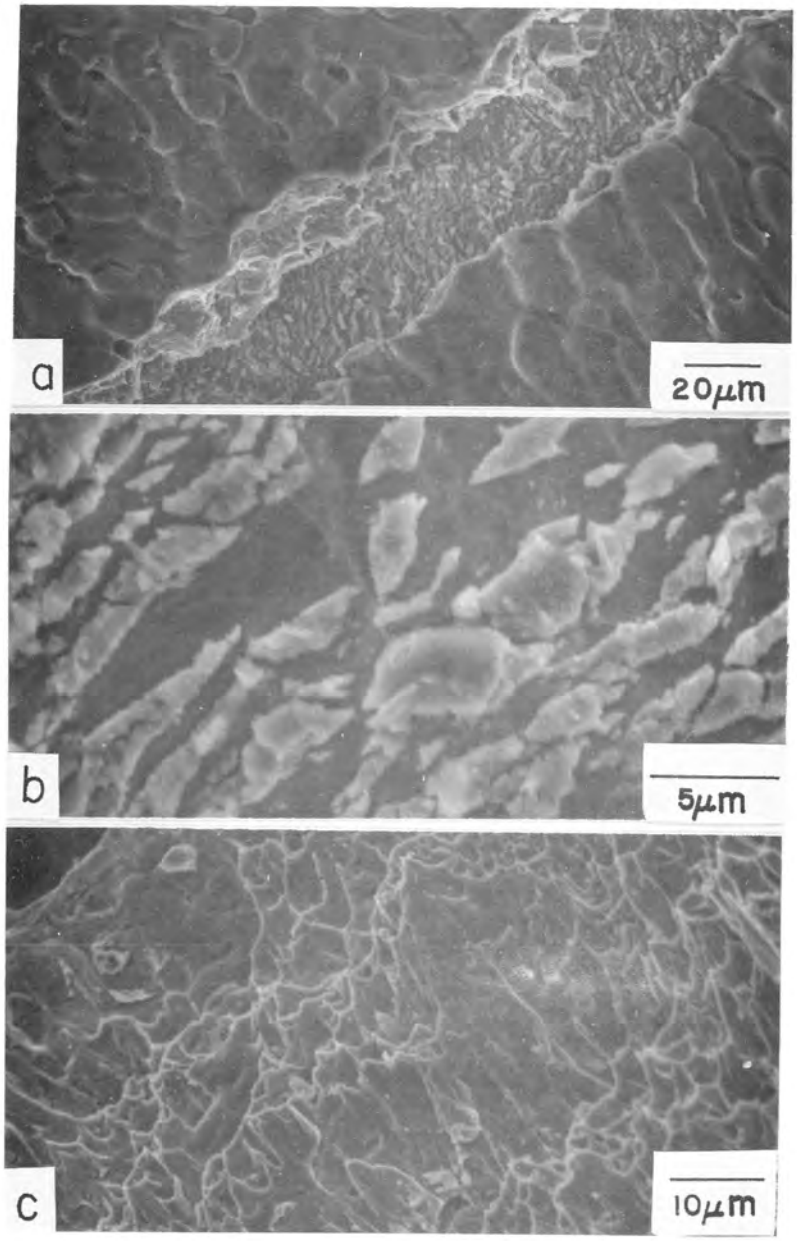

Figure 46 Fracture areas adjacent to the necked region of a Galvalume tension specimen a) crack in the coating, b) particles on the steel substrate, within the crack, c) underside of a section of Galvalume coating which separated from the steel substrate at the neck

crack is approximately 20 μm wide. Within the crack there were Al-Zn particles adherent to the steel substrate. The particles were found on exposed steel surfaces, wherever there were cracks in the coating. Figure 46b shows a high magnification micrograph of these particles. The EDS spot analysis on these particles gave a composition of approximately 70 at% Al, 24 at% Zn, 4 at% Fe and 2 at% Si. The particles appear to be part of the first Al-rich layer in the overlay. The fracture of these particles may be due to the inability of the intermetallics (21) in the alloy layer to flow with the steel substrate. Therefore, cracks open and particles are separated as the steel continues to flow. Analysis of the area between the particles gave primarily Fe with minor amounts of Al, Zn and Si. The higher Si percentage in the particle could imply some amount of Si enrichment. Figure 48c shows the underside of a portion of the Galvalume coating which separated from the steel substrate at the neck. It shows evidence for shear and/or ductile fracture in a layer of the coating close to the interface. The voids are interpreted to result from shear around intermetallic particles on the steel substrate (Figures 46a and 46b).

Uniaxial tension tests of Galfan revealed extensive

microcracking in the coating (11). The cracks grew with strain. The next section will present results of studies on texture changes with deformation. This work was performed to complement SEM observations on deformation and give conclusive evidence for plastic flow in the coating materials.

5.2.2 Texture changes with Deformation in Uniaxial Tension Tests

Texture changes during uniaxial tensile deformation were monitored for the coatings listed in Table 4, in terms of variations in deviation parameters of Zn peaks with strain. Tables 8-10 show the variation in deviation parameters of the zinc peaks with strain in the electrogalvanized coatings. The electrogalvanized coatings chosen for this study showed preferential development of Zn$\{11\bar{2}2\}$ texture with coating weight (Refer to Section 5.1.2) in the as-received condition. Therefore changes in the deviation parameter of Zn$\{11\bar{2}2\}$ and Zn$\{0002\}$ were monitored as a function of strain. Figures 47 and 48 show plots of $\Delta\{11\bar{2}2\}$ changes and $\Delta\{0002\}$ respectively, as a function of strain in these coatings. The EG100 and EG70 coatings show a substantial change in $\Delta\{11\bar{2}2\}$ compared to

Table 8 Deviation parameters of zinc peaks as a function of strain on a EG30 coating

% Strain	$\Delta\{0002\}$	$\Delta\{10\bar{1}0\}$	$\Delta\{10\bar{1}2\}$	$\Delta\{11\bar{2}2\}$
0%	-81%	-57%	-39%	+35%
10%	-81%	-55%	-43%	+28%
21%	-85%	-65%	-25%	-13%
34%	-81%	-60%	-36%	-17%
49%	-81%	-62%	-39%	-39%

Table 9 Deviation parameters of zinc peaks as a function of strain on a EG70 coating

% Strain	$\Delta\{0002\}$	$\Delta\{10\bar{1}0\}$	$\Delta\{10\bar{1}2\}$	$\Delta\{11\bar{2}2\}$
0%	-64%	-60%	-36%	+230%
11%	-72%	-60%	-32%	+152%
19%	-79%	-65%	-14%	+48%
28%	-79%	-67%	-21%	+26%
39%	-83%	-67%	-25%	-22%

Table 10 Deviation parameters of zinc peaks as a function of strain on a EG100 coating

% Strain	Δ{0002}	Δ{10$\bar{1}$0}	Δ{10$\bar{1}$2}	Δ{11$\bar{2}$2}
0%	-51%	-60%	+7%	+256%
10%	-64%	-62%	-4%	+200%
20%	-70%	-62%	0%	+61%
36%	-75%	-70%	-7%	+9%
42%	-75%	-70%	-11%	-17%

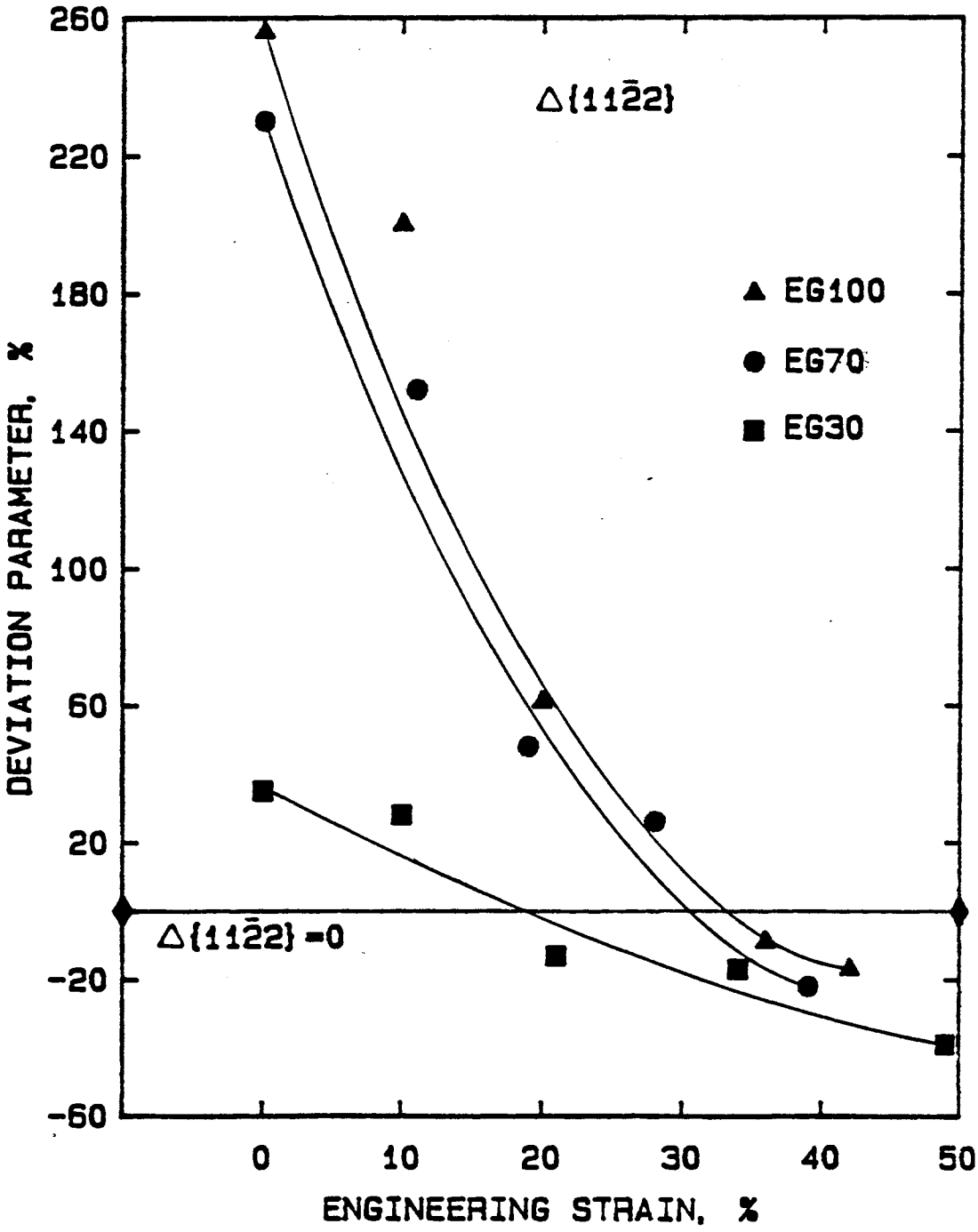

Figure 47 Deviation parameter of Zn{11$\bar{2}$2} plotted as a function of engineering strain for electrogalvanized coatings tested in uniaxial tension

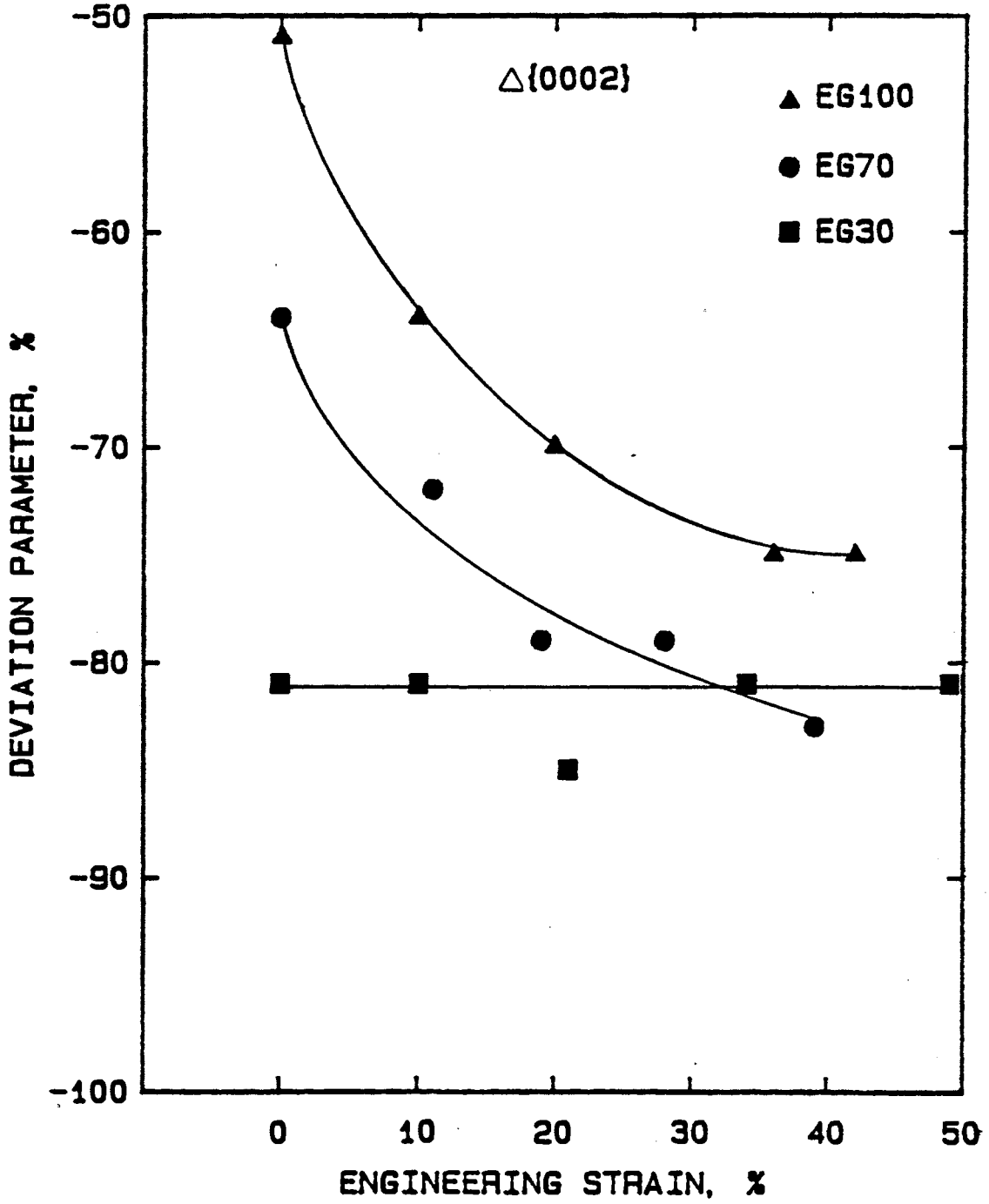

Figure 48 Deviation parameter of Zn{0002} plotted as a function of engineering strain for electrogalvanized coatings tested in uniaxial tension

EG30, Figure 47. The fact that $\Delta\{11\bar{2}2\}$ changes in all three coatings is indicative of slip and rotation of crystals on the surface, while the larger changes in $\Delta\{11\bar{2}2\}$ in EG100 and EG70 are a result of the strong $Zn\{11\bar{2}2\}$ texture present in these coatings in the undeformed as-coated condition. When the crystals in the coating slip and rotate to accommodate the strain, the $Zn\{11\bar{2}2\}$ planes are rotated and the deviation parameter decreases significantly. This is seen in Figure 47 where the change in $\{11\bar{2}2\}$ is quite steep at lower strains. Figure 48 shows that $\Delta\{0002\}$ becomes more negative with increase in strain in the EG100 and EG70 coatings. The EG30 shows no change in $\Delta\{0002\}$ with strain.

The deviation parameters of several peaks listed in Tables 8-10 seem to approach a similar set of values for all three electrogalvanized coatings at higher strains. Also, the values are all significantly negative. Since the peak intensities were normalized to $Zn\{10\bar{1}1\}$ in the electrogalvanized coatings, the negative deviation parameters suggest a stabilization of $Zn\{10\bar{1}1\}$ texture parallel to coating surface at higher strains in these coatings.

Consider texture changes in the zinc-alloy coatings listed in Table 3. Table 11 shows deviation parameters of Zn peaks in Galfan becoming less negative with strain. Galfan has a strong basal plane texture in the as-received condition (Section 5.1.2). Therefore the peak intensities were normalized with respect to Zn{0002} in Galfan. Table 11 shows that the basal plane peak is becoming relatively less prominent with strain. However, the magnitude of this texture change is small, and indicates only a minimal amount of plastic deformation by slip in the coating. SEM observations on the surface of deformed Galfan samples show microcracking occurring in the coating with strain (11). These observations suggest that a Galfan coating accommodates strain by a combination of plastic deformation and cracking in the coating.

The Al X-ray diffraction peaks in Galvalume showed considerable anisotropy in intensities with rotation about the normal to the diffracting surface (Figure 36). Therefore it was difficult to monitor Al peak intensities as a function of strain. The Zn peaks themselves did not show a significant trend in intensity changes with strain. The Zn$\{10\bar{1}1\}$ was the most prominent peak in the diffraction pattern obtained on both the as-received and strained

Table 11 Deviation parameters of zinc peaks as a function of strain on a Galfan coating (Relative intensities were normalized to Zn(0002))

% Strain	$\Delta\{10\bar{1}0\}$	$\Delta\{10\bar{1}1\}$	$\Delta\{10\bar{1}2\}$	$\Delta\{11\bar{2}2\}$
0%	-85%	-84%	-92%	-95%
10%	-80%	-75%	-88%	-93%
21%	-68%	-66%	-83%	-88%
34%	-67%	-68%	-83%	-88%
48%	-63%	-59%	-74%	-84%

Galvalume samples.

5.2.3 Summary of Understanding Gained from Uniaxial Tension Tests

The results from the microstructure and texture evaluations on the electrogalvanized pure zinc and hot dip Zn-Al alloy coatings, as a function of uniaxial tensile strain, have provided the following information. The electrodeposited zinc grains with $\{11\bar{2}2\}$ surface planes, are favorably oriented for high resolved shear stress on the primary slip systems (on basal planes) when the coated sheet steel is subjected to uniaxial tension. As these coatings are strained the Zn grains slip and rotate, causing significant changes in surface texture with strain. A favorable texture for plastic deformation yields good substrate coverage except in the thinnest coatings subjected to the highest strains.

In order to confirm the above observations on texture changes with strain in electrogalvanized coatings, pole figure measurements were performed on EG100 samples. The densities of $\{11\bar{2}2\}$ and $\{0002\}$ poles as a function of the tilt and azimuthal angles were obtained on as-received and

strained EG100 samples. Figures 49 and 50 show the Zn{11$\bar{2}$2} and Zn{0002} pole figures for the as-received sample. A strong {11$\bar{2}$2} texture is seen in the as-received coatings. Figures 51 and 52 show the corresponding pole figures for an EG100 sample strained 20% in an uniaxial tension test. The rotation of the {11$\bar{2}$2} poles away from the center and the rotation of the {0002} planes towards the tensile axis (which is parallel to the rolling direction RD indicated in each figure) is clearly seen in these figures. The pole figure measurements confirm the results of the simple deviation parameter analysis. The deviation parameters provide information only on the planes parallel to the surface. They do not give any information on pole densities as a function of the azimuthal and tilt angles. However, it must be realized that for coating deformation the critical point is whether the basal planes {0001} are parallel to the surface.

The Zn-Al alloy coatings, Galvalume and Galfan exhibit extensive cracking during uniaxial tension tests. The network of microcracks formed initially coalesce and widen to form larger cracks with strain. Galvalume coating accommodates strain by interdendritic cracking in the Zn-rich regions, despite a random orientation of zinc

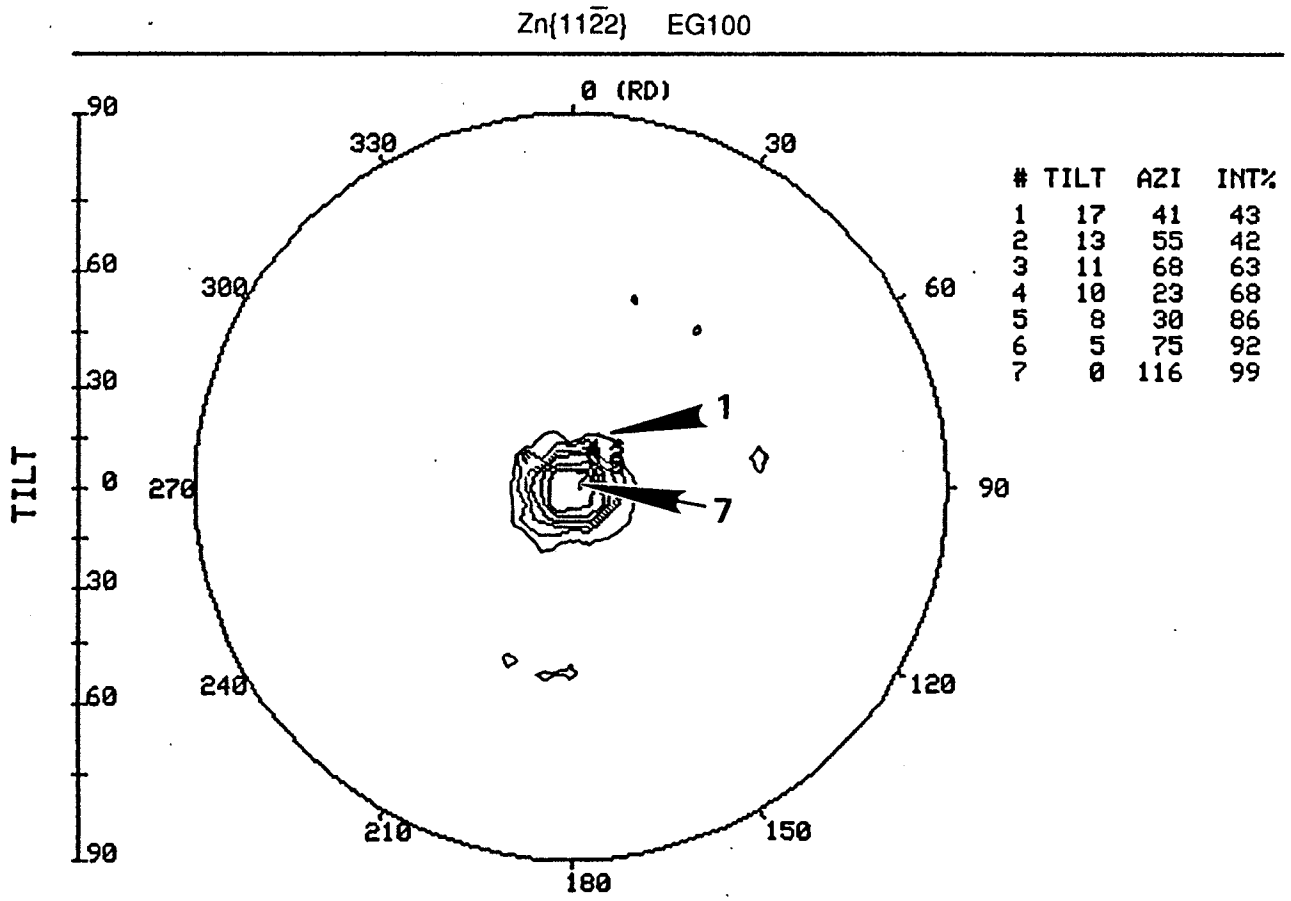

Figure 49 Plot of Zn{11$\bar{2}$2} pole density on as-received EG100 coating (pole densitym measurements not normalized with respect to zinc powder sample)

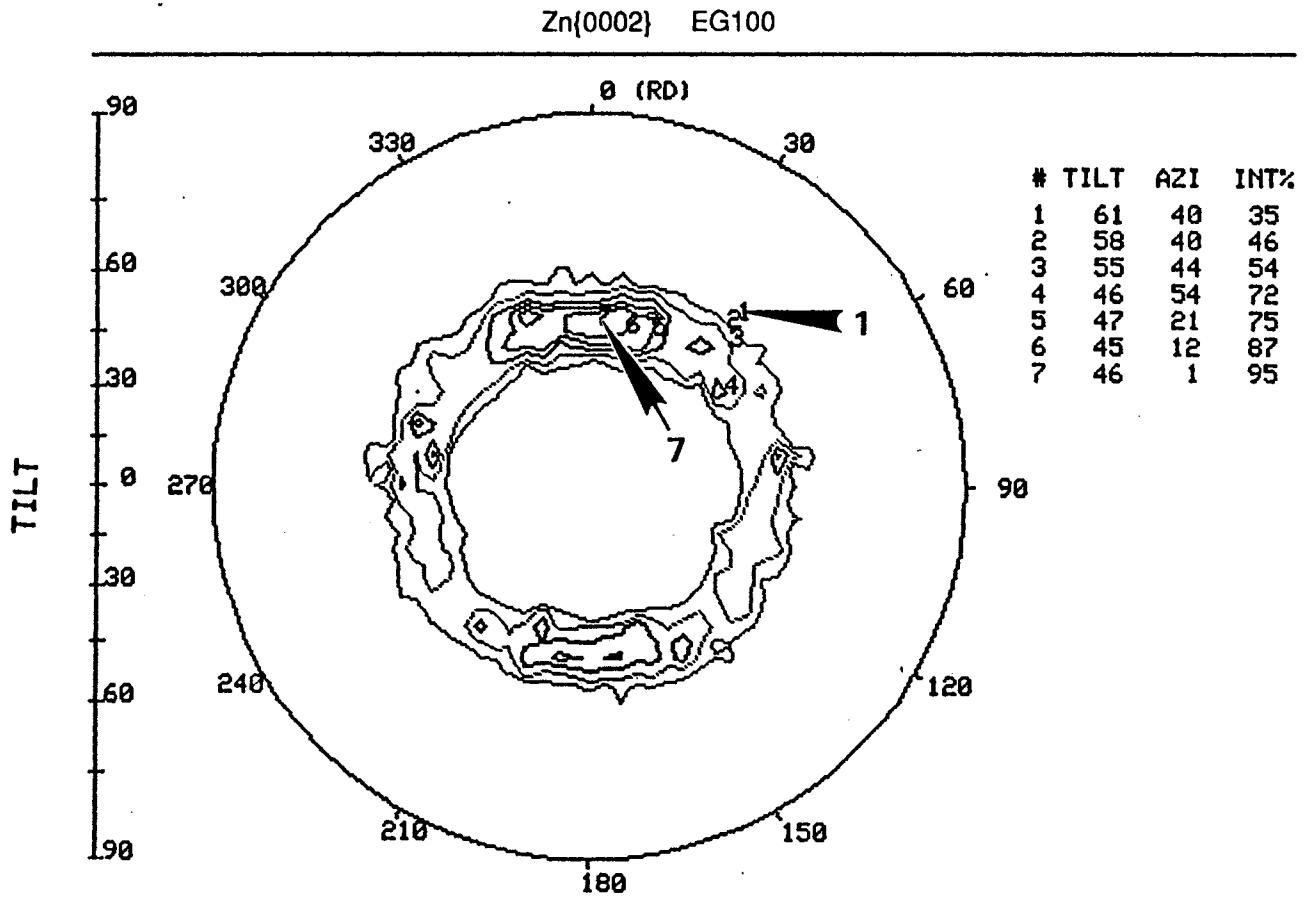

Figure 50 Plot of Zn{0002} pole density on as-received EG100 coating (pole density measurements not normalized with respect to zinc powder sample)

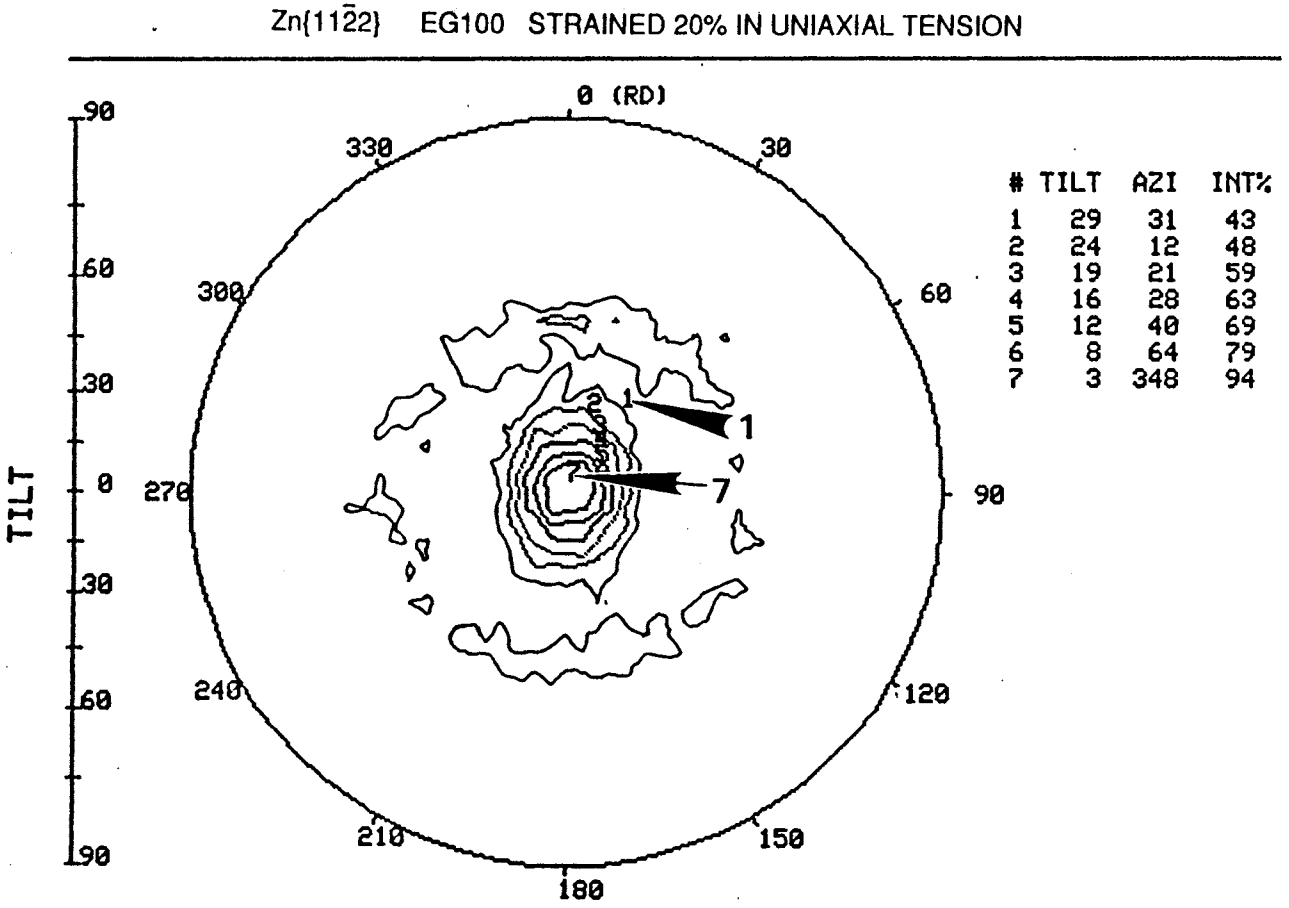

Figure 51 Plot of Zn(11$\bar{2}$2) pole density on a EG100 sample strained to 20% in uniaxial tension (pole density measurements not normalized with respect to zinc powder sample)

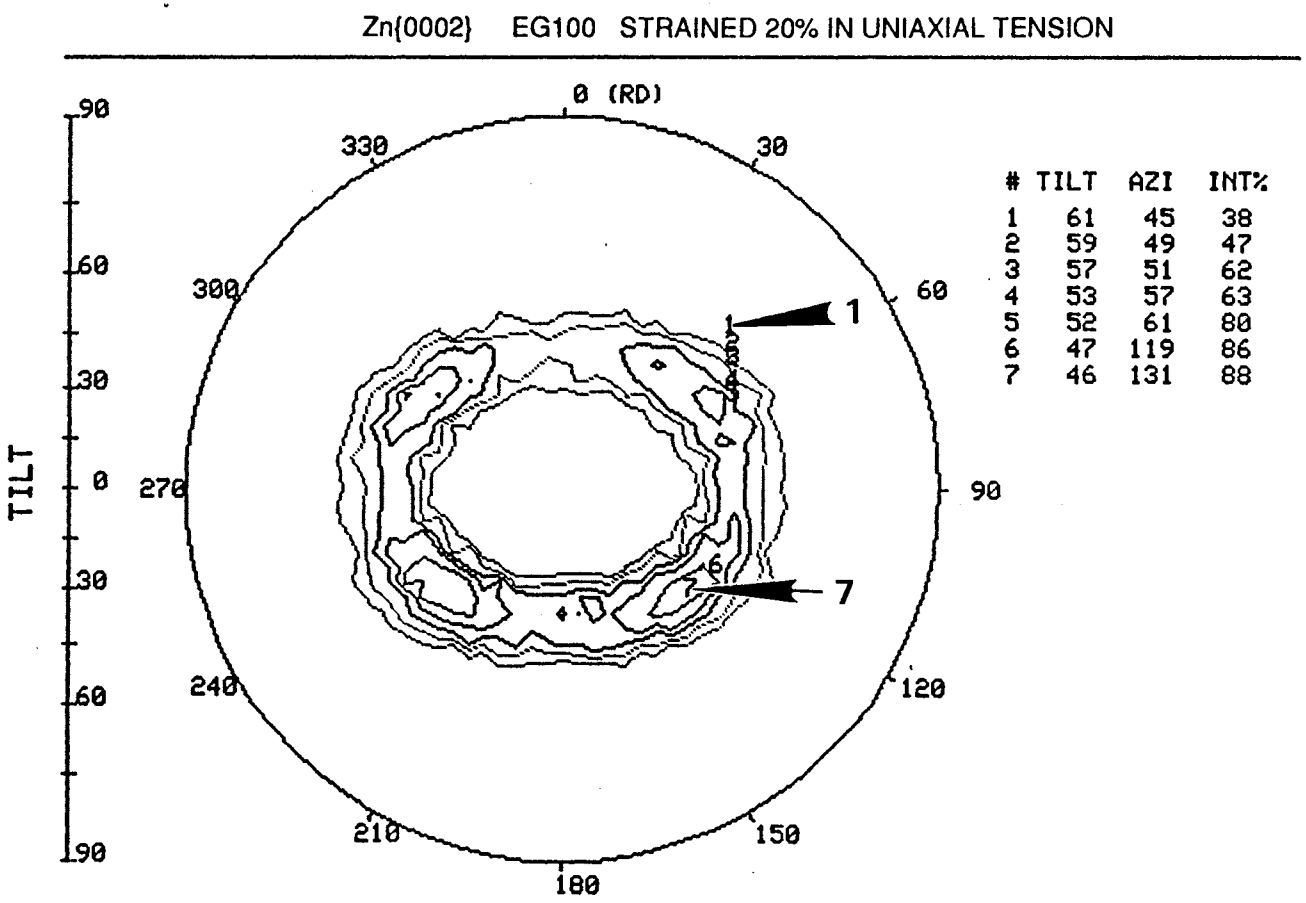

Figure 52 Plot of Zn(0002) pole density on a EG100 sample strained to 20% in uniaxial tension (pole density measurements not normalized with respect to zinc powder sample)

crystals in this region. The ductile fracture in these regions could be the result of a high density of precipitates (Figure 25b). Precipitates promote microvoid formation at the precipitate-matrix interface. Galfan on the other hand exhibits cracking in uniaxial tension tests because it possesses a strong basal plane texture, which is unfavorable for slip under the applied stress state.

The above results show that coating texture and microstructure are two primary material factors that control the mode of strain accommodation in coatings during simple stretching operations.

5.3 Deformation Behavior of Hot Dip Galvanized Coatings in a Biaxial Stretching Operation.

Deformation behavior of three hot-dip coatings X, Y and Z, listed in Table 4, were analyzed in biaxially stretched regions of flexible tubes made from these materials. The flexible tubes were made in a commercial roll forming operation illustrated in Figure 21.

Figure 53 shows representative surface crack morphologies from the three coatings in the biaxially

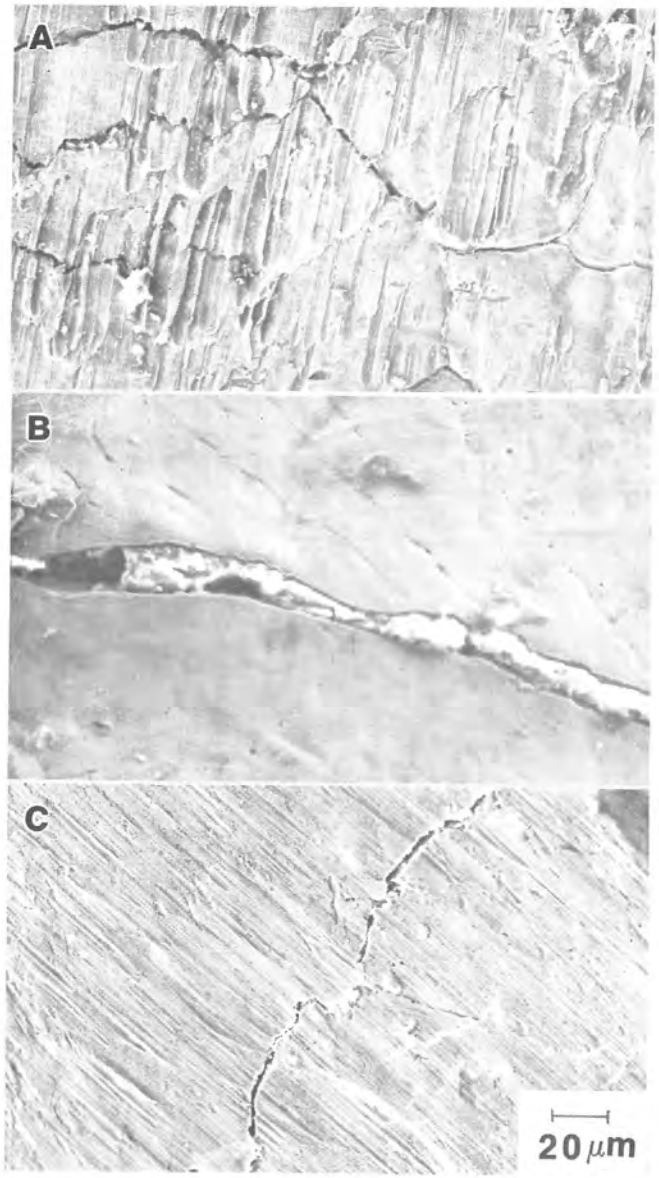

Figure 53 Examples of crack morphologies in a) specimen Z. b) specimen Y and c) specimen X (SEM micrographs)

stretched zones. All three coatings exhibit cracking. Coating X with large spangle size and a low basal plane texture accommodates strain by a combination of plastic flow and cracking. Because most of the forming strain was accommodated by slip, the crack faces showed little separation (Figure 53c). Material Y with a large spangle size and a dominant basal plane texture accommodated strain primarily by the development of large wide cracks without associated plastic flow. As a result, galvanic corrosion was activated and the cracks filled with Zn-based corrosion products (Figure 53b). Material Z with the most dominant basal plane texture, and the smallest spangle size, also exhibited extensive fine cracking (Figure 53a). Since the same amount of strain is accommodated by many cracks in contrast to the large spangled material Y, crack widths were smaller and the critical area of steel required to activate galvanic corrosion was not exposed.

The above results show variable deformation and fracture behavior of hot dip pure zinc coatings subjected to a biaxial strain state. The differences in response to forming stem from the effects of crystallographic texture and spangle size. Non-basal plane textures and small spangle sizes are desirable features in hot dip zinc

coatings in order to avoid wide forming cracks which initiate early occurrence of corrosion in formed parts. Basal plane textures are unfavorable for slip, when coatings are subjected to stretching strains, whether uniaxial or biaxial.

5.4 Analysis of Friction on Coated Sheet Steels

Measurement of frictional properties for coated sheet steels in a bending under tension type strip drawing test is described in Section 2.4.3. Coulombic friction is assumed in the analysis. In this section the implications and the limitations of this analysis are illustrated by experimental results. This is followed by an evaluation of texture and crystal structure effects on friction in coated sheet steels. Finally, experimental measurements of true contact areas on the coatings, as a function of contact pressure in friction tests are presented. These results corroborate the theoretical predictions of Wanheim and Bay model, presented in Section 2.4.5.

5.4.1 Coulombic Friction

Consider an example analysis under the assumptions of

Coulombic friction conditions. Strips of electrogalvanized steel sheet (Inland 70G70G) were subjected to the friction test at various back-tension levels (F_2) (Refer to Figure 3). Figure 54 shows a plot of the forward pulling force F_1, for a free roller condition. The difference between F_1 and F_2 gives F_b, the bending load. In this example, F_b has a value of 66 lbs. Figure 55 plots the pulling force for a fixed roller configuration, at different back-tension levels. A linear regression fit is drawn through the points. If the F_1 values in the fixed roller configuration were corrected for bending, and the (F_1-F_b) values plotted against F_2, the linear fit obtained is shown in Figure 56. This straight line has a negative y intercept. The corresponding values of contact pressure and μ were calculated from Equations 3 and 4 given in Section 2.4.3. μ is plotted as a function of contact pressure in Figure 57. Due to the negative y-intercept, μ decreases with decreasing contact pressure in the low pressure range, as discussed earlier in Figure 4. In comparison to Figure 56, Figure 58 shows a constrained linear regression fit between (F_1-F_b) and F_2. The straight line has been constrained to go through the zero point. μ values calculated from Figure 58 are independent of contact pressure as shown in μ vs. P in Figure 59. The

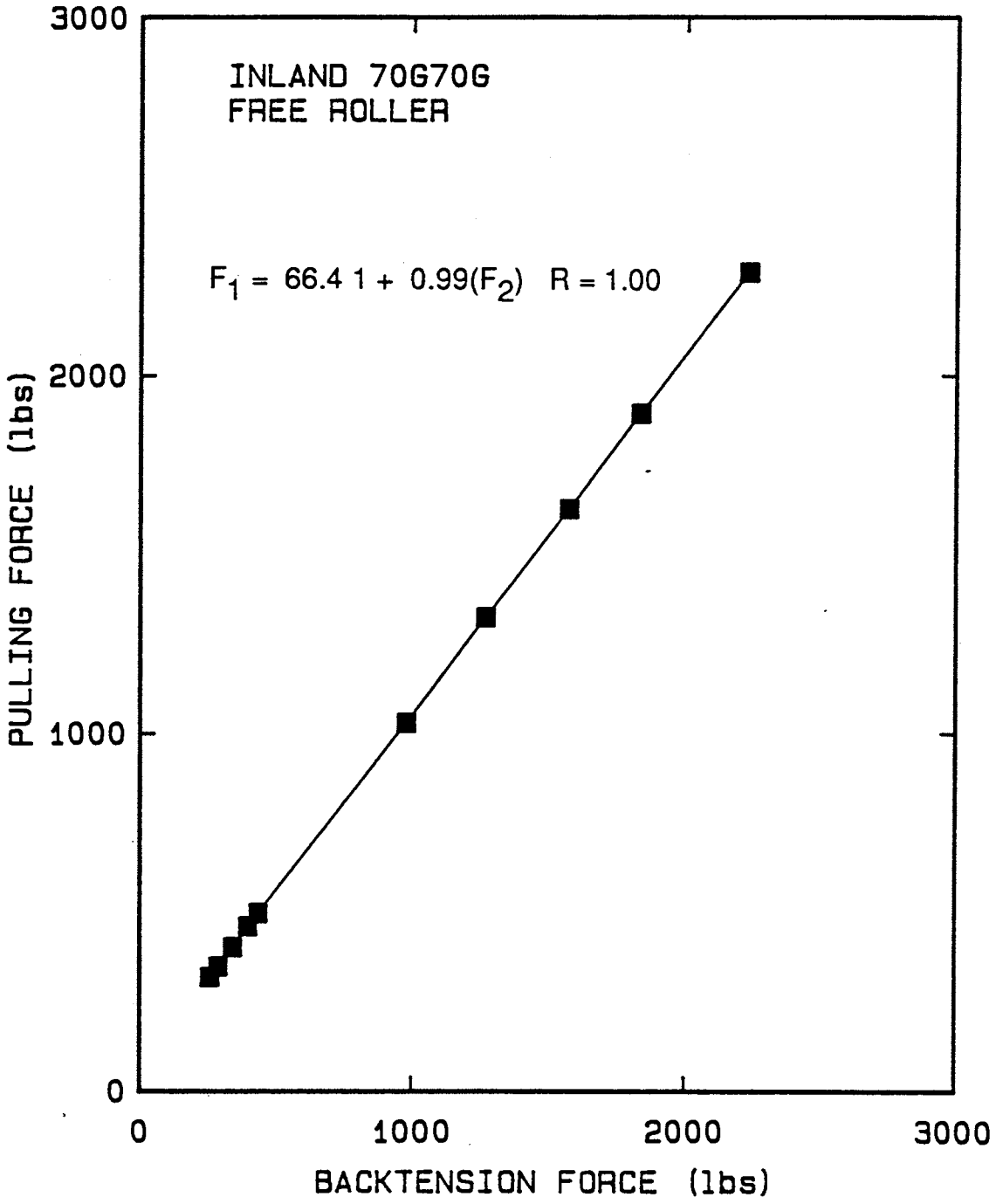

Figure 54 The pulling force F_1, plotted as a function of the backtension force F_2 for a free roller configuration in a bending under tension test at a displacement rate of 100 inches/minute. Y intercept of F_1 gives F_b (Material: Inland 70G/70G)

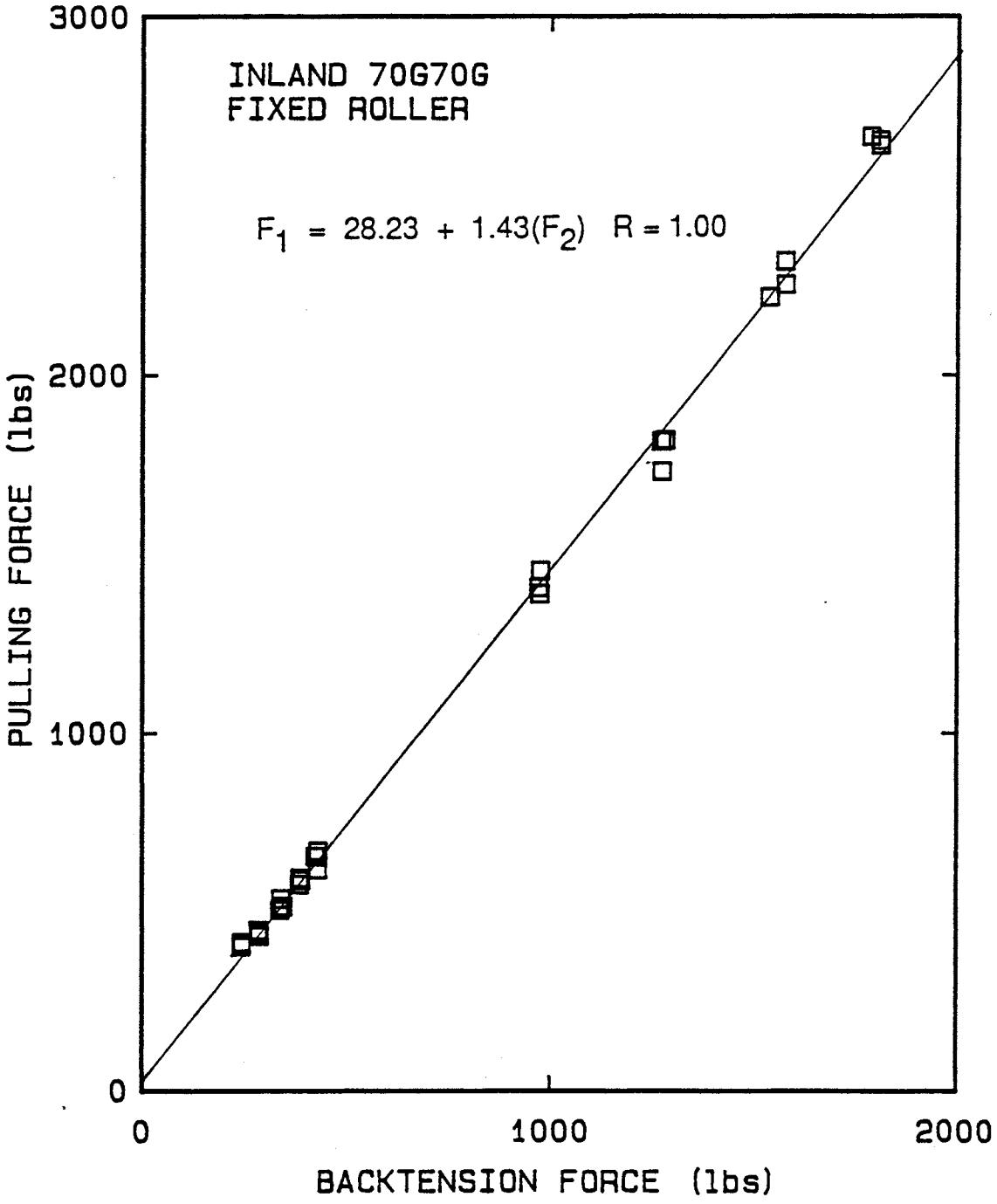

Figure 55 The pulling force F_1 plotted as a function of the backtension force F_2 for a fixed roller configuration in a bending under tension test at a displacement rate of 100 inches/minute. (Material: Inland 70G/70G)

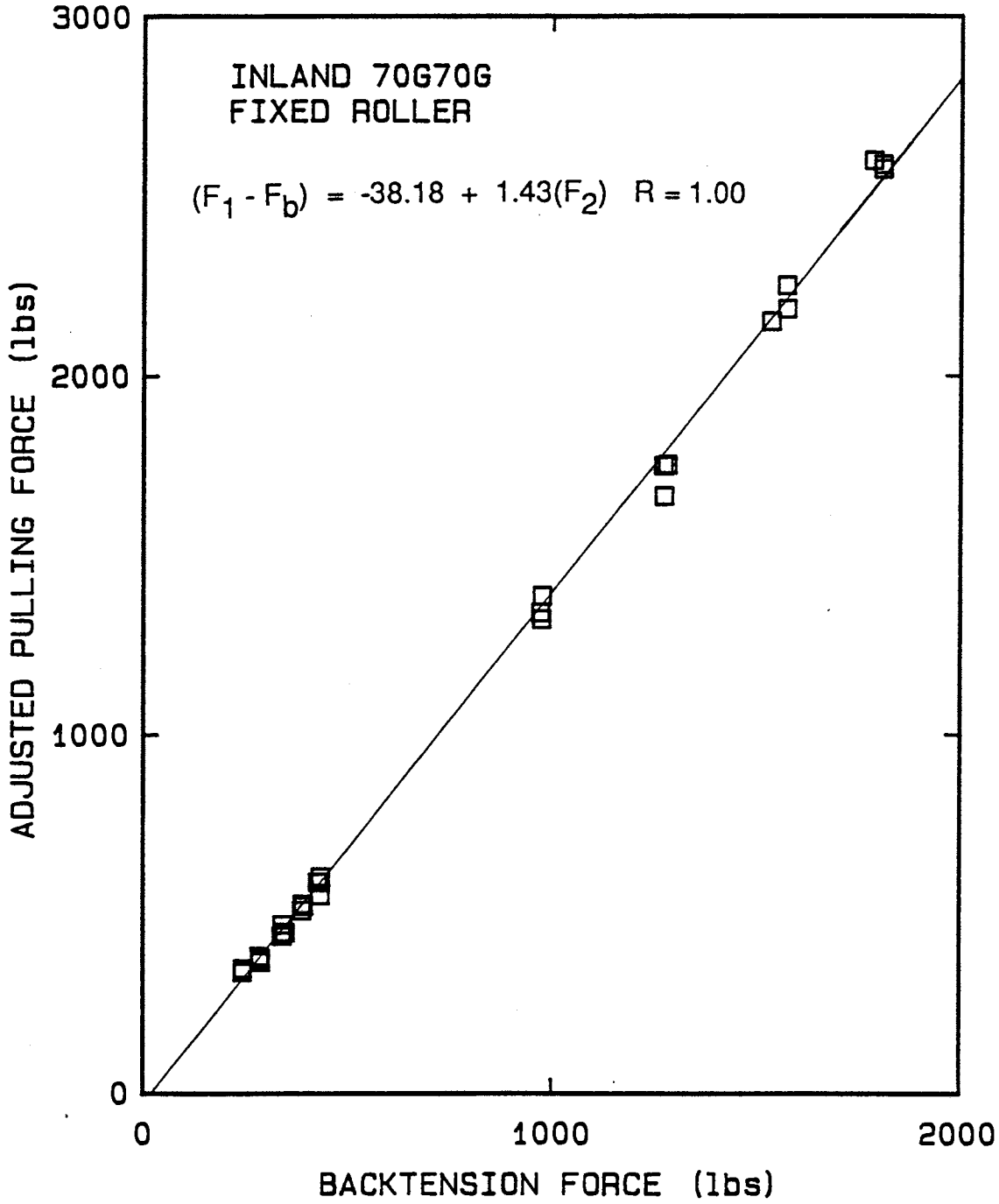

Figure 56 The adjusted pulling force (F_1-F_b) plotted as a function of the backtension force F_2 for the fixed roller configuration in a bending under tension strip drawing test at a displacement rate of 100 inches/minute. (Material: Inland 70G/70G)

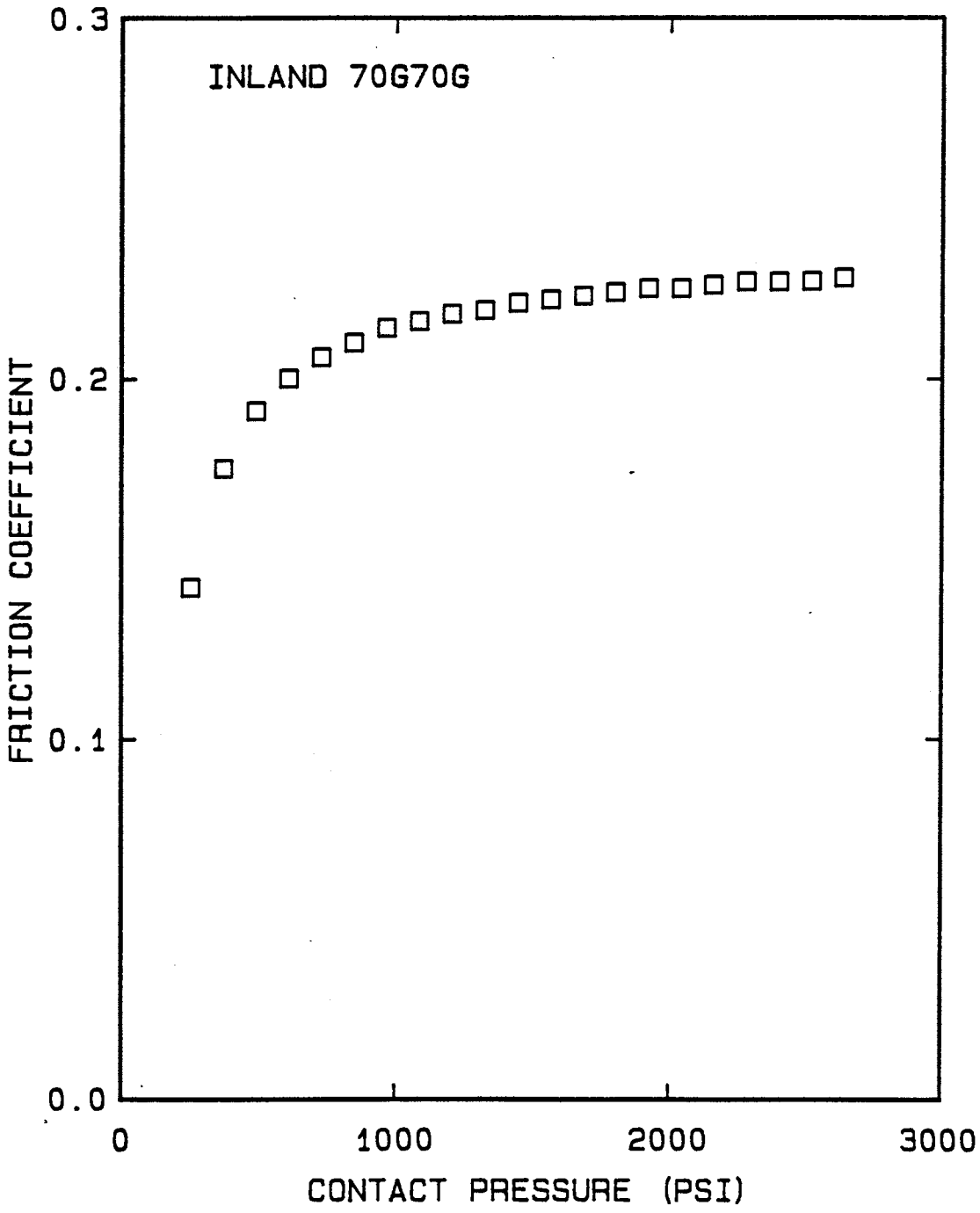

Figure 57 Friction coefficient μ as a function of contact pressure for Inland 70G/70G

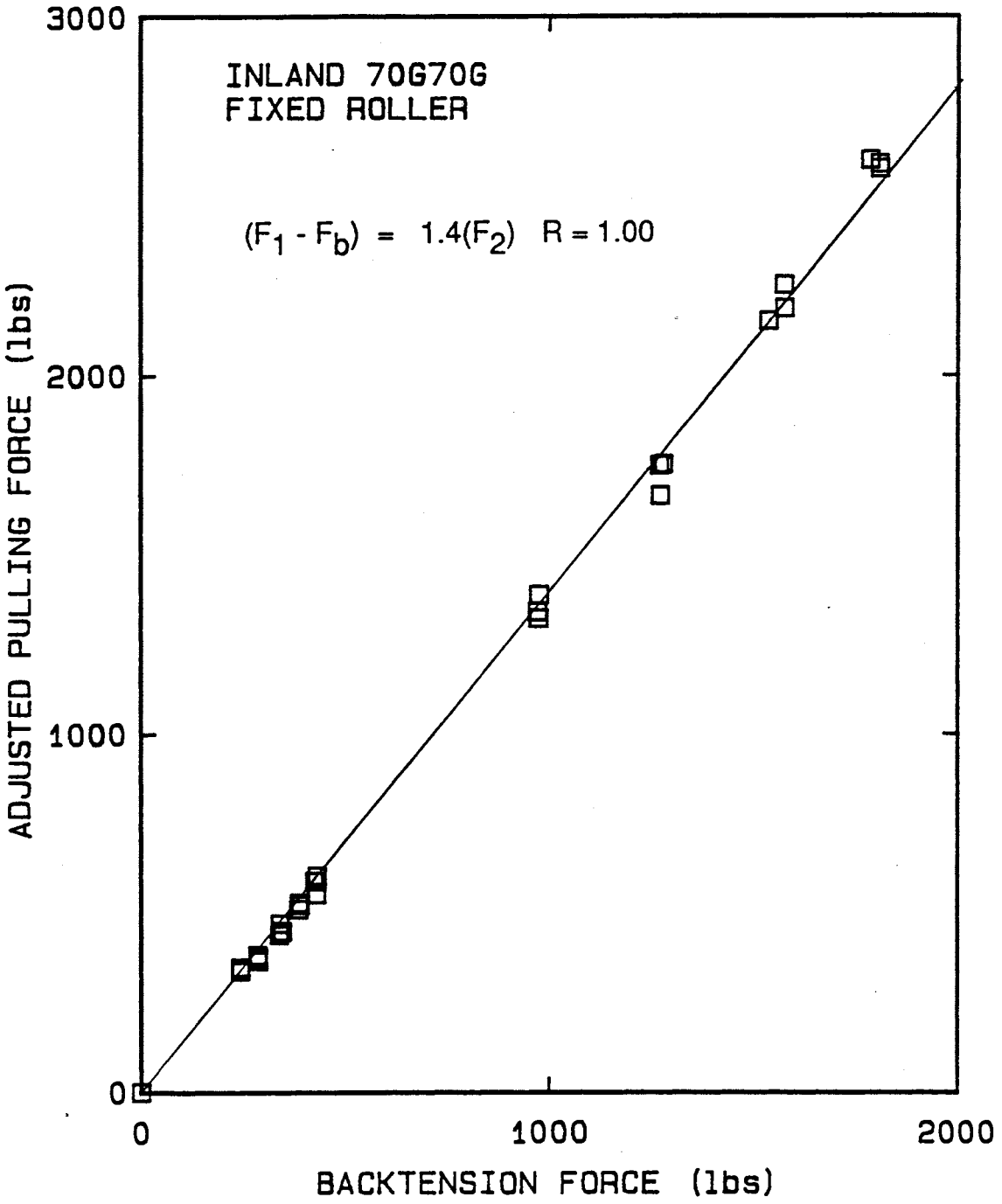

Figure 58 A linear fit between the adjusted pulling force (F_1-F_b) and the back tension force F_2, that has been constrained to go through the zero point (Material: Inland 70G/70G)

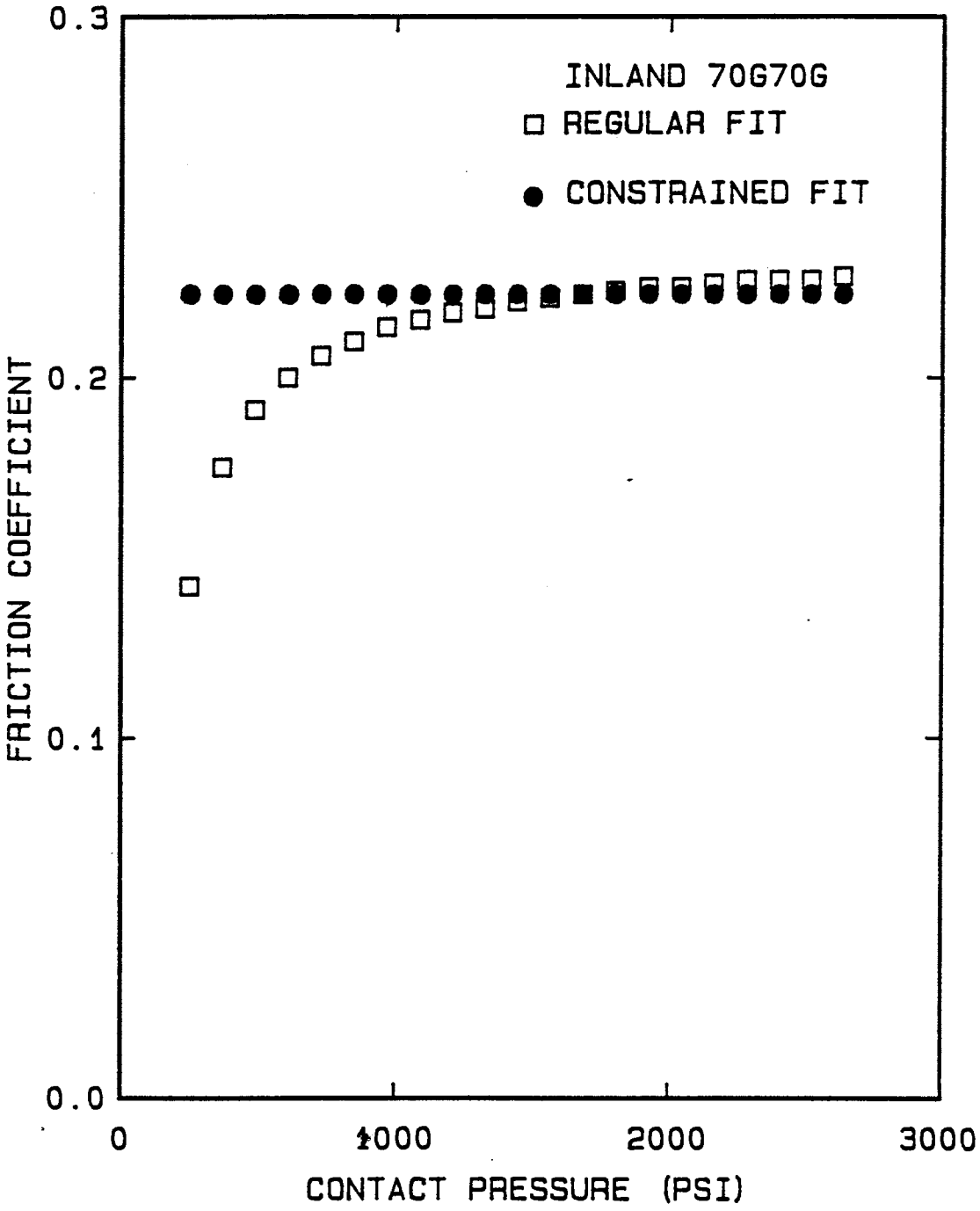

Figure 59 A comparison of the behavior of μ with contact pressure for cases of constrained and unconstrained linear fits between the adjusted pulling force (F_1-F_b) and the backtension force F_2 (Material: Inland 70G/70G)

value of μ for the electrogalvanized coating material tested is 0.223.

One of the limitations of this analysis (discussed in Section 2.4.3), is the necessity for the linear function between the adjusted pulling force (F_1-F_b) and the back-tension force F_2 to have a zero intercept value. A zero value for the intercept is necessary, though not sufficient, to keep Coulombic friction valid. Data measured experimentally do not give a zero intercept value for this function. Therefore for all three coatings listed in Table 5, linear functions obtained between (F_1-F_b) and F_2 will be constrained to have a zero intercept, before analyzing data under the Coulombic friction assumption. With the use of this procedure, the frictional behavior of the three coatings, Inland 70G70G (electrogalvanized zinc), Stelco 60HD (hot dip zinc), and Inland 60N40N (hot dip galvannealed) are compared.

5.4.2 Evaluation of Texture and Crystal Structure Effects on Friction in Coated Sheet Steels

In order to evaluate the effects of coating texture on friction, strips of coated sheet steels with an

electrogalvanized zinc coating (Inland 70G70G) or a hot dip zinc coating (Stelco 60HD) were subjected to the bending under tension type strip drawing test. Inland 70G70G had a Zn{10$\bar{1}$3} texture, parallel to the coating surface. Stelco 60HD had a strong basal plane texture. Texture changes were monitored as a function of the contact pressure in portions of the strip that saw the combined effects of stretching and a normal contact pressure. The deviation parameters of the Zn{10$\bar{1}$3} peak are plotted as a function of average contact pressure in Figures 60 and 61 for data obtained on Inland 70G70G. Both plots show a significant amount of scatter. Δ{10$\bar{1}$3} shows a trend towards randomness with increasing contact pressure in Figure 60. The observed change in deviation parameter with pressure indicates plastic flow and rotation of crystals. Texture changes were also measured on portions of the test strips that were subjected only to stretching (Figure 61). In these strips, deviation parameters of Zn{10$\bar{1}$3} and Zn{0002} were all positive, but showed considerable scatter in the values. The scatter can result from an initial scatter in texture on as-received Inland 70G70G sheets. Δ{10$\bar{1}$3} showed higher positive values as compared to Δ{0002}. Thus, while there is some preferred texture of Zn{10$\bar{1}$3} planes parallel to the surface, the extent of such texture

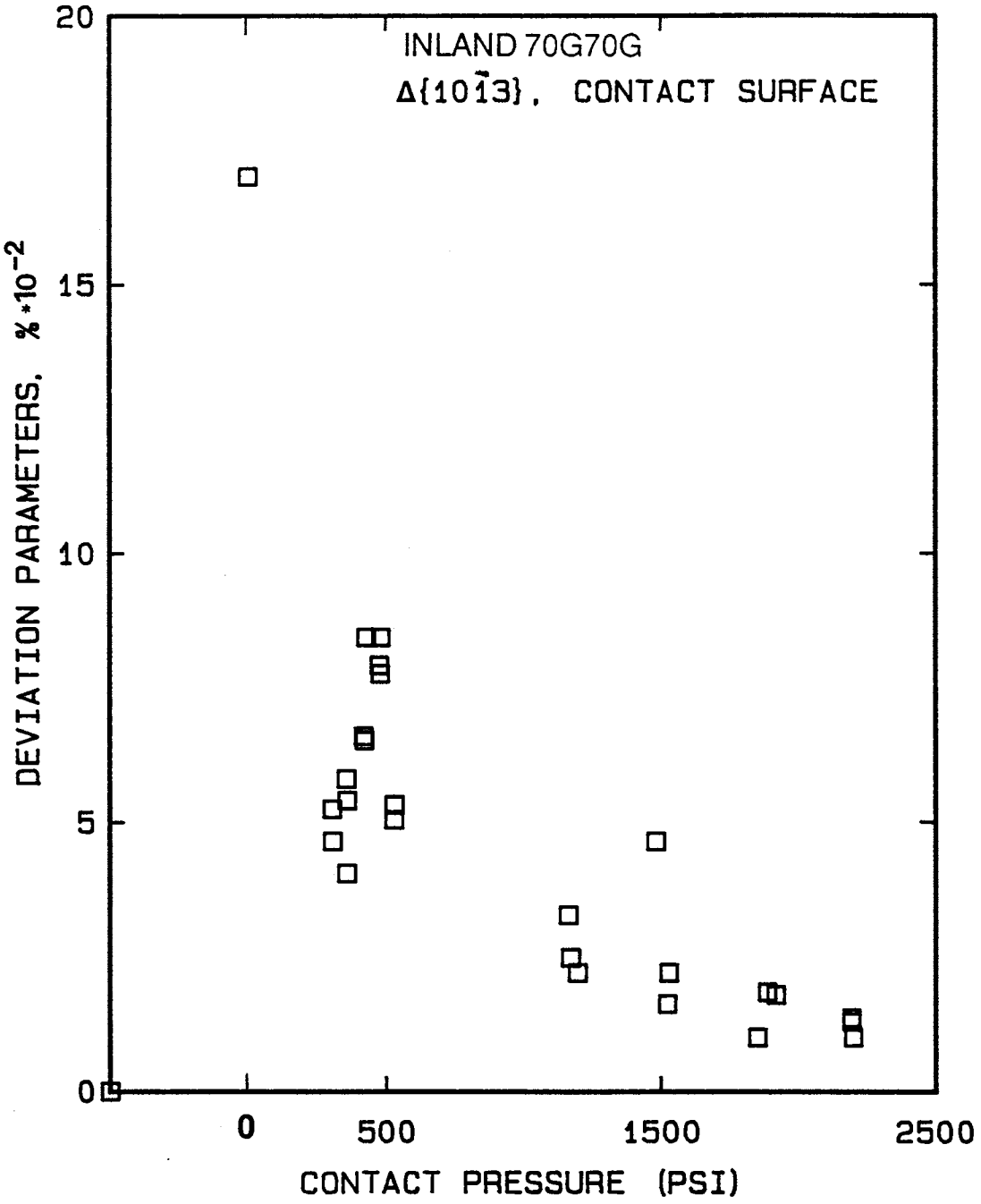

Figure 60 Deviation parameters of Zn{10$\bar{1}$3} peak plotted as a function of contact pressure in friction test, for an area of the strip subjected to contact with the roller (Material Inland 70G/70G)

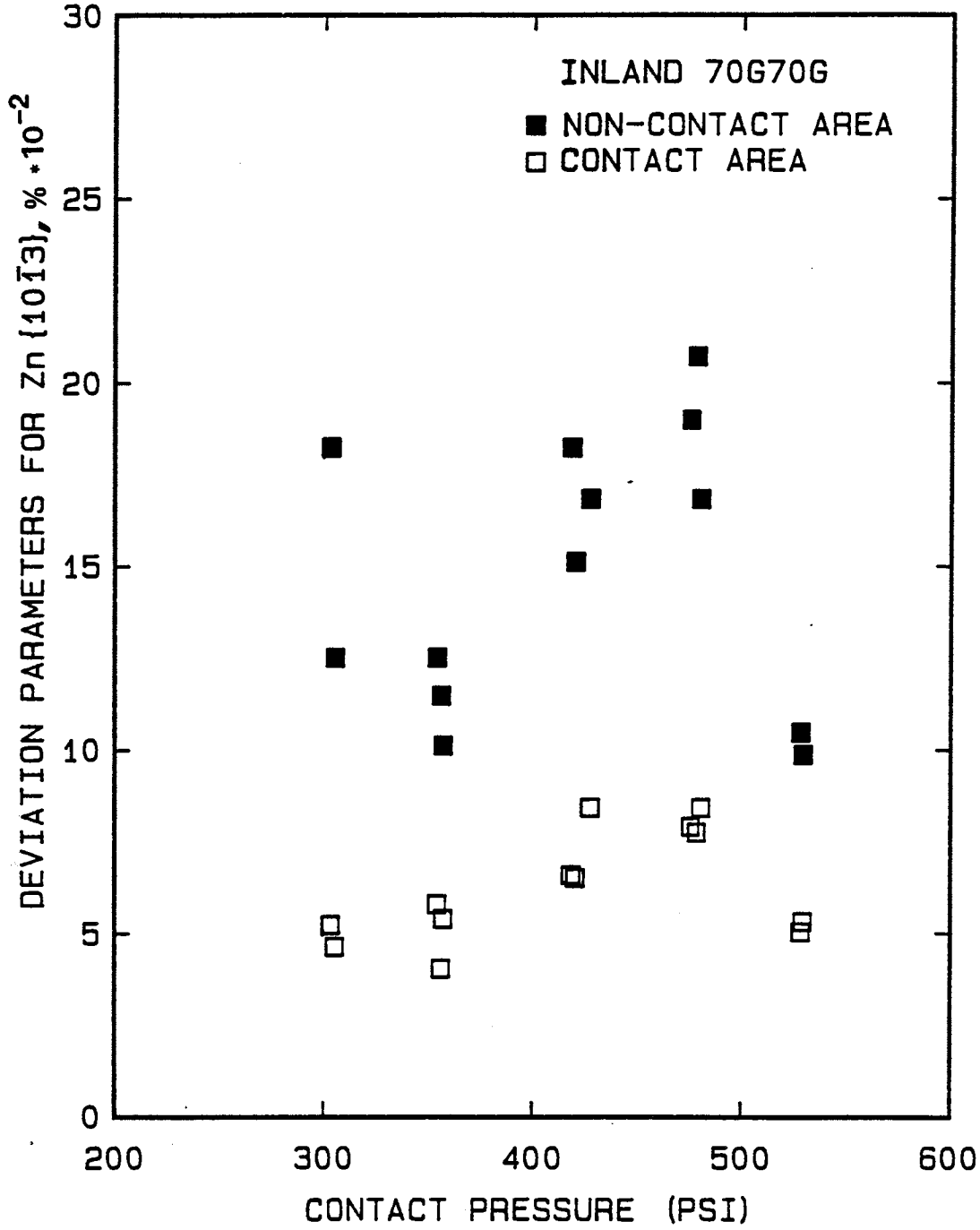

Figure 61 Deviation parameters of Zn{10$\bar{1}$3} peak plotted as a function of contact pressure in friction test, for areas of strip that were not in contact with roller, superimposed on the deviation parameter values for areas that were in contact (Material: Inland 70G/70G)

seems to vary significantly. For the purpose of this experiment, the critical factor is whether the basal planes are parallel to the surface. In Inland 70G70G, even though Zn{0002} shows positive deviation from randomness, the extent of basal plane texture is significantly less than Stelco 60HD (hot dip zinc coating), where the only peak observed in the X-ray diffraction pattern is the basal plane (Zn{0002}) peak, as shown in Figures 41 and 42. The hot dip coating showed the same strong basal plane texture before and after the friction test in the regions that saw contact pressure and stretching. Figure 62 shows X-ray diffraction pattern obtained on a Stelco 60HD coating surface, after it was subjected to a contact pressure of 513 psi. No variation in surface texture is seen when compared to the pattern obtained on the as-received coating, shown in Figure 42. In contrast, Figure 63 which presents the X-ray diffraction pattern obtained on an Inland 70G70G surface, after it was subjected to a similar contact pressure (528 psi) shows evidence for plastic flow and rotation of crystals (Refer to Figure 41 for the Inland 70G70G as-received coating X-ray diffraction pattern). The lack of surface texture change in Stelco 60HD does not necessarily imply lack of plastic flow. Shear stresses generated at the coating-roller interface in the friction

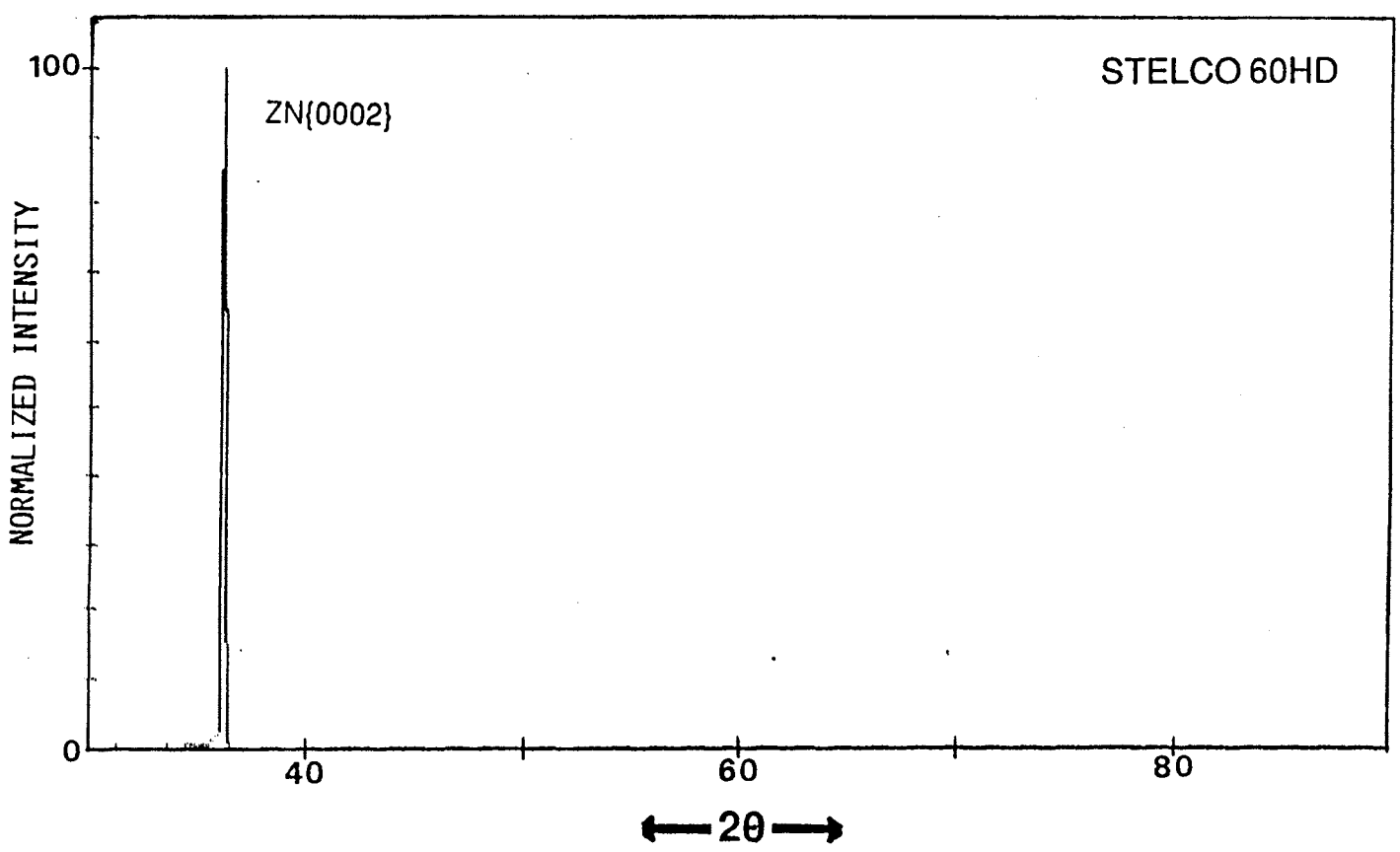

Figure 62 X-Ray diffraction pattern obtained from a Stelco 60HD hot dip zinc coating subjected to a contact pressure of 513 psi in the friction test (i.e., from an area of strip subjected to contact with roller)

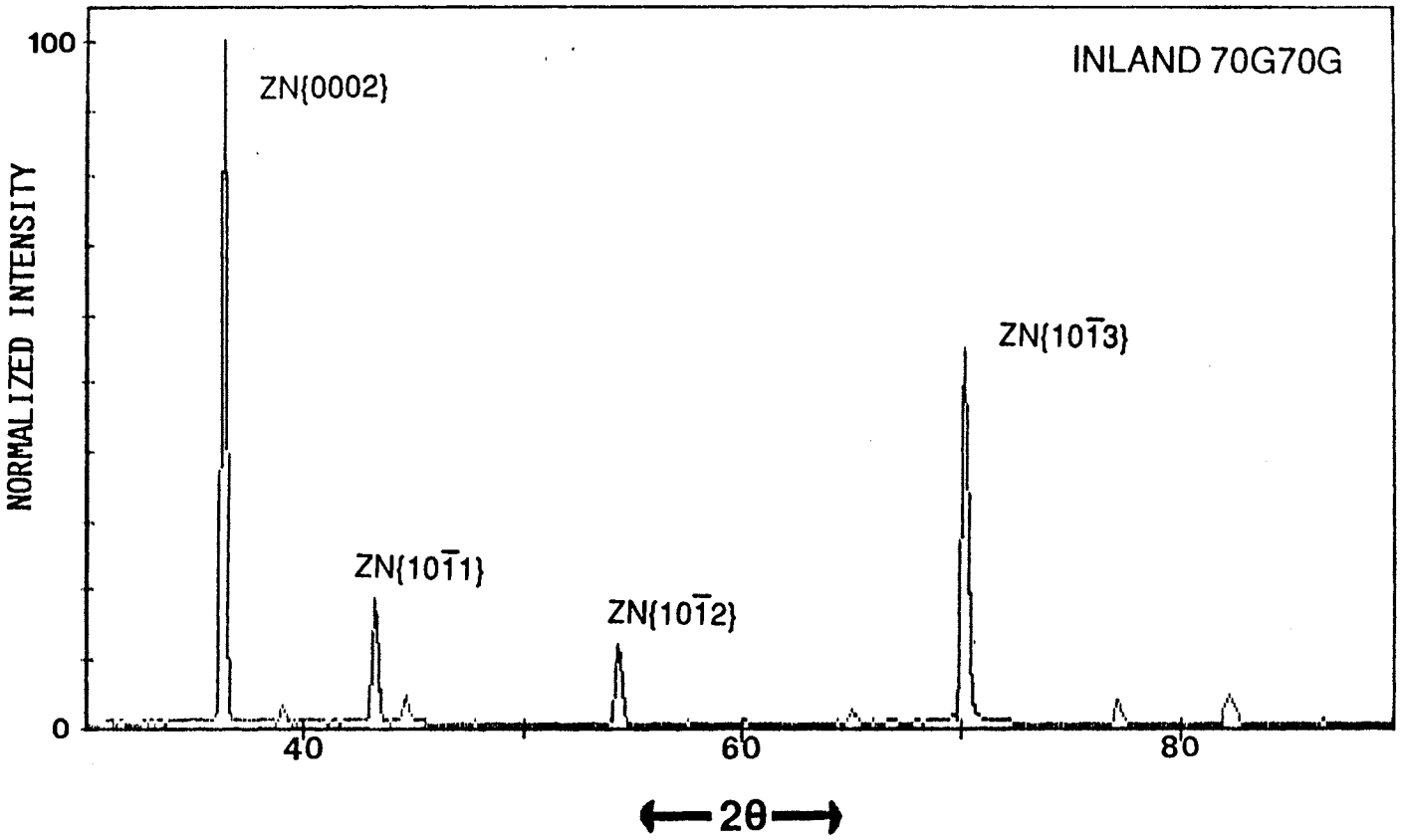

Figure 63 X-Ray diffraction pattern obtained from an Inland 70G70G electrogalvanzied zinc coating subjected to a contact pressure of 528 psi in the friction test (i.e., from an area of strip subjected to contact with roller)

tests, will promote plastic flow in the basal slip planes which are parallel to the coating surface in this coating. However the type and extent of such plastic flow does not appear to influence the X-ray diffraction pattern in Figure 62. Both coatings were tested under the same conditions of sliding speed and lubrication. From subsequent microscopic observations of the contact surface which showed non-contact zones surrounded by contact-zones, the lubrication appeared to be in the mixed regime for both coatings, i.e., the applied normal load was shared by asperities on the coating surface as well as the lubricant trapped between them.

Application of Coulombic friction law to the data generated in the friction test, gave values of 0.192 and 0.154 for μ of Inland 70G70G and Stelco 60HD respectively. The analysis was used to interpret data generated in a contact pressure range between 300 and 600 psi. The electrogalvanized coatings have a higher coefficient of friction than the hot-dip coating. Since the hot dip coatings have their basal slip planes parallel to the surface, shearing on these surfaces is expected to occur at lower applied shear stresses. Therefore, friction is expected to be lower for this orientation compared to the

non-basal texture in the electrogalvanized coating. From the point of view of initial texture in coatings, a basal plane texture parallel to coating surface is desirable for lower friction.

Steel sheets with a galvannealed coating (Inland 60N40N) were also subjected to friction tests. Galvannealed coatings have poor powdering resistance during forming and the powdering is a function of the alloy phase composition of the coating (37). Formation of intermetallic phases like δ and ζ, whose crystallographic structures are given in Table 2, result in brittle behavior of the coatings. The intermetallic phases have a greater tendency to fracture than flow. Under a combined stress state of pressure and shear, the asperities on the coating will fracture. Limited plastic flow occurs and as a result welding and adhesion do not develop at the metallic junctions (44). Brittle alloy coatings should therefore have low true areas of contact and correspondingly lower nominal shear stresses for junction breakage at tool-coating interface. These coatings therefore should have a lower friction coefficient compared to ductile coatings, as illustrated in Figure 19. Analysis of data under a Coulombic friction assumption gave a μ value of

0.171 for the galvannealed coating. The data was generated in the contact pressure range between 1000 and 2400 psi. A higher pressure range was chosen for the harder alloy coating in order to induce coating deformation at the surface and study it's behavior. It is important to note that the as-received galvannealed coating surface had a high percentage of temper-rolled area. In order to induce deformation to the level of freshly observable contact zones between the coating and the roller, over the temper rolled area, higher contact pressures were required. This becomes an important consideration in the contact area measurements discussed in the next section.

For comparison, the electrogalvanized coating (Inland 70G70G) was also subjected to friction tests in the high pressure range. Coulombic friction applied to the data generated at the higher pressures alone gave a μ value of 0.229 for the Inland 70G70G coating. Coulombic friction applied to data generated at the low pressures gave a μ value of 0.192, as reported earlier. With the assumption that Coulombic friction holds over the entire test pressure range, i.e., 300-2400 psi, a μ value of 0.223 was obtained as shown in Figure 59. In either case, the electrogalvanized coating has a higher μ compared to the

galvannealed coating, which supports the hypothesis of lack of welding and adhesion in the metallic junctions formed at the coating-roller interface.

Thus material factors unfavorable for plastic flow in stretching operations, namely basal plane textures and brittle alloys, prove to be beneficial in terms of lowering the friction coefficients of coated sheet steels. Coatings design will have to strike at an optimal compromise between superior flow in the coatings with better substrate coverage and lower surface ductility with lower friction coefficients, in order to arrive at a coating with good formability characteristics.

5.4.3 Analysis of Contact Surfaces on Coated Sheet Steels Subjected to the Friction Test

The above evaluation of friction on coated sheet steels employed the Coulombic friction assumption in the entire pressure range over which the materials were tested (approximately 300-2400 psi). However this approach has several limitations as pointed out in Section 2.4.3. One of the primary limitations of this analysis, is the non-validity of variations in μ with contact pressure. Such variations were however predicted by the analysis,

contradicting the assumptions of Coulombic friction. The limitations led to an exploration of new theories in friction. Wanheim and Bay's model (47) for metallic friction is able to predict, more closely, the experimental behavior of frictional shear stress as a function of normal pressure, over a wide range of contact pressures. In this model, the behavior of the true area of contact with contact pressure is critical, and determines the behavior of the frictional stress as a function of the contact pressure. It was therefore decided to evaluate true area of contact on coated sheet steels at different contact pressures i.e., different back-tension levels (F_2) in a bending under tension type strip drawing test. The measurements were done on all three coated sheet steels subjected to the friction test (Table 5), and involved extensive SEM studies followed by quantitative metallography i.e., point counting to determine the percentage true area of contact. A complete analysis was done for the electrogalvanized coating Inland 70G70G, and the hot dip zinc coating Stelco 60HD, i.e., true area of contact was measured over most of the pressure range between 300 and 2000 psi. For the galvannealed coating, friction testing and true contact area measurements were performed only at the higher contact pressure values, for

reasons stated in the previous section.

The results of the contact area measurements are summarized in Figures 64-66. Figures 64-66 show the surface morphologies of the three coatings after contact with the roller, in a fixed roller configuration. All three coatings exhibit both contact and non-contact zones, as illustrated in the micrographs. Figure 64, shows the surface of the electrogalvanized coating, after it was subjected to a contact pressure of 1166 psi. As shown in this figure, the as-received crystal morphology of the electrogalvanized coating is unaffected in the non-contact zone, while an adjacent contact zone on the coating is flattened. There are very clear groove marks seen on the contact zone in Figure 64b. The presence of these marks suggest that plowing occurred during sliding. Plowing could be a result of both tool surface roughness and coating debris buildup on the tool surface. Plowing contributes significantly towards increasing friction between sliding surfaces, especially when both surfaces are rough. In the present work plowing will contribute towards increasing the forward pulling force in the bending under tension type strip drawing test. On the electrogalvanized zinc coating surface, no evidence for cracking in the

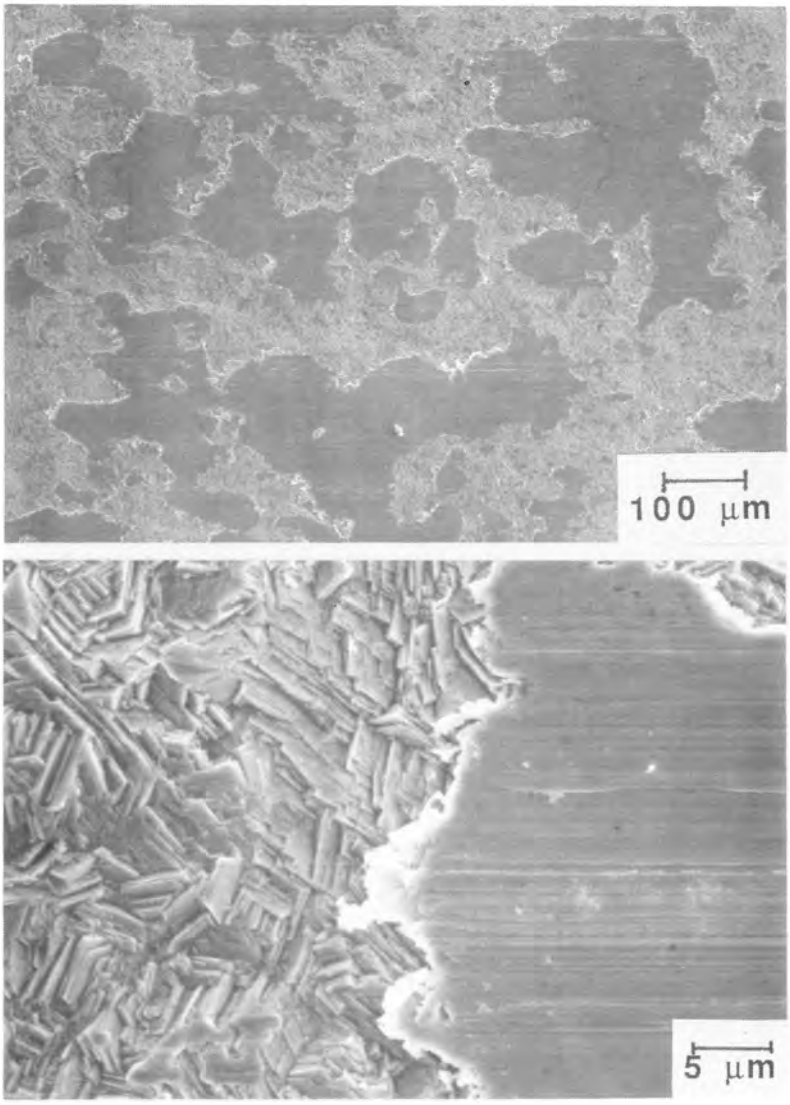

Figure 64 Surface morphology of an electrogalvanized zinc coating (Inland 70G/70G) after contact with the roller in a bending under tension type strip drawing test. Darker regions in the micrographs are contact zones. Sliding direction is parallel to the grooves in the contact zone

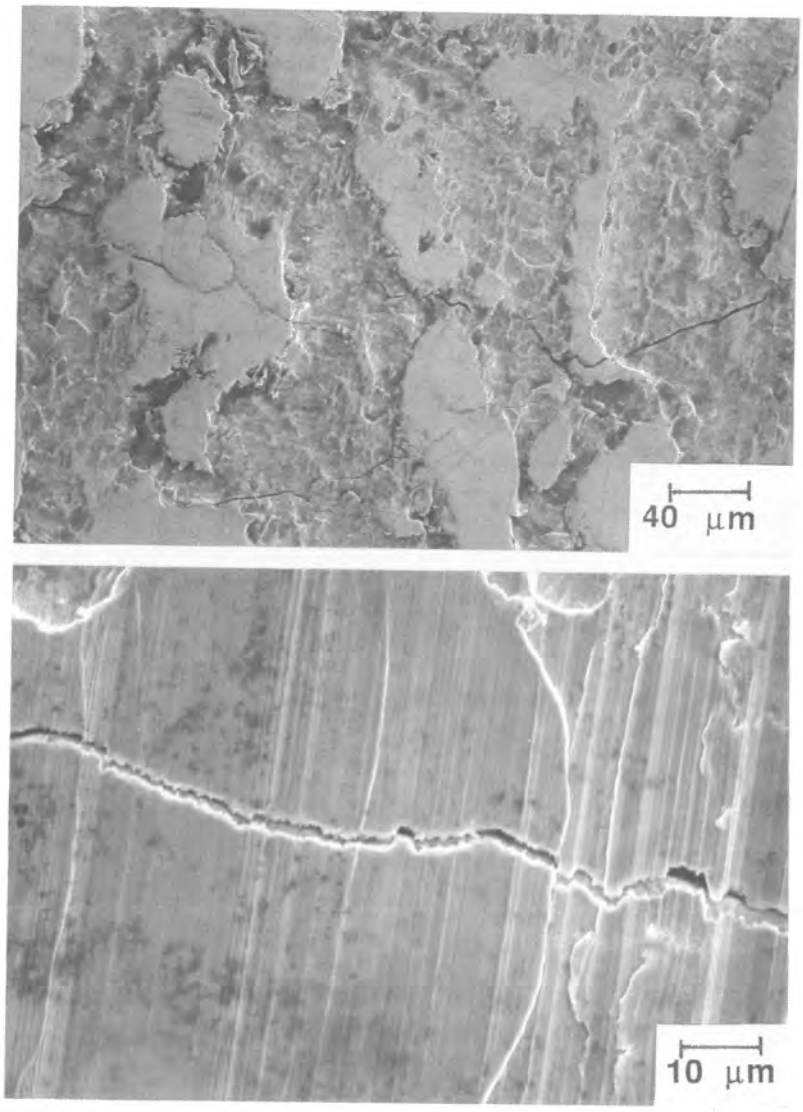

Figure 65 Surface morphology of hot dip zinc coating (Stelco 60HD) after contact with the roller in a bending under tension type strip drawing test. Sliding direction is parallel to the grooves in the contact zone

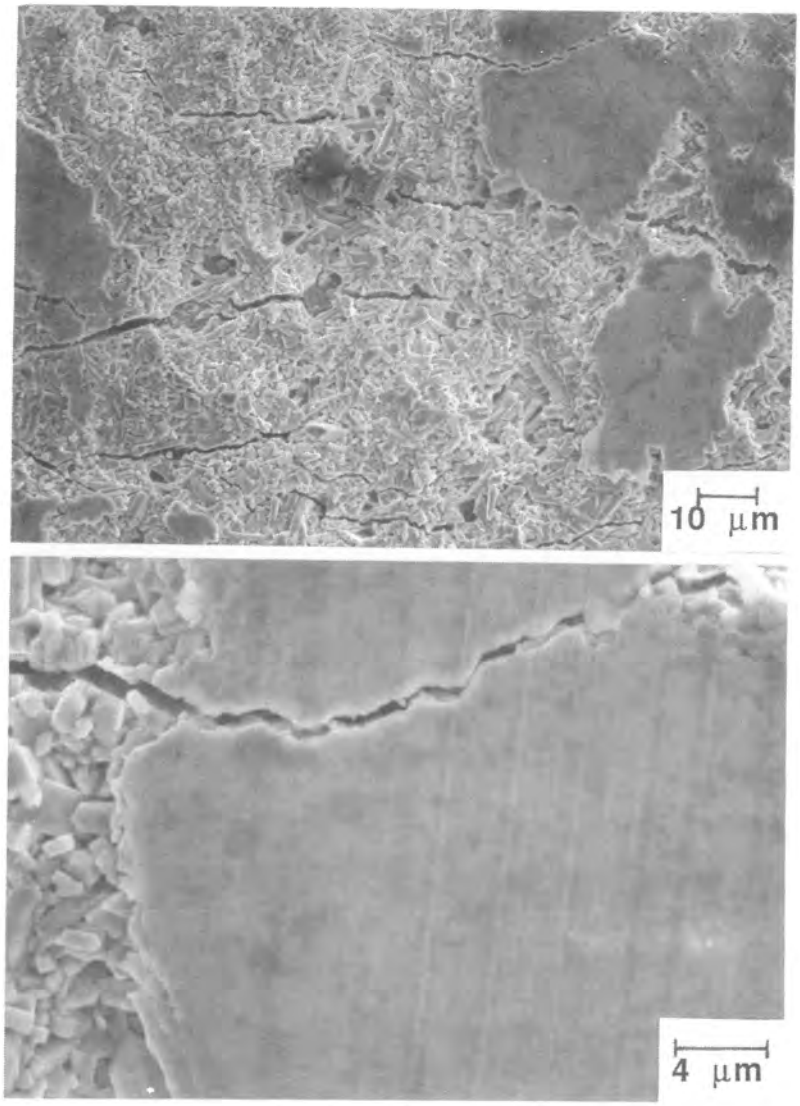

Figure 66 Surface morphology of Galvannealed coating (Inland 60N40N) after contact with the roller in a bending under tension type strip drawing test. Sliding direction is parallel to the grooves in the contact zone

coating is found. Figure 65, shows the contact surface on Stelco 60HD, hot dip zinc coating. Micrographs in Figure 65 show the presence of several cracks in the coating. The cracks traverse through both the non-contact zone and the contact zone (Figure 65b). These cracks are probably a result of the sheet unbending strains imposed on the coating, after the section of coated sheet steel had passed over the roller. Since the hot dip zinc coatings have a strong basal plane texture, cracking was promoted as a mode of strain accommodation. Once again, grooves indicating plowing are seen in the contact zone in Figure 65b. Figure 66 shows the contact surface on a galvannealed coating, which was subjected to a contact pressure of 1450 psi. Some of the key features in Figure 66 are, presence of a number of parallel cracks traversing both the contact and the non-contact zones, an intact alloy crystal morphology in the non-contact zones, and faint grooves indicating plowing in the contact zones. The cracks are a result of both the sheet unbending strains and the brittle intermetallic phases present in these coatings.

The series of micrographs in Figures 64-66 clearly show that the true areas of contact are lower than the nominal areas of contact on surfaces of coatings subjected

to the friction test. The micrographs also emphasize the necessity for microstructural studies on deformed coating surfaces, in order to understand fundamental mechanisms controlling friction.

Now consider the factors that determine the true areas of contact on a coating material. Figure 67, plots the true contact area ratio a, from point count measurements, as a function of the contact pressure, for the three coatings subjected to friction tests. For both pure zinc coatings, Inland 70G70G and Stelco 60HD, measured values are similar at a given pressure and increase with the average contact pressure. For the alloy coating, Inland 60N40N, the measured values are lower compared to pure zinc coatings, for the same contact pressures.

The behavior of a, for pure zinc coatings, follows the predictions of Wanheim and Bay (Figure 11). At lower pressures, a is a linear function of the contact pressure. In this region, Coulombic friction holds. However, at contact pressures greater than 500 psi, a enters a transition zone between Coulombic and constant friction regimes. A contact pressure of 500 psi corresponds to a p/2k ratio of 0.05, since the measured tensile yield

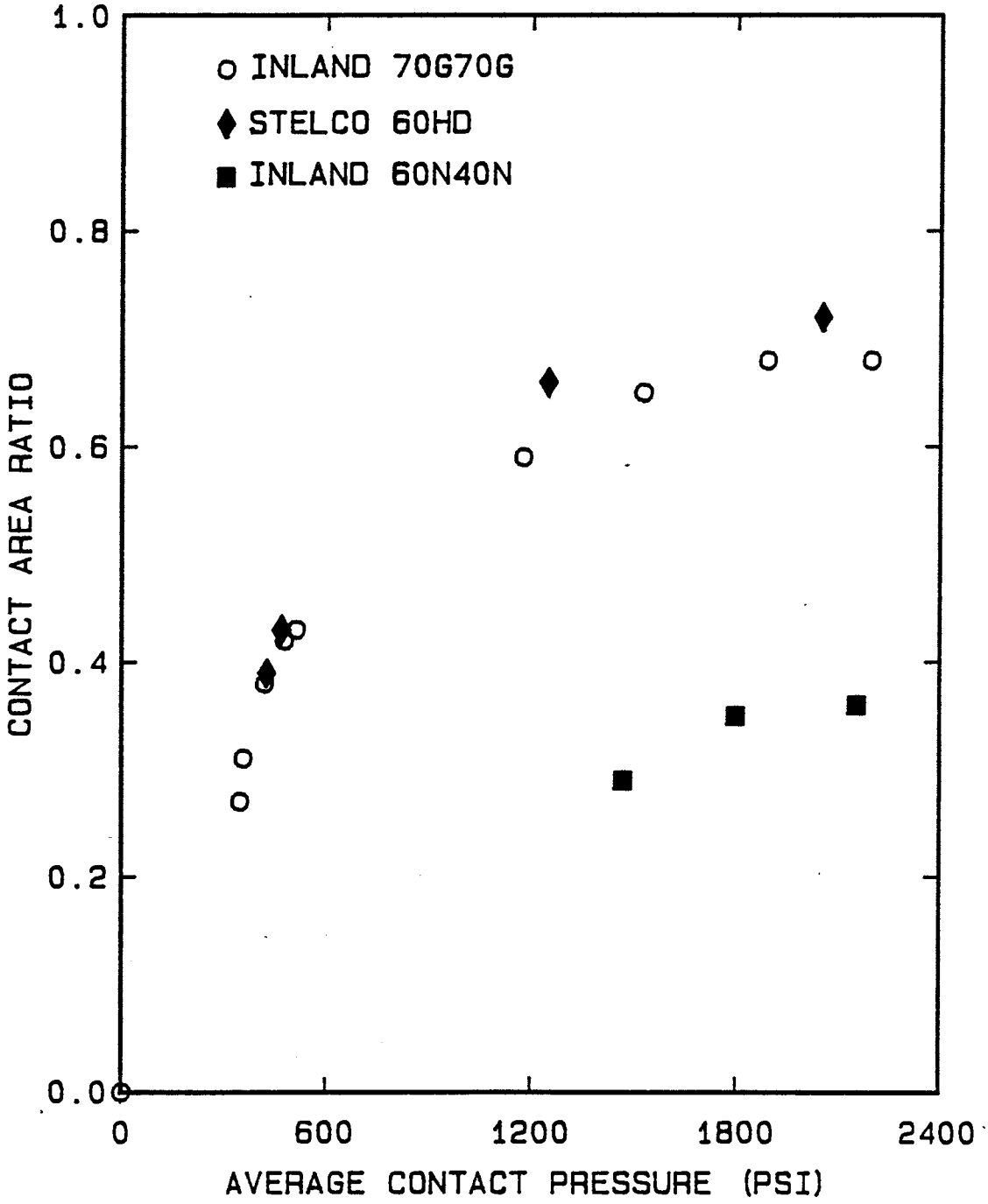

Figure 67 True contact area ratios on coated sheet steel surfaces plotted as a function of average contact pressure in a bending under tension type strip drawing test

strength of pure zinc at 300°k is approximately 9000 psi (82). 2k refers to tensile yield strength of the material, when Tresca yield criterion is used (50). If von Mises yield criterion is used the same value of measured tensile yield strength is equal to $\sqrt{3}$ k. Thus the value of k will vary depending on the yield criterion used. In the current discussion, the contact pressure generated in the friction test is normalized with respect to a measured yield strength value which is independent of the type of yield criterion employed. In Figure 67, for pure zinc coatings a transition from Coulombic friction behavior starts at a normalized contact pressure of 0.05, which is far less than the value of 1.3 for dry sliding reported by Wanheim and Bay (Refer to Figure 12). One of the possible explanations for this difference is the fact that the average contact pressures generated are far less than the peak values that can occur at the entry and exit points of contact between the sheet and the roller. At average contact pressures greater than 2000 psi, the constant friction model seems to apply. Here α reaches a saturation value of 0.7 for pure zinc coatings.

In Figure 67, similar values of true contact areas are obtained on the electrogalvanized and hot dip zinc

coatings, even though Coulombic friction analysis showed that they have markedly different coefficients of friction. Also, Figure 67 suggests that data collected at contact pressures below 500 psi can be used to determine the Coulombic coefficient of friction. Assuming Coulombic friction for data generated below a contact pressure of 500 psi gave μ values of 0.192 for the electrogalvanized coating and 0.154 for the hot dip coating, respectively. This is in contrast to a μ value of 0.223 for Inland 70G70G, obtained by assuming Coulombic friction over the entire pressure range (300-2400 psi). Assuming Coulombic friction to hold over a wider range of pressures thus results in a 20% difference in calculated values of μ for the electrogalvanized coating.

The linear portion of the α vs. contact pressure function has a slope of $8.85*10^{-4}$ / psi in Figure 67. Multiplying this slope by the flow stress of zinc in pure shear, k, (half the tensile yield strength)a value for the ratio of μ/f is obtained. Since values of μ are known, values for f (adhesive bond strength factor), can be calculated for the electrogalvanized and hot dip coatings, assuming k is the same for both these coating material (82). The electrogalvanized coating (Inland 70G70G) with a

μ value of 0.187, has a corresponding f value of 0.047. The hot dip coating (Stelco 60HD) with a μ value of 0.155 has a corresponding f value of 0.039. Since the frictional stress is given by $\tau = f\alpha k$, hot dip zinc coatings with a lower adhesive bond strength factor f, experience lower friction shear stresses at any given contact pressure.

Galvannealed coatings have lower true areas of contact compared to pure zinc coatings, as shown in Figure 69. Due to limited ductility in these coatings, adhesion between the asperities on the coating and the roller is expected to be weak resulting in lower values of f. This suggests that the normalized nominal friction stresses, τ/k, will be lower on these coatings. Galvannealed coating surfaces had a high percentage of temper rolled area in the as-received condition. The coatings also exhibited a significantly higher hardness compared to pure zinc coatings (82). Therefore, in order to induce any measurable amount of deformation and associated coating-roller contact zones on the surface of these coatings, higher pressures were required. Friction testing of the galvannealed coatings were restricted to higher pressures for these reasons. As a result a value for f is not available for galvannealed coatings.

Figure 67 shows that the two factors influencing true area of contact are the applied contact pressure and the material strength. This is true for a given set of lubrication conditions and sliding speed. The presence of the lubricant physically prevents the true contact area ratio from reaching a value of unity at high contact pressures, as would be the case in dry sliding.

5.4.4 Summary of Understanding Gained from Friction Analyses on Coated Sheet Steels.

Friction analyses on coated sheet steel present the following picture:

In a wide range of normalized contact pressures, coating materials exhibit different frictional behaviors. In the low contact pressure range, materials obey Coulombic friction law, where the frictional shear stress is a constant fraction of the applied contact pressure. The fraction is the coefficient of Coulombic friction μ. The true area of contact established between the tool and the workpiece varies linearly with pressure in this regime. Frictional shear stress is given as $\tau = f\alpha k$, where f is the

adhesive bonding factor (83), α the fractional area of true contact and k the material flow stress in pure shear. Since α is a linear function of contact pressure, τ also varies linearly with the contact pressure.

At high contact pressures materials follow the constant frictional stress behavior. Here the frictional stress is a constant fraction "f" of the product of material flow stress in pure shear, k, and the saturation value of the fractional area of true contact, α, i.e., $\tau = f(\alpha k)$. The product within the parentheses is a constant in this high pressure region. For dry sliding conditions, α reaches a value of 1 and $\tau = f(k)$.

In an intermediate pressure range, between the Coulombic and the constant friction regimes, α and therefore τ vary non-linearly with contact pressure. A smooth transition occurs here, between the Coulombic and constant friction regions.

Since frictional properties are directly related to the material flow properties, coating texture and crystal structure become important parameters controlling friction on coated sheet steels. For ductile zinc coatings, a basal

plane texture parallel to the surface, is favorable for lower friction coefficients. If the basal planes of the surface crystals are aligned parallel to the surface, slip, becomes easier at lower applied shear stresses. Favorable texture for shear manifests as a reduced interface adhesive bond strength factor in Wanheim and Bay model (47). Brittle Zn-alloy coatings also exhibit lower friction coefficients compared to non-basal plane textured pure zinc coatings. This is because the crystal structure and the associated material strength determine true areas of contact under a given contact pressure. Coatings with higher material strength, exhibit lower true areas of contact and therefore experience lower nominal frictional stresses. Also, with intermetallic phases, plastic flow is limited, and welding and adhesion at the metallic junctions will not develop, leading to lower coefficients of friction.

In dry sliding, coating material strength appears to be the primary factor controlling the true area of contact and therefore the friction stress. However, for lubricated sliding, coating roughness and lubrication play a role in determining the value of f and α. The role of roughness is closely related with the effective supply of lubricant at

the interface. Roughness may also control the amount of entrapped lubricant. Entrapped lubricant provides additional constraints to metal flow, thereby preventing α from reaching higher values. The entrapped lubricant bears a fraction of the applied load, which also implies a reduced value of α for the same applied load. Besides roughness, efficiency of the lubricant is another factor that may control f and α. An efficient lubricant can prevent the formation of strong adhesive metal junctions, thereby reducing the value of f. Entrapped lubricant properties may control the extent to which the value of is lowered.

Values of α obtained for different coated sheet steels in a bending under tension type test clearly illustrate the influence of material properties on friction. However, it is necessary to compare and contrast these values with those obtained on a drawbead simulator test, which is an established test in the industry for characterization of frictional properties on coated and uncoated sheet steels.

5.4.5 A Comparison of Friction Results Obtained from the Drawbead Simulator Test and the Bending Under Tension Test

Drawbead simulator test (84) is being widely used in automotive industries to characterize frictional properties of various coatings and evaluate the efficiency of different lubricants used in sheet metal forming operations. Drawbeads on a blankholder are used in a sheet metal forming operation to control the flow of metal into the die (84). The sheet experiences both frictional resistance and bending deformation. In order to independently determine the force required to overcome friction and the force required to bend the sheet over the rollers, a drawbead simulator test was designed (84). The design and development of the test is described in reference 84. In this test, a drawing force F and a clamping force C are measured. When the drawbeads in the test are free rollers, the drawing force F (F_2) relates to the force required for bending the sheet. If the drawbeads in the test are fixed, the drawing force F (F_1) measures the force required to overcome friction in addition to the force required to bend the sheet (84). The difference ($F_1 - F_2$) gives the drawing force required

to overcome friction. The normal force that develops between the sheet steel and the drawbead is measured as a clamping force C (force measured in the blankholder clamping direction). From a measurement of C, a distributed force normal to the semi-cylindrical bead surface can be calculated assuming uniform contact pressure over the entire contact surface. The uniformly distributed normal force, N, is given by (84)

$$N = (\pi C)/2 \qquad [14]$$

Assuming Coulombic friction to hold, a coefficient of friction can be calculated as follows

$$\mu = \tau/p = [(F_1 - F_2)/A]/[N/A] = (F_1 - F_2)/N \qquad [15]$$

A is the true area of contact between the sheet steel and the drawbead. A is equal to $(\pi w D)$, where D is the diameter of the drawbead and w is the width of the sheet. The average contact pressure, p, is equal to N/A. This value of p is comparable to the average contact pressure calculated in the bending under tension test. N is calculated from Equation 14. Since the sheet going through a drawbead is loaded on both sides, the total clamping

force is given by 2C. Therefore, N becomes equal to C. The coefficient of friction is now given by

$$\mu = (F_1 - F_2)/\pi C \qquad [16]$$

The electrogalvanized and the galvannealed sheet steels, Inland 70G70G and Inland 60N40N respectively, were subjected to the drawbead simulator test at the Inland Steel Company research center in East Chicago, Indiana (40). The results obtained are summarized in Table 12. Table 12 lists the measured values of forces and the calculated values of μ for the two coated sheet steels, along with the average contact pressure, p, that was generated during the drawbead simulator test. The contact pressures generated are higher than 500 psi which is the limiting contact pressure upto which Coulombic friction is valid for pure zinc coatings (Refer to Figure 67). Values of μ for the two coated sheet steels calculated from the bending under tension test, assuming Coulombic friction to hold in the high pressure range, are also listed in Table 12. Both tests indicate similar variations in values of μ as a function of the coating material. The galvannealed sheet steel exhibits a lower coefficient of friction compared to the electrogalvanized sheet steel. The bending

Table 12: Summary of results obtained from a Drawbead Simulator Test

(Diameter of Drawbead, D = 0.375")

(Width of coated sheet steel = 2")

Material	F_1 (lbs)	F_2 (lbs)	C (lbs)	μ	p (psi)	μ (from bending under tension test)
Inland 70G70G	1279	718	1010	0.176	1347	0.229
Inland 60N40N	1271	817	1052	0.137	1403	0.171

F_1 - average drawing force (fixed drawbead)

F_2 - average drawing force (free roller)

C - average clamping force (fixed drawbead)

p - average contact pressure generated in the drawbead simulator test

under tension test gives a higher value for μ (approximately 30% higher in Table 12) compared to the drawbead test.

For the Inland 70G70G sheet steel, the bending under tension test gave a μ value of 0.192 at contact pressures less than 500 psi. This value is assumed correct since Coulombic friction was found to be valid in this low pressure region. The drawbead simulator test underestimates the μ value by assuming Coulombic friction to hold at higher pressures while the bending under tension test overestimates the value of μ for the same assumption.

It must be realized that μ is a system parameter, i.e., its value reflects on both the material properties and the imposed test conditions. For the same test conditions, it is worthwhile to compare trends or changes in the value of μ for different materials. However, comparing absolute values of μ obtained under different test conditions for different materials may give erroneous results. Evaluation of μ values must be done under conditions that simulate the applied stress state during the actual application.

6.0 CONCLUSIONS

1) Pure zinc coatings with a basal plane texture (i.e., basal planes aligned parallel to the coating surface in many coating crystals) tend to fracture upon the application of tensile strain in stretching operations without surface contact stresses. Therefore, a non-basal plane texture is preferred in pure zinc coatings for accommodation of strain by plastic flow.

2) Zinc-alloy coatings with limited ductility tend to fracture upon the application of tensile strain. Increasing amounts of strain are accommodated by coalescence and widening of microcracks in the coating.

3) For hot dip zinc coatings, besides texture, spangle sizes are an important consideration in flow and fracture behavior. Spangle boundaries are potential sites for crack nucleation. Large spangle sizes and basal plane texture promote wide coating cracks, exposing the steel substrate. This exposure results in enhanced galvanic corrosion of zinc in an unpainted condition.

4) The differences between a simple stretching operation and a friction test are the presence of a contact pressure perpendicular to the coating surface and frictional shear stresses at the interface. The frictional shear stress at the interface, i.e., the applied shear stress required to overcome friction, is lower in coatings with basal planes parallel to the sheet surface.

5) The limited plastic flow in zinc-alloy coatings prevents formation of strong welded metallic junctions at the coating-tool interface, since the asperities on the alloy coating surface fracture. As a result, shear stresses required to break these junctions are low. Correspondingly brittle zinc-alloy coatings have lower frictional stresses compared to ductile non-basal plane textured zinc coatings.

6) A modified model for metallic friction incorporating asperity deformation on surfaces was proposed by Wanheim and Bay. A key prediction in this model is the functional dependence of true area of contact on contact pressure. The experimentally measured true contact area on coating surfaces in this work followed the predicted trend in

Wanheim and Bay's model, supporting the applicability of this model to friction analyses on coated sheet steels.

7) Nominal friction shear stresses are directly proportional to the true areas of contact and a bonding factor in Wanheim and Bay's model. Pure zinc coatings with a basal plane texture have lower bonding factors and therefore lower nominal friction shear stresses. Zinc-alloy coatings with limited plastic flow have a low true area of contact at a given pressure compared to more ductile coatings, and therefore also have lower friction stresses.

8) Experimental determination of true contact area on pure zinc coatings as a function of contact pressure showed that Coulombic friction was valid upto a contact pressure of 500 psi for pure zinc coatings. Assuming Coulombic friction to hold over a wider range of pressures (300-2400 psi) resulted in a 15% difference in the reported values of the coefficient of friction μ.

9) Coating deformation and friction models developed in this work can be used to understand and design coatings with improved formability. One such design based on the

results of this work would be a two layer pure zinc coating with differing textures in the layers. The outer thin layer, of the order of few microns, should have a basal plane texture for reduced friction. The bulk of the coating should have a non-basal plane texture for accommodation of stretching strains by plastic flow. The feasibility of commercial production of these coatings and their deformation behavior, especially at the interface between the two layers, needs to be investigated in the future.

7.0 REFERENCES

1) G.J. Harvey and P.N. Richards, "Zinc Based Coatings for Corrosion Protection of Steel Sheet and Strip", Metals Forum, vol. 6, no. 4, 1984, pp. 234-247.

2) D.F. Baxter, "Developments in coated steels", Metal Progress, vol. 129, no. 6, 1986, pp. 31-35.

3) Corrosion Resistant Automotive Sheet Steels, ed. L. Allegra, ASM, Metals Park, Ohio, 1988.

4) M.G. Fontana, "Corrosion Engineering", McGraw-Hill Book Company, 1986, pp. 487-492.

5) H. Leidheiser Jr. and I. Suzuki, "Towards a More Corrosion Resistant Galvanized Steel", Corrosion, vol. 36, 1980, pp. 701-702.

6) M.R. Lambert and R.G. Hart, "Corrosion Resistance of 0-15% Ni-Zn Alloy Electroplated Coatings", SAE Technical paper No. 860266, 1986.

7) T. Adaniya, T. Hara, M. Sagiyama, T. Watanabe and T. Honma, "Corrosion Resistance of Zn-Fe Alloy Electroplated Steel", ASM Metals/Materials Tech. Series, No. 8512-022, 1985, pp. 1-10.

8) H.E. Townsend and A.R. Borzillo, "Twenty-year Atmospheric Corrosion Tests of Hot-Dip Coated Sheet Steel", Materials Performance, July 1987, pp. 37-41.

9) F.E. Goodwin, A.F. Skenazi and R.F. Lynch, "Corrosion Test Results and Application of Coil Coated Galfan", CIM Bulletin, vol. 80, no. 905, 1987, pp. 115-122.

10) "The Forming of Galvanized Sheet Steels", Guidelines for Automotive Applications, American Iron and Steel Institute.

11) N.M. Giallourakis, "Structure and Deformaton of Zinc Coated Sheet Steels", M.S. Thesis, NO. T-3441, Colorado School of Mines, Golden, Colorado, 1987.

12) D.J. Willis and J.S.H. Lake, "The Influence of the Interaction between Coating and the Sheet Steel Base on the Formability of Aluminium-Zinc Coated Steel",

Proc. of 15th. Bienn. Congr. of IDDRG, Dearborn, Michigan, May 16-18, 1988, pp. 31-41.

13) F. Hanna and N. Nassif, "Factors Affecting the Quality of Hot-dip Galvanized Steel Sheets", Surface Technology, vol. 21, 1984, pp. 27-37

14) J. Mackiowak and N.R. Short, "Metallurgy of Galvanized Coatings ", Int. Met. Revs., vol. 24, 1979, pp. 1-19.

15) J. Mackiowak and N.R. Short, "Effect of Chemical Potential of Zinc on Composition and Nature of Interaction Layers Formed during Reaction between Solid Iron and Zinc Vapor at 793 K", Metal Science, November 1977, pp. 517-522.

16) A.R. Borzillo and W.C. Hahn Jr., "Growth of the Inhibiting Aluminum-Rich Alloy Layer on Mild Steel during Galvanizing in Zinc that contains Aluminum", Transactions of the ASM, vol. 69, 1969, pp. 729-739.

17) D.I. Cameron, G.J. Harvey and M.K.Ormay, "The Spangle of Galvanized Iron", J. Austr. Inst.

Metals, vol. 10, 1965, pp. 255-264.

18) D.I. Cameron and G.J. Harvey, "Solidification and Spangle of Galvanized Coatings", 8th. Int. Conf. on Hot Dip Galv., London, 1967, pp. 86-97.

19) R.G. Hart, N.S. Berke and H.E. Townsend, "The Effects of Water Vapor on Solidification of Galvanized Coatings", Metall. Trans. B, vol. 15B, 1984, pp. 393-395.

20) R.F. Lynch, "Hot-Dip Galvanizing Alloys", J. of Metals, vol. 39, no.8, 1987, pp. 39-41.

21) J.H. Selverian, M.R. Notis and A.R. Marder, "The microstructure of 55 w/o Al-Zn-Si (Galvalume) Hot Dip Coatings", Surface Modifications and Coatings, ed. R. D. Sisson Jr., ASM, 1986, pp. 447-453.

22) H. Leidheiser, Jr. and I. Suzuki, "Cobalt and Nickel Cations as Corrosion Inhibiters for Galvanized Steel", J. Electrochem. Soc.: Electrochemical Science and Technology, vol. 128, no.2, 1981, pp. 242-249.

23) N.T. Ferguson, A. Tropeano, C. Raggio and L. Ulivieri, "Multizincrox - An Improved Multilayer Electrogalvanized Steel Sheet", Iron and Steel Engineer, June 1987, pp. 35-39.

24) D. Perry, A. Juissiaume and Y. Deleon, "Study of Damage Sustained by Precoated Sheet Steel during Deformation and Effect of This on Resistance to Corrosion", Addendum to Controlling Sheet Metal Forming Processes, Proc. of 15th. Bienn. Congr. of IDDRG, Dearborn, Michigan, May 16-18, 1988.

25) J.B. Vrable, "Effect of Forming Deformation on Corrosion Test Performance of Electroplated Zinc and Iron-Zinc Alloy Coatings for Automotive Sheet", SAE Technical Paper No. 862012, 1986.

26) J.Z. Gronostajski and M.S. Ghattas, "Influence of Forming of Coated Steel Sheets on the FLD and Corrosion Resistance", Proc. of the 15th. Bienn. Congr. of IDDRG, 1988, Dearborn, Michigan, May 16-18, 1988, pp. 49-54.

27) I. Aoki, T. Horita and T. Herai, "Formability and

Application of Galvanized Sheet Steels", Proc. of the 13th. Bienn. Congr. of the IDDRG, Melbourne, Australia, 1984, pp. 165-176.

28) D.J. Robbins, D.M. Smith and T.R. Roberts, "Corrosion Testing and Behavior of Zinc and Zinc Alloy Coated Autobody Sheet Steels", Corrosion-Resistant Automotive Sheet Steels, ed. L. Allegra, ASM, Metals Park, Ohio, 1988, pp. 1-14.

29) D.J. Mueleman, A.G. Denner, and F.L. Cheng, "The Effect of Zinc Coatings on the Formability of Automotive Sheet Steels", SAE Technical Paper No. 840370 1984.

30) C. Belleau and D.K. Kelly, "Quality, Formability and Productivity Considerations in Production Use of Galvanized Steels", SAE Technical Paper No. 850272, 1985.

31) I. Gupta, R.S. Cline, and R.S. Patil, "Effect of Iron-Zinc Alloy Layer on the Mechanical Properties and Formability of Hot Dip Galvanized Steels", SAE Technical Paper No. 840216, 1984.

32) R. Stevenson, "Formability of Galvanized Steels - Revisited", SAE Technical Paper No. 850276, 1985.

33) R. Stevenson, "Coating Effects in the Formability of Galvanized Steel", SAE International Meeting and Exposition, Detroit, Michigan, March 1-4, 1983.

34) J.Z. Gronostajski and W.J. Ali, "Analysis of Formability of Coated Steel Sheet at Complex Strain Paths", Proc. of the 15th Bienn. Congr. of IDDRG, Dearborn, Michigan, May 16-18, 1988, pp. 43-47.

35) H. Ike, "Fundamental Mechanisms of Galling and other Surface Damage Caused by Sliding and/or Plastic Deformation", Adv. Tech. of Plasticity, vol. 1, 1984, pp. 180-185.

36) S. Makkimattila and A. Ranta-Eskola, "Behavior of Galvanized Coatings during Forming", Proc. of 13th Bienn. Congr. of the IDDRG, Melbourne, Australia, 1984, pp. 292-303.

37) T. Nakamori and A. Shibuya, "Effects of Galvannealing

Conditions and Coating Weight on Powdering Resistance of Galvannealed Steel Sheet", Corrosion-Resistant Automotive Sheet Steels, ed. L. Allegra, ASM, Metals Park, Ohio, 1988, pp. 139-149.

38) S. Nakamura, M. Yoshida and A. Nishimoto, "Frictional Characteristics of Coated Steel Sheets", Proc. of the 15th Bienn. Congr. of the IDDRG, Dearborn, Michigan May 16-18, 1988, pp. 77-83.

39) M. Ejima, Y. Tokunaga, and T. Honda, "Analysis of Formability and some problems in Stamping of Coated Steel Sheets", Proc. of the 13th Bienn. Congr. of IDDRG, Melbourne, Australia, 1984, pp. 317-328.

40) A.E. Wilson III, "Friction Effects on the formability of Electrogalvanized and Hot-Dipped Automotive Sheet Steel", M.S. Thesis, No. T-3733, Colorado School of Mines, Golden, Colorado, 1989.

41) M. Sulonen, P. Eskola, J. Kumpulainen and A. Ranta-Eskola, "A Reliable Method for Measuring the Friction Coefficient in Sheet Metal Forming", in IDDRG Working Group Meeting, Tokyo, Japan, 1981.

42) D.W. Vallance, D.K. Matlock and C.J. Van Tyne, "Determination of Friction Coefficients of Sheet Metal by the Bending Under Tension Test", ASPPRC Research Report No. MT-SRC-089-035, Colorado School of Mines, Golden, Colorado, September 1989.

43) K. Hanaki and K. Kato, "Pressure Peak in Bending and Unbending Process", Adv. Tech. of Plasticity, vol. 1, 1984, pp. 581-587.

44) P.H. Hansen, N. Bay and P. Christensen, "Analysis of the Ring Compression Test using a General Friction Model and the Upper Bound Elemental Technique", North American Manufacturing Research Conference Proceedings - 16, Urbana, Illinois, May 24-27, 1988, pp. 41-47.

45) F.P. Bowden and D. Tabor, The Friction and Lubrication of Solids, Clarendon Press, Oxford, 1950.

46) J.S. McFarlane and D. Tabor, "Relation between Friction and Adhesion", Proc. Roy. Soc. London, vol. 202A, 1950, pp. 244-253.

47) T. Wanheim and N. Bay, "A model for Friction in Metal Forming Processes", Ann. of CIRP, 27, 1978, pp. 189-194.

48) J. Halling, Principles of Tribology, Macmillan Press, 1978, pp. 40-67.

49) F.P. Bowden and D. Tabor, The Friction and Lubrication of Solids, Clarendon Press, Oxford, 1964, pp. 320-349.

50) G.E. Dieter, Mechanical Metallurgy, 3rd. edition, McGraw Hill Book Company, 1986, pp. 77-79.

51) A.P. Green, "Friction between Unlubricated Metals: A Theoretical Analysis of the Junction Model", Proc. Roy. Soc. London, vol. 228A, 1955, pp. 191-204.

52) A.P. Green, "The Plastic Yielding of Metal Junctions due to Combined Shear and Pressure", J. Mech. Phys. Solids, vol. 2, 1954, pp. 378-393.

53) J.M. Challen and P.L.B. Oxley, "An Explanation of the Different Regimes of Friction amd Wear using Asperity Deformation Models", Wear, vol. 53, 1979, pp. 229-243.

54) H. Moalic, J.A. Fitzpatrick and A.A. Torrance, "The Correlation of the Characteristics of Rough Surfaces with Their Friction Coefficients", Proc. I. Mech. E., vol. 201, 1987, pp. 321-329.

55) P. Lacey, A.A. Torrance and J.A. Fitzpatrick, "The Relation between the Friction of Lubricated Rough Surfaces and Apparent Normal Pressure", J. Tribology, Trans. ASME, vol. 111, 1989, pp. 260-264.

56) D. Tabor, "Junction Growth in Metallic Friction: the Role of Combined Stresses and Surface Contamination" Proc. Roy. Soc. London, vol. 251A, 1959, pp. 378-393.

57) C. Rubenstein, "The Coefficient of Friction of Metals", Wear, vol. 2, 1958/59, pp. 85-96.

58) J.M. Alexander, "The Effect of Coulomb Friction in the Plane-Strain Compression of a Plastic-Rigid Material", J. Mech. Phys. Solids, vol. 3, 1955, pp. 233-245.

59) W.R.D. Wilson, "Friction and Lubrication in Sheet Metal Forming", Mechanics of Sheet Metal Forming -

Material Behavior and Deformation Analysis, ed. by Koistinen and Wang, Plenum Press, New York-London, 1978, pp. 157-174.

60) J.A. Schey, Tribology in Metal Working - Friction, Lubrication and Wear, American Society for Metals, Metals Park, Ohio, 1983, pp. 11-25.

61) O.O. Adewoye and T.F. Page, "Electron Microscopy Study of Surface and Subsurface Friction Damage in Single-Crystal SiC", Wear, vol. 73, 1981, pp. 247-260.

62) B. Avitzur, C.K. Huang and Y.D. Zhu, "A Friction Model Based on the Upper-Bound Approach to the Ridge and Sublayer Deformation", Wear, vol. 95, 1984, pp.59-77.

63) J.H. Dautzenberg, "The Role of Dynamic Recrystallization in Dry Sliding Wear", Wear, vol. 60 1980, pp. 401-411.

64) P.J. Blau, "Measurements and Interpretations of Sliding Wear Damage in Metals", J. Tribology, Trans. ASME, vol. 107, 1985, pp. 483-490.

65) T. Wanheim and T. Abildgaard, "A Mechanism for Metallic Friction", in Proc. 4th. Int. Conf. Prod. Engn., Tokyo, 1980, p. 122.

66) D.H. Buckley and R.L. Johnson, "The Influence of Crystal Structure and Some Properties of Hexagonal Metals on Friction and Adhesion", Wear, vol. 11, 1968, pp. 405-419.

67) K. Komvopoulos, N.Saka and N.P.Suh, "The Mechanism of Friction in Boundary Lubrication", J. Tribology, Trans. ASME, vol. 107, 1985, pp. 452-462.

68) V. Rangarajan, N.M. Giallourakis, D.K. Matlock and G. Krauss, "The Effect of Texture and Microstructure on Deformation of Zinc Coatings", J. Mater. Shap. Tech., vol. 6, No. 4, 1989, pp. 217-227.

69) V. Rangarajan, C.A. Natalie, D.K. Matlock and G. Krauss, "Deformation Behavior of Hot Dip Galvanized Coatings in Complex Sheet Metal Forming", submitted for publication to Journal of Materials Shaping Technology.

70) D.W. Vallance, D.K. Matlock, "Determination of Friction Coefficients of Sheet Metal by the Bending Under Tension Test", ASPPRC Research Report No. MT-SRC-089-026, Colorado School of Mines, Golden, Colorado, March 1989.

71) D.W. Vallance, D.K. Matlock, and G. Krauss, "Determination of Friction Coefficients of Sheet Metal by the Bending under Tension Test", ASPPRC Research Report No. MT-SRC-088-015, Colorado School of Mines, Golden, Colorado, September 1988.

72) K. Kamei and Y. Ohmori, "Hetero-Epitaxial Growth of Zinc Electrodeposits on Low-Carbon Steel Sheets", J. of Appl. Electrochem., vol. 17, 1987, pp. 821-827.

73) V. Jiricny, H. Choi and J.W. Evans, "Zinc Electrodeposit Morphology under conditions of Fluctuating Current Density", J. of Appl. Electrochem., vol. 17, 1987, pp. 91-103.

74) A.C. Beshore, B.J. Flori, G. Schade and T.J. O'Keefe, "Nucleation and Growth of Zinc Electrodeposited from Acidic Zinc Solutions', J. Appl. Electrochem., vol.

17, 1987, pp. 765-772.

75) N.M. Giallourakis, D.K. Matlock and G. Krauss, "A Cryogenic Fracture Technique for Characterizing Zinc-Coated Steels", Metallography, in press.

76) Selected Powder Diffraction Data for Metals and Alloys, Data Book, Vol. 1, 1st edition, (Index Card No. 4-831), JCPDS International Centre for Diffraction Data, 1978.

77) U. Lindborg, "Observations on the Growth of Whisker Crystals from Zinc Electroplate", Metall. Trans. A, 6A, 1975, pp. 1581-1586.

78) G.F. Bastin, F.J.J. Van Loo and G.D. Rieck, "A New compound in the Iron-Zinc System", Z. Metallkde, vol. 10, 1974, pp. 656-660.

79) G.F. Bastin, F.J.J. Van Loo and G.D. Rieck, "On the Texture in the δ(Fe-Zn) Layer formed during Hot Dip Galvanizing", Z. Metallkde, vol. 67, 1976, pp. 694-698.

80) G.F. Bastin and F.J.J. Van Loo, "On the Texture in the ζ(Fe-Zn) Layer formed during Hot Dip Galvanizing", Z. Metallkde, vol. 69, 1978, pp. 540-545.

81) C.M. Vlad, M. Dahms and H.J. Bunge, "ODF Analysis of Texture of Galfan and Galvanized Hot Dipped Coatings of Low Carbon Steel Sheets", Private Communication, Institut fur Metallkunde und Metallphysik, TU Clausthal, FRG.

82) S.H. Deits, D.K. Matlock, G. Krauss and C.J. Van Tyne, "Mechanisms of Coating Failure during Deep Drawing", ASPPRC Research Report No. MT-SRC-089-035, Colorado School of Mines, Golden, Colorado, September 1989.

83) B. Avitzur, C.J. Van Tyne, Z.J. Luo and C.R. Tang, "A Model for the Simulation of Friction between Dies and Workpiece", Adv. Tech. Plasticity, vol. 1, 1984, pp. 200-207.

84) H.D. Nine, "Drawbead Forces in Sheet Metal Forming", Mechanics of Sheet Metal Forming, eds. D.P. Koistinen and Neng-Ming Wang, Plenum Press, New York, 1978, pp. 179-211.

APPENDIX A

INFORMATION ON ZINC SINGLE CRYSTAL DEFORMATION

From: "Zinc - The Science and Technology of the Metal, Its Alloys and Compounds", C.H. Mathewson, Reinhold Publishing Company, New York, 1959, pp. 411-419.

CRYSTAL STRUCTURE

HEXAGONAL CLOSE PACKED STRUCTURE

SLIP

Primary slip is on (0001) planes and $[\bar{2}110]$ directions Secondary slip on $(\bar{2}110)$ planes at elevated temperatures Average Critical Resolved Shear Stress (CRSS) at room temperature = 37.0 gm/mm^2

TWINNING

Twinning occurs on $(10\bar{1}2)$ planes (pyramidal planes)

Twinning

- involves shearing along $[10\bar{1}1]$ direction (Refer to figure A1)
- occurs when compressive stress is exerted normal to basal planes.
- occurs when tensile stress is exerted parallel to basal planes in corresponding $[10\bar{1}0]$ direction
- CRSS for twinning is not clear - values from 300 to 600 gm/mm^2 are reported in literature.

- is not possible when compressive stresses act parallel to basal planes
- is not possible when crystal is restrained by grips, polycrystalline material, adjacent grain or twin.

CLEAVAGE

Cleavage occurs along basal planes when a critical tensile stress is applied normal to these planes. Critical cleavage stress is approximately 180-200 gm/mm^2. Critical cleavage stress remains relatively unaffected at low temperatures while CRSS for slip increases significantly. Therefore, basal plane cleavage is more likely at low temperature in crystals having borderline orientations. Twinning can position basal planes in favorable position for cleavage.

Slip and twinning are the main modes of deformation during rolling of polycrystalline zinc. Grain reorientation during twinning promotes slip.

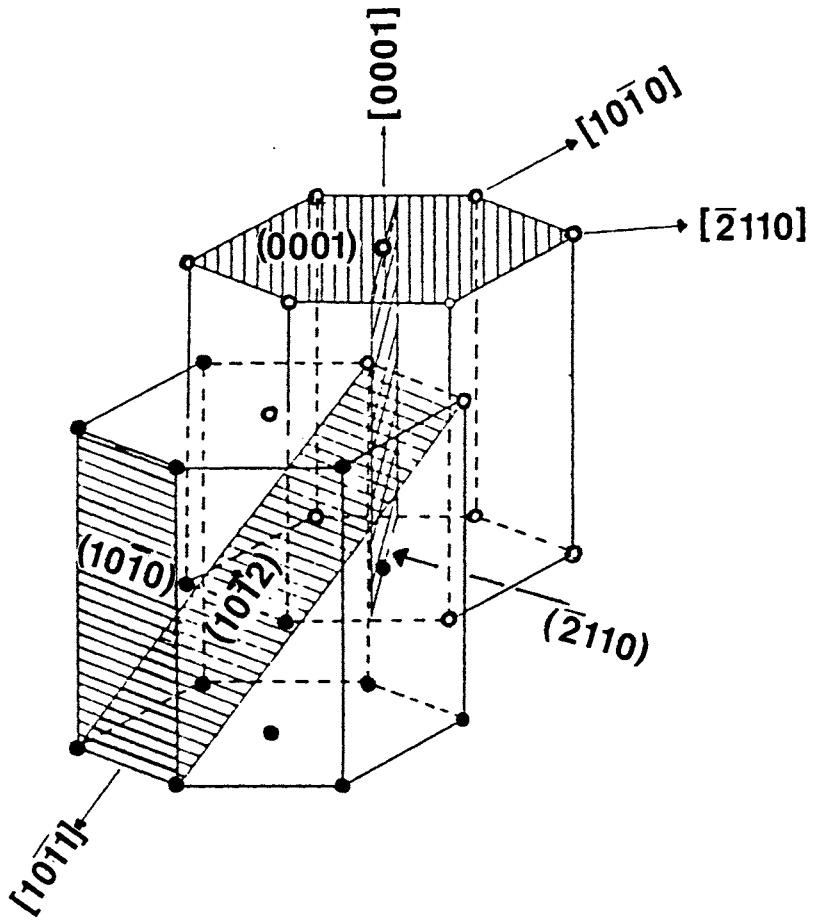

Figure A1 Arrangement of atoms in the crystal structure of zinc